PROPAGATION OF STATISTICAL UNCERTAINTY IN MESH-BASED SHUTDOWN DOSE RATE CALCULATIONS

by

Moataz S. Harb

A dissertation submitted in partial fulfillment of
the requirements for the degree of

Doctor of Philosophy

(Nuclear Engineering and Engineering Physics)

at the

UNIVERSITY OF WISCONSIN–MADISON
2019

Date of final oral examination: 03/15/2019

The dissertation is approved by the following members of the Final Oral Committee:

Paul P.H. Wilson, Professor, Nuclear Engineering
D. Henderson, Professor, Nuclear Engineering
J. Blanchard, Professor, Nuclear Engineering
B. Bednarz, Professor, Medical Physics
P. Chien, Professor, Statistics

Dedicated to my soulmate, Shymaa

ACKNOWLEDGMENTS

I would like to express my gratitude to my advisor, Prof. Paul P.H. Wilson, for guiding me through my Ph.D. journey and for his excellent wisdom and leadership which all helped me articulate my scientific qualities and be a better version of myself. Special thanks to my parents, Aida & Salah, and my wife, Shymaa, for their continuous support and encouragement. I would like to thank Dr. Andrew Davis for many years of scientific discussions that helped me understand many scientific concepts and methodologies and also for teaching me a lot about programming. I would also like to thank all members of the Computational Nuclear Engineering Research Group (CNERG) for their support and insights in numerous occasions. Finally, I would like to thank my dissertation committee for their comments and the helpful advice they provided during my preliminary examination and on reviewing the final draft of my thesis. It is worth mentioning that my thesis work was funded in part by projects DE-FG02-99ER54513 and DE-SC0017122 from the U.S. Department of Energy (DOE), Office of Fusion Energy Sciences (OFES).

CONTENTS

LIST OF TABLES

LIST OF FIGURES

ABSTRACT

In fusion energy systems (FES), high energy neutrons are emitted from the plasma source - due to the D-T fusion reaction - enabling them to penetrate deep in the materials surrounding the core. Energy is then deposited along the path of the neutrons due to interactions with nuclides, resulting in - besides nuclear heating - two main effects; radiation damage and transmutation. Radiation damage causes changes in the macroscopic properties of the materials due to microscopic changes that result from interactions of high energy neutrons with nuclides. Transmutation is caused by the absorption of neutrons by nuclides in the medium and almost always results in the production of radioactive nuclides. Such radioactive nuclides are of importance to FES design and operation as they persist after the shutdown of the facility due to their long half lives. Efforts are directed to quantify the shutdown dose rate (SDR) that results from gamma emitting nuclides produced by transmutation. Monte Carlo (MC) methods are favored over deterministic methods for the simulation of particles transport in FES due to complexity of the models and to reduce the uncertainties/errors of the predicted particle flux distributions due to approximations. The rigorous 2-step method (R2S) relies on dedicated activation calculations to predict the photon emission density distribution, and is widely used for SDR quantification. It involves a neutron transport step, activation analysis to obtain the photon emission density, and a photon transport step to calculate the SDR.

It is often the case that neutrons suffer attenuation in traversing the medium from the plasma source - due to interactions with nuclides - and that results in a steep gradient in the neutron flux. Variance reduction (VR) tools have been developed with the primary goal of pushing neutrons - simulated particles - to regions of the phase-space that are of importance for the quantities under consideration in order to reduce the uncertainty in the MC results. The recently developed Group-wise Transmutation - Consistent Adjoint Driven Importance Sampling (GT-CADIS) method provides a capability to obtain the photon emission density distribution

as a function of the energy dependent group-wise neutron flux distribution via linearization of the transmutation operator. Using the photon emission density it is possible to overcome previous difficulties of the error propagation in the R2S workflow. One primary concern with the R2S workflow is that only the contribution of the photon transport step is considered as a measure of the uncertainty of the calculated SDR, while the contribution from the neutron transport step remains undefined. Previous methods have tried to tackle this issue but there was always difficulty in obtaining the correlation of the neutron fluxes and that resulted in implementing either impractical approximations or just calculating the upper and lower bounds of the uncertainty of the SDR.

In this document, the R2S workflow has been investigated. First, issues related to the neutron transport step and the uncertainty of the photon emission density have been addressed. Second, a scheme was developed to propagate the statistical uncertainty of the neutron transport step to the SDR. Starting with the neutron transport step, a variation of the main R2S that aimed at increasing the resolution while reducing the computational expenses was found to introduce systematic errors that might undermine the gain in the computational cost. One of the difficulties in propagating the neutron flux uncertainty to the photon emission density is obtaining the correlation values between the neutron fluxes in different energy groups and mesh voxels. By utilizing the GT method, an approximation to the calculation of the correlation coefficients has been investigated building on the fact that using group-wise transmutation the correlation terms needed were greatly reduced. It was discovered that the correlation between the neutron fluxes in different energy groups is a function of the material composition. That facilitated obtaining the needed correlation matrix and quantifying the uncertainty of the photon emission density. A method to propagate the photon source uncertainty to the SDR by random sampling was developed and was demonstrated to be efficient on various types of numerical experiments as well as a production level problem.

1 INTRODUCTION

Many research efforts have been directed to harnessing fusion energy for commercial and research purposes by testing many confinement and fuel cycle concepts. The confinement concepts include inertial (laser, z-pinch, etc.) and magnetic (tokamak, stellarator, etc.) confinement. The fuel cycle includes many candidates that utilize deuterium (D), tritium (T), and helium (He) such as the $D-T$, $D-D$, $D-He^3$, etc. [1]. The magnetically confined tokamak and the $D-T$ fuel cycle shows potential as a practical way to pave the road for the first commercial power plant [2]. When D and T nuclei are fused together under the harsh conditions inside the plasma core, energy is released. Neutrons are emitted with energies as high as $14.1\,MeV$ and, being neutral, result in deep penetration in materials present in the system, leading to deposition of energy along their path and eventually absorption/leakage. Such behavior affects the materials in the core - besides nuclear heating - in two ways; radiation damage and transmutation.

Radiation damage is caused by the high energy particles from the plasma colliding as they traverse the medium causing microscopic defects in the structural materials that could lead - over time - to macroscopic changes in the materials properties, necessitating the replacement of some components. On the other hand, transmutation happens when the neutron is absorbed by a nucleus leading to the formation of an excited nucleus that might decay via different modes by emission of different types of radiation.

Some of the transmutation interactions in the facility are utilized and controlled for breeding the rare T used as fuel while others lead to the formation of radioactive nuclei that decay by the emission of gamma radiation, persisting even after shutdown due to their long half lives. This radiation can also cause damage to biological tissues, so the access/handling of personnel to such "hot" components inside the facility has to be controlled. Operation of FES like ITER [3] and FNSF [4] requires a maintenance schedule to repair/replace components. The schedule determines wait times to allow the dose rate levels from induced radioactivity in the components to drop below the acceptable limits. An accurate assessment of the

SDR is then necessary not only for the maintenance stage but also for the design of shielding in the facility.

Many methodologies have been developed to obtain reliable SDR estimates by simulating the transport and interaction of particles with the materials exposed to the radiation environment. The MC method is a stochastic tool that simulates the random walk of the particles in the medium. The basic idea is to follow a particle as it traverses the medium and simulate its behavior according to the laws of physics. Random number generators are used to select the state of the particle - energy, direction, type of interaction, etc. - until the particle "history" is terminated. The quantity of interest is then calculated as the mean of the contributions of many such histories. As the method is stochastic, the calculated quantities of interest have associated uncertainties that result from the spread in the distribution of the contributions of all particles histories simulated.

Many codes exist (MCNP [5], FLUKA [6], etc.) that rely on the MC method and provide useful means of simulating radiation transport in FES. Recent developments [7] have introduced new capabilities by improving the geometry representation of the problem allowing for more accurate modeling of design details and making the simulation more robust. With its capabilities to simulate particle transport in a continuous space-energy phase-space, MC has been widely used for SDR quantification for FES. Deterministic tools [8] also exist that simulate the particles behavior in the medium by solving a set of differential equations that represent a mathematical model of the problem. Discretization is then necessary in energy, space, angle, and time and for complex geometries like FES that could result in approximation errors. Coupling of both methods [9] has proven to boost large scale simulations and aid in obtaining high fidelity results.

FES are modular integrated engineering systems with many components that serve different purposes; blankets for tritium breeding, shielding to protect the life-time components such as the magnets, and other engineering components inside the facility. Shielding in the facility - whether biological shield or to protect components - results in a steep gradient in the neutron flux making it difficult to obtain the desired neutron flux distribution - using MC methods - with acceptable

statistical uncertainty especially at locations away from the plasma source or behind shields. Numerous VR techniques are utilized with one goal in mind, pushing simulated neutrons to regions of phase-space with high importance to the objective (flux, detector response, etc.). Many tools have been utilized to accurately generate the needed parameters for VR among which the most widely utilized concept is that of "importance functions" [10].

One of the methods in use to quantify the SDR in FES is the rigorous 2-step (R2S) [11] method. The workflow of R2S consists of a neutron transport step to obtain the multi-group flux distribution over a mesh covering the problem geometry. Using nuclear inventory analysis codes, the obtained neutron flux distribution is then used to simulate nuclear transmutations and obtain the distribution of gamma emitting radionuclides in the system. The nuclear density distribution of those radionuclides defines the photon emission density. The photon emission density distribution then defines a source for the transport code to be used in the photon transport step. Using the resulting photon flux distribution, flux-to-dose-rate conversion factors are then used to estimate the biological dose (SDR) at the detector(s) at different times after shutdown. Whether deterministic or MC solutions of the transport problem are used in the SDR calculation there exist many sources of uncertainties that have to be taken into account; modeling approximations, discretization, cross section data uncertainties, transport solution uncertainties, etc. Until recently, in the R2S workflow only the contribution from the photon transport step has been considered as a measure of the uncertainty of the calculated SDR assuming that the neutron flux distribution is obtained with low uncertainty which would lead to obtaining a photon source with low uncertainty, as a result [12].

While efforts have been directed towards developing new tools for more accurate and reliable SDR calculations with a focus on the effect of nuclear data uncertainties on the SDR, less effort focused on the effect of the other sources of uncertainties on the SDR. Those tools are validated against standard benchmark problems and an example of data uncertainty propagation in Boltzmann/Bateman coupled problems can be found in literature [13]. Previous work [14] [15] tried to answer questions on how the uncertainty of the neutron transport solution affects the calculated SDR.

The method tried to propagate the statistical uncertainty from the MC transport solution in the workflow using the adjoint flux and the relation of the SDR to the photon source distribution. The main obstacle was the difficulty of calculating the needed correlation terms between neutron fluxes in different regions of the phase-space.

A different approach has been adopted in this work building on recent development in the CADIS method [16] which will help mitigate the difficulty in the propagation of the uncertainty from the neutron transport step to the calculated SDR. The GT-CADIS method provides a tool to calculate the group-wise photon emission density distribution as a function of the group-wise neutron flux distribution (space-energy distribution). Using group-wise transmutation under certain conditions - which are widely satisfied for most materials and irradiation scenarios in FES [16] - the photon emission density in different energy groups can be constructed in a form that makes utilization of error propagation techniques more practical.

This document examines a new approach that overcomes the difficulties encountered with previous methods and obtains a reliable estimate of the contribution of the transport solution uncertainty to the calculated SDR in the R2S workflow. This is done over two steps: by propagating the statistical error through the transmutation operator (from neutrons to the photon source), then by incorporating it into the sampling of the photon source (from the photon source to the SDR). By dividing the error propagation scheme into two steps, it provides a tool to validate new practices in the SDR calculation and study the effect of different methodologies in obtaining the neutron flux distribution on the final SDR uncertainty. The transport solution uncertainty could affect the SDR in two possible ways; uncertainty of the neutron transport and uncertainty of the photon transport. Building on the newly developed GT-CADIS method, the photon emission density in every mesh element (spatial mesh voxel and energy bin) could be obtained as a function of the energy dependent neutron spectrum in the spatial mesh voxel. The photon emission density as a function of the neutron spectrum as calculated using GT method allows propagating the statistical uncertainty from the neutron transport

step all the way to the SDR.

In R2S workflow, the statistical uncertainty of the calculated neutron flux distribution - obtained using the MC method - in space-energy phase-space is given by the code and can then be directly propagated to the calculated photon emission density using the available error propagation techniques. One variation of the main R2S workflow [17] focused on reducing the uncertainty of the obtained neutron flux distributions while reducing also the number of nuclear inventory calculations needed to obtain the photon emission density. The method is based on the idea of scaling the photon emission density calculated on a coarse spatial mesh by the total flux magnitudes over the desired fine mesh. Such method - as will be shown in this work - is found to be equivalent to the main R2S workflow with the neutron flux distribution replaced by a *constructed* flux distribution over the coarse and fine meshes. That will affect the statistical uncertainty of the flux distribution and a propagation of the statistical error is then paramount to judge the validity of such practice which - up until now - is not practically possible.

As the statistical uncertainty of the neutron flux distribution is propagated to the photon emission density as mentioned above, two possible ways could be adopted to propagate the uncertainty to the SDR; *implicit* and *explicit*. The *implicit* method involves editing the sampling routine of the transport code to sample from the photon emission density with its associated standard deviation, treating the emission density at each mesh element as a local distribution. The method is developed to estimate the contribution of the photon source uncertainty to the total uncertainty of the SDR and has been demonstrated to be efficient on various numerical experiments.

In this work, the uncertainty of the photon source in the R2S workflow as a result of the uncertainty of the neutron flux distribution will be studied. A method will be developed to estimate the photon source uncertainty which will then be propagated to the SDR. This document is divided into different chapters covering background, theory, and future work. In chapter 2, a thorough literature review of the neutron transport, MC tools, VR techniques, nuclear inventory analysis, and SDR analysis will be presented. Chapter 3 will discuss the uncertainty of

the neutron transport step in the R2S workflow and will introduce a new method to calculate the uncertainty of the photon emission density. Chapter 4 will be dedicated to the method of propagating the statistical uncertainty to the photon emission density in a newly developed variation of the R2S workflow. In chapter 5, a method to propagate the uncertainty of the photon source to the SDR via random sampling will be discussed. Finally, in chapter 6 the newly developed methods will be applied to a production-level problem; the uncertainty of the photon emission density in one sector of the FNSF facility will be calculated as well as the total uncertainty of the SDR.

In the following sections, a brief background of many physics/computational concepts that lie at the heart of SDR quantification will be introduced. Starting with the physics of neutron interaction with matter, the different ways to solve the neutron transport equation, and the transmutations of nuclei exposed to radiation and the nuclear inventory analysis that is performed to quantify that. The computational schemes currently in use to quantify the SDR will also be introduced followed by a discussion of the need for more reliable estimations and what difficulties faces achieving such goal.

2.1 Neutron Transport and the Boltzmann Equation

2.1.1 The Boltzmann Equation

The neutron transport equation is a balance equation that describes the behavior of neutrons in the medium and can be used to obtain the particles distribution in FES. In its simplest form, the Boltzmann equation can be written as in Eq. (2.1). It is often the case that in FES the steady state equation is solved for the distribution of particles in the facility, so the time derivative in the equation is set to zero.

$$\left[\frac{1}{\nu}\frac{\partial}{\partial t} + \hat{\Omega}.\vec{\nabla} + \Sigma(\vec{r}, E)\right]\psi(\vec{r}, \hat{\Omega}, E, t) = q(\vec{r}, \hat{\Omega}, E, t) + \iint dE' d\hat{\Omega}' \Sigma_s(\vec{r}, E' \rightarrow E, \hat{\Omega}'.\hat{\Omega})\psi(\vec{r}, \hat{\Omega}', E', t) \quad (2.1)$$

In Eq. (2.1), $\psi(\vec{r}, \hat{\Omega}, E, t)$ is the angular particle flux defined as the number of particles at point $\vec{r}$ with energies in dE about energy E and moving in directions contained within an infinitesimal cone of directions $d\hat{\Omega}$ about unit vector $\hat{\Omega}$ at time t. $\Sigma(\vec{r}, E)$ is the total macroscopic cross section which is defined as the probability per unit path length that a collision between a particle with energy E and a nucleus at point $\vec{r}$ in the medium will happen. $q(\vec{r}, \hat{\Omega}, E, t)$ encapsulates all the information

about the external source of particles in the medium. The term $\Sigma_s(\vec{r}, E' \rightarrow E, \hat{\Omega}'.\hat{\Omega})$ is defined as the double differential scattering cross section which is the probability per unit path length that a neutron with energy E' and moving in direction $\hat{\Omega}'$ will as a result of a scattering collision at point $\vec{r}$ emerge with energy in dE about E and direction in $d\hat{\Omega}$ about unit vector $\hat{\Omega}$.

2.1.2 Adjoint Neutron Transport

The steady state transport equation can be written in operator form as in Eq. (2.2a),

$$H\psi(\vec{r}, \hat{\Omega}, E) = q(\vec{r}, \hat{\Omega}, E) \tag{2.2a}$$

where the transport operator H is defined as in Eq. (2.2b),

$$H = \hat{\Omega}.\vec{\nabla} + \Sigma(\vec{r}, E) - \iint dE'd\hat{\Omega}'\Sigma_s(\vec{r}, E' \rightarrow E, \hat{\Omega}'.\hat{\Omega}) \tag{2.2b}$$

Mathematically, the adjoint problem could be defined as in Eq. (2.3) where $\langle . \rangle$ denotes an inner product, integration over all independent variables $(\vec{r}, \hat{\Omega}, E)$. Eq. (2.3) yields the adjoint form of the transport equation given in Eq. (2.4) and the adjoint flux $\psi^+(\vec{r}, \hat{\Omega}, E)$ is a quantity that has wide application in the modeling/simulation of FES. The adjoint flux is usually used in MC VR - using the detector response as a localized adjoint source - and it has the physical meaning of the importance of different regions in the space-energy phase-space to the SDR at the detector location [18].

$$\left\langle \psi^+(\vec{r}, \hat{\Omega}, E), H\psi(\vec{r}, \hat{\Omega}, E) \right\rangle = \left\langle H^+\psi^+(\vec{r}, \hat{\Omega}, E), \psi(\vec{r}, \hat{\Omega}, E) \right\rangle \tag{2.3}$$

$$\left[-\hat{\Omega}.\vec{\nabla} + \Sigma(\vec{r}, E)\right] \psi^+(\vec{r}, \hat{\Omega}, E) = q^+(\vec{r}, \hat{\Omega}, E) + \iint dE'd\hat{\Omega}'\Sigma_s(\vec{r}, E \rightarrow E', \hat{\Omega}.\hat{\Omega}')\psi^+(\vec{r}, \hat{\Omega}', E') \tag{2.4}$$

The physical meaning of the adjoint flux could be shown by an example problem. Assume there is a detector at point $\vec{r}_d$ with a response function defined as $\sigma_d(\vec{r}, E)$, then the detector response R could be defined as,

$$R = \left\langle \psi(\vec{r}, \hat{\Omega}, E), \sigma_d(\vec{r}, E)\delta(\vec{r} - \vec{r}_d) \right\rangle \tag{2.5}$$

and by defining the adjoint problem using the detector response function as the adjoint source we end up with,

$$H^+\psi^+(\vec{r}, \hat{\Omega}, E) = q^+(\vec{r}, \hat{\Omega}, E) = \sigma_d(\vec{r}, E)\delta(\vec{r} - \vec{r}_d) \tag{2.6}$$

and using equations (2.2a) , (2.3), and (2.5) ,

$$\begin{aligned} \left\langle \psi^+(\vec{r}, \hat{\Omega}, E), q(\vec{r}, \hat{\Omega}, E) \right\rangle &= \left\langle q^+(\vec{r}, \hat{\Omega}, E), \psi(\vec{r}, \hat{\Omega}, E) \right\rangle \\ &= \left\langle \sigma_d(\vec{r}, E)\delta(\vec{r} - \vec{r}_d), \psi(\vec{r}, \hat{\Omega}, E) \right\rangle = R \end{aligned} \tag{2.7}$$

and from this result it can be shown that the detector response, $R = \langle \psi^+, q \rangle$ is just the contribution of the source q weighted by the adjoint flux ψ^+.

2.1.3 Deterministic Neutron Transport

The term "deterministic" is used in contrast to "stochastic" when discussing solutions to the transport equation. Deterministic solutions of the transport equation involve numerical methods that seek solution to the equation by means of discretization in space, energy, angle, etc. The energy discretization is achieved by dividing the whole energy range into intervals of custom width and integrating the transport equation (Eq. (2.1)) over different group ranges. It builds on the concept of separation of energy and space of the angular flux as shown in Eq. (2.8)

$$\psi(\vec{r}, \hat{\Omega}, E) = \psi_g(\vec{r}, \hat{\Omega})f(E) \quad , \quad E_g \leqslant E \leqslant E_{g-1} \tag{2.8}$$

where the energy index, g, increases as the neutron energy decreases and the spectral energy function $f(E)$ is normalized according to Eq. (2.9).

$$\psi_g(\vec{r},\hat{\Omega}) = \int_{E_g}^{E_{g-1}} dE\psi(\vec{r},\hat{\Omega},E) = \int_{E_g}^{E_{g-1}} dE\psi_g(\vec{r},\hat{\Omega})f(E) = \psi_g(\vec{r},\hat{\Omega})\int_{E_g}^{E_{g-1}} dEf(E) \tag{2.9}$$

Applying discretization in energy to the steady state form of Eq. (2.1) yields,

$$\left[\hat{\Omega}.\vec{\nabla} + \Sigma_g(\vec{r})\right]\psi_g(\vec{r},\hat{\Omega}) = q_g(\vec{r},\hat{\Omega}) + \sum_{g'=0}^{G}\int_{\hat{\Omega}'} d\hat{\Omega}'\Sigma^s_{g'\to g}(\vec{r},\hat{\Omega}'.\hat{\Omega})\psi_{g'}(\vec{r},\hat{\Omega}') \tag{2.10}$$

where $\psi_g(\vec{r},\hat{\Omega})$ is group g angular flux, $\Sigma_g(\vec{r})$ is group g macroscopic cross section and is given by Eq. (2.11), $q_g(\vec{r},\hat{\Omega})$ is the angular source strength of the emitted neutrons in group g, and $\Sigma^s_{g'\to g}(\vec{r},\hat{\Omega}'.\hat{\Omega})$ is the macroscopic scattering cross section from group g' to group g.

$$\Sigma_g(\vec{r}) = \frac{\int_{E_g}^{E_{g-1}} dE\Sigma(\vec{r},E)\psi(\vec{r},\hat{\Omega},E)}{\int_{E_g}^{E_{g-1}} dE\psi(\vec{r},\hat{\Omega},E)} \tag{2.11}$$

Numerous methods build on the energy discretization of the transport equation and use finite difference techniques to achieve discretization in space to relate the flux in different mesh elements. The discrete ordinates, S_N, method solves the discretized multi-group transport equation along certain directions that form a quadrature set.

The method is suitable to obtain quick estimates of the flux distribution - at the cost of accuracy due to truncation and discretization - which are often used in hybrid methods (MC/deterministic) to estimate the needed parameters for VR. The method uses large computing resources due to the need to store vast amounts of data - cross sections and angular multi-group fluxes for each ordinate for each mesh element - at each iteration step. One of the limitations of this method is that it is ill fitted for situations where streaming plays a large role. Ray effects which are just high flux values along certain discrete directions near voids and streaming

might not be well represented if the streaming direction is not well aligned with an angle of the quadrature set. All of those limitations make it hard for deterministic methods to find wide applications in SDR calculation in FES, so stochastic methods are considered more suitable for such applications.

2.1.4 Monte Carlo Neutron Transport

With the ability of continuous treatment of the transport equation independent variables (space & energy), MC methods provide a more convenient tool - compared to deterministic methods - to model FES. MC codes such as MCNP use a number, N, of particle histories to simulate physical particles as they traverse the medium. MCNP uses a pseudo random number generator to randomly select the state of the particle along its path to populate the history. A history starts by randomly sampling the particle from a given source distribution; using random numbers to select the position, direction, energy. Random numbers are then generated to sample the distance to the next collision, the type of nuclides, and the type of collision. Histories are terminated when a particle is absorbed or escapes the medium. That avoids the systematic error introduced when simulating FES using deterministic methods such as the discretization of energy, space, and angle.

MCNP calculates the contribution of all histories simulated to the quantities of interest and that results in a probability density function (PDF). Quantities such as fluxes, currents, reaction rates, etc. are tallied over the geometry and reported by the code as the mean of the contribution of the N histories as given by Eq. (2.12a). The stochastic nature of the simulation process results in a statistical uncertainty - which can be calculated from the generated PDF - of the calculated quantities which is used as a measure of the accuracy of the obtained results. A relative error (R) - which is defined as in Eq. (2.12b), where $\sigma(\hat{x})$ is the standard deviation of the quantity $\hat{x}$, is one such measure.

$$\hat{x} = \frac{1}{N} \sum_{i=1}^{N} x_i \tag{2.12a}$$

$$R = \frac{\sigma(\hat{x})}{\hat{x}} \tag{2.12b}$$

2.2 Activation and Nuclear Inventory Analysis

In FES, materials are exposed to radiation either from the plasma itself (alpha particles, neutrons, etc.) or from the products of radiation interaction with other nuclides in the facility. The main effect that is of interest for SDR analysis of irradiation in FES is transmutation. Transmutation occurs when a nuclide absorbs a neutron forming a compound nucleus that decays by the emission of subatomic particles. Most of the produced nuclides are radioactive that persist even after shutdown of the facility due to their long half lives. The concentration of various nuclides in the facility is affected by transmutation and decay processes and while the former is only relevant during operation, the latter is of importance during operation and after shutdown and is the source of SDR. Mathematical models have been developed to calculate the inventory of various nuclides and dedicated activation analysis codes (such as ALARA [19], FISPACT [20], etc.) obtain the distribution of nuclides in the facility at different time steps by solving such models.

2.2.1 The Bateman Equation

The most famous mathematical model to solve for the concentration of nuclides in a decay chain was developed by Bateman [21] in 1910 and since then it has been expanded to include other sources of production of various nuclides in the chain such as irradiation. Consider a linear decay chain, $N_1 \rightarrow N_2 \rightarrow ... \rightarrow N_{n-1} \rightarrow ...$, then the concentration of different nuclides can be described by a system of differential equations as shown in Eq. (2.13). By applying an integral transform and after some algebraic manipulations, Bateman derived the solution of the system of differential equations for the concentration of nuclides, at time = t, as shown in Eq. (2.14), where N_i^o and λ_i are the initial concentration and the decay constant of

nuclide N_i, respectively.

$$\frac{dN_1}{dt} = -\lambda_1 N_1 \quad , \quad \frac{dN_2}{dt} = \lambda_1 N_1 - \lambda_2 N_2 \quad , \quad ... \quad ,$$
$$\frac{dN_{n-1}}{dt} = \lambda_{n-2} N_{n-2} - \lambda_{n-1} N_{n-1} \quad , \quad ... \tag{2.13}$$

$$N_1 = N_1^o e^{-\lambda_1 t} \quad , \quad N_2 = \frac{\lambda_1}{\lambda_2 - \lambda_1} N_1^o e^{-\lambda_1 t} + \left[\frac{\lambda_1}{\lambda_1 - \lambda_2} N_1^o + N_2^o \right] e^{-\lambda_2 t} \quad , \quad ... \tag{2.14}$$

2.2.2 The Transmutation Mathematical Model

The Bateman mathematical model can be extended to include production/destruction of nuclides in a radiation field. The production rate per nucleus, $P^T_{i\to j}$, of nuclide j due to transmutation of nuclide i in a radiation field can be expressed as a function of an energy dependent production microscopic cross section, $\sigma_{i\to j}(\vec{r}, E)$, and the neutron flux, $\phi(\vec{r}, E)$, as in Eq. (2.15a). The other pathway by which nuclide j could be produced from nuclide i is by radioactive decay, $P^D_{i\to j} = \lambda_{i\to j}$ with $\lambda_{i\to j}$ being the decay constant. The total production rate per nucleus of nuclide j from nuclide i is shown in Eq. (2.15b).

$$P^T_{i\to j} = \int dE \sigma_{i\to j}(\vec{r}, E)\phi(\vec{r}, E) \tag{2.15a}$$

$$P^{Total}_{i\to j} = P^T_{i\to j} + P^D_{i\to j} \tag{2.15b}$$

The same procedure could then be followed as in the derivation of Bateman equations by writing the balance equations of all nuclides in the medium. The balance equations could be written in a matrix form using a transfer matrix, **A**, and a vector of nuclides concentrations, $\vec{N}(\vec{r}, t)$. The elements of the matrix along the diagonal (i,i) being the destruction rates of nuclide i and the off-diagonal elements (i,j) being the production of nuclide i from nuclide j. The rate of change of $\vec{N}(\vec{r}, t)$

as a result of both radioactive decay and transmutation in a radiation field is given by Eq. (2.16a) and a solution is given in Eq. (2.16b). In FES, it is often the case that as a result of the complex irradiation scenario a large number of nuclides will be created due to irradiation and the production/destruction pathways will form a complex system of balance equations and in turn a large, and possibly sparse, $\mathbf{A}$. Activation codes focus on utilizing numerical methods to solve such systems.

$$\frac{\partial}{\partial t}\vec{N}(\vec{r},t) = \mathbf{A}\vec{N}(\vec{r},t) \tag{2.16a}$$

$$\vec{N}(\vec{r},t) = \vec{N}(\vec{r},0)e^{\mathbf{A}t} \tag{2.16b}$$

2.3 Shutdown Dose Rate Calculation

As mentioned in the introduction, a key point in the design/operation of FES is the quantification of SDR for hands-on maintenance around irradiated components in the facility. Fully comprehensive computation of SDR requires - in general - three steps; neutron transport, activation, and photon transport. The neutron transport step calculates the neutron energy dependent flux distribution in the facility and it can be obtained using either deterministic or stochastic tools as discussed before. The neutron flux is then used to calculate the distribution of gamma emitting nuclides at different times after shutdown. The obtained distribution is then used and a photon transport calculation is performed to obtain the photon flux distribution at the points of interest. Flux-to-dose-rate conversion factors such as $ICRP-74$ [22] are then used to estimate the SDR. In this section two procedures that have been developed, to-date, to estimate the SDR are discussed: the Direct 1-Step (D1S) [23] [24] method and the Rigorous 2-Step (R2S) [11] method.

2.3.1 Direct 1-Step (D1S) Method

The method was initially developed to overcome the difficulty of using deterministic methods, like S_N method, in modeling complex geometries, such as ITER, as it

introduced high uncertainties due to approximations [23]. The method was also developed to provide a tool to obtain a better spatial resolution of the photon source distribution as the photon transport is performed - in one step alongside neutron transport - at the locations of emission of photons. As MC codes such as MCNP calculates the prompt gamma production from (n, γ) reactions, it is possible to modify the code to produce decay gamma and as a result both neutron and photon transport calculations could be performed in one step. Modification to the nuclear data libraries were introduced by replacing the prompt gamma reaction such as the cross section and spectrum by those of reactions producing nuclides that decay by gamma emission. Based on the irradiation scenario, the ratio of the actual contribution to the SDR of the production rates calculated by the code could then be obtained and applied to the contribution of all the nuclides of interest.

The concept of the method is presented by Eq. (2.17) where $q_i(\vec{r}, E^p)$ is the photon emission density from nuclide i at energy E^p, $\sigma_{j\to i}(\vec{r}, E^p, E^n)$ is the production rate of nuclide i from nuclide j due to neutron interaction at energy E^n. Also, the modified cross section contains information about the decay constant and branching ratio of the nuclide producing the photon. The main challenge with the method is the production of such modified cross sections for all the isotopes in the problem. The method has been applied to complex geometries as in ITER and JET [25]. The method is fast as both the neutron and photon transport are performed in one step and also the method provides high spatial resolution of the photon emission density as photons are emitted at locations of production. One disadvantage of the method lies in the fact that it is problem dependent as pre-analysis has to be done to determine some relevant parameters in relation to the contribution of activated nuclides to the SDR.

$$q_i(\vec{r}, E^p) = \int_{E^n} \sigma_{j\to i}(\vec{r}, E^p, E^n)\phi(\vec{r}, E^n)\, dE^n \tag{2.17}$$

2.3.2 Rigorous 2-Step (R2S) Method

Unlike the D1S method, the R2S method involves two separate transport steps; neutron and photon. First, neutron transport is performed and the distribution of neutrons is obtained - as a function of space and energy - in the geometry cells or over a superimposed mesh. The neutron flux distribution is then used as an input for dedicated activation and nuclear inventory codes that perform analyses to quantify the transmutation of the materials in the problem domain. The distribution of the nuclides decaying by gamma emission is then obtained and is used as a source definition for the following photon transport step. Photon transport is then performed and the flux distribution - as a function of space and energy - is obtained at different locations of interest in the problem geometry. Flux-to-dose-rate conversion factors [22] are then used to estimate the SDR at those locations. The R2S workflow will be used throughout this work.

The R2S method has been through several developments all aiming at a more efficient utilization of computing resources and a higher fidelity of the obtained results. While they all agree on the activation and photon transport steps, they differ based on how the neutron transport step is performed. With the cell-based R2S [11], the multi-group neutron flux distribution is obtained for all non-void cells in the problem geometry and the resolution of the flux is then governed by the size of the different cells that the geometry is decomposed into. Using MCNP meshtally capabilities, in the mesh-coupled R2S method [26] the neutron flux distribution is obtained over a mesh laid on the problem geometry and the resolution is then a function of the size of the mesh voxels. Such method allows controlling the size of the mesh and the resolution without the need to make changes to the model itself.

To achieve a more efficient use of computing resources by means of reducing the number of activation calculations performed, the R2Smesh [17] method utilizes a split of the neutron transport step. The neutron flux spectra are obtained over a coarse mesh and are used for activation calculations. The obtained photon source over the coarse mesh is then scaled to the desired fine mesh by the total neutron flux over the fine mesh. The method has been applied to complex geometries as in

ITER and JET [25] and was found to be in good agreement with experimental data.

2.4 Monte Carlo Variance Reduction

In FES the objective of many materials in the facility is to protect the life-time components, such as the magnets, or to help breed the rare fuel, such as tritium (T). In both cases the result is a steep gradient in the neutron flux across regions that contain shielding or breeding materials. As a result of the steep gradient in the flux not all particles will reach regions behind shielding materials and by analogy, not all simulated histories in MC contribute to tallies behind shielding materials. The distribution of tally scores from all histories can be assumed as shown in Fig. (2.1) with $g(x)$ being the distribution of scores of histories contributing to the calculated tally and $\bar{x}$ is the mean of histories scores.

A fraction of histories, c on Fig. (2.1), will not contribute - contribution is zero - to the quantity being evaluated - such as a flux behind a thick shield - and that might increase the relative error of the tally. That increase in the relative error could be related to a high standard deviation due to the fact that small fraction of histories score and contribute to the tally resulting in a spread in the distribution of scores. It could also be related to a low mean of the calculated tally if a large fraction of histories, c, didn't score resulting in a lower mean than expected. A figure of merit (FOM) is defined as given in Eq. (2.18) where $\sigma^2(\hat{x})$ is the variance of the calculated quantity $\hat{x}$ and T is the computer time spent in processing all histories.

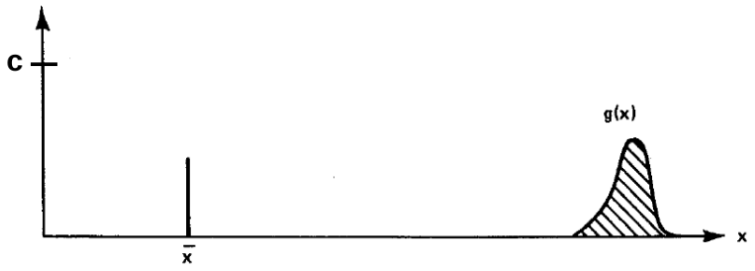

Figure 2.1: Distribution of Tally Scores [8]

$$\mathrm{FOM} = \frac{1}{\sigma^2(\hat{x})\mathrm{T}} \tag{2.18}$$

2.4.1 Non-Analog Monte Carlo

VR methods aim at increasing the FOM of the calculated tallies and the main focus of the different VR techniques fall under three categories; source, transport (Russian roulette, splitting, exponential transform, etc.), and collision (implicit capture, forced collision, etc.) biasing. Applying VR techniques will affect both terms contributing to the FOM, the variance of the tally, $\sigma^2(\hat{x})$, and the time spent in tracking particles, T. In source biasing, the source PDF is biased such that particles are being sampled more frequently in regions of the phase-space that are important to the objective. To ensure that no systematic bias is being introduced and that particles weights in the problem are conserved, a statistical weight is applied to the modified PDF as given by Eq. (2.19). In the equation, W is a particle weight and P is sampling frequency.

$$W_{\mathrm{unbiased}}\mathrm{P}_{\mathrm{unbiased}} = W_{\mathrm{biased}}\mathrm{P}_{\mathrm{biased}}. \tag{2.19}$$

The transport biasing - splitting/roulette - of particles is controlled by means of weight windows (WW). WWs are range of weights, upper and lower bounds on the weight of the particle in different regions of the space-energy phase-space such that particles are split or the Russian roulette game performed - to terminate histories - when the weight of the particle entering a region is outside the range. Particles histories are split when moving to a region of higher importance - weight above the upper bound - or terminated via Russian roulette when moving to a region of lower importance - weight below the lower bound. In case of splitting, the particles weights are adjusted with a proper reduction of the weight of each history. As a result, MC codes will spend more time tracking histories but on the other hand having more histories in an important region increases the chance of scoring to tallies in that region and reduce the spread in the scores. The overall effect is an increase in T and a decrease in $\sigma^2(\hat{x})$ and with proper implementation,

the combined effect could be an increase in the FOM.

2.4.2 GT-CADIS

The photon emission density that results from transmutation/decay of nuclides exposed to neutrons could be expressed in integral form as a function of the energy dependent neutron flux as in Eq. (2.20). A new method, Group-wise Transmutation - Consistent Adjoint Driven Importance Sampling (GT-CADIS) [16], provides the conditions under which a solution for the transformation function, T, in Eq. (2.20) can be obtained. Such a solution can be found given that some criteria are satisfied which facilitate introducing some approximations to the activation analysis. The photon source distribution could be obtained if the distribution of the nuclides emitting photons is known. By adopting the concept of linear transmutation chains, the photon source distribution can be expressed as a sum of the contribution from the last nuclide in each chain as shown in Eq. (2.21) where λ_{c,i_c} is the decay constant, $b_{c,i_c}(E^p)$ is the branching ratio, and $N_{c,i_c}(\vec{r}, t_{tot})$ is the concentration of the last nuclide, i_c, in chain c at point $\vec{r}$ and time t_{tot}.

$$q(\vec{r}, E^p) = \int_{E^n} T(\vec{r}, E^p, E^n)\phi(\vec{r}, E^n)\, dE^n \tag{2.20}$$

$$q(\vec{r}, E^p, t_{tot}) = \sum_c \lambda_{c,i_c} b_{c,i_c}(E^p) N_{c,i_c}(\vec{r}, t_{tot}) \tag{2.21}$$

Eq. (2.21) can be expressed in a form similar to Eq. (2.20) so that a solution for T could be obtained. By decomposing the nuclide concentration as a function of time, a further simplified expression can be found. As each nuclide concentration is calculated at time = t_{tot} that could be expressed as an irradiation/decay up to time = t_{irr} and then only decay in the absence of any transmutation after shutdown from time = t_{irr} to time = $t_{tot} - t_{irr} = t_{dec}$. If the concentrations of nuclides are obtained at the end of irradiation then it can be obtained at any time following the shutdown using the laws of radioactive decay. Such expression is shown in Eq. (2.22) with the quantity $N_{c,j}(\vec{r}, t_{irr})B_{c,i_c,j}(t_{dec})$ representing the rate of production

of nuclide i_c from nuclide j via chain c after a decay time = t_{dec}. An expression relating the nuclide concentration at t_{irr} to the neutron flux distribution is shown in Eq. (2.23) where $U_{c,i}(\vec{r}, E^n, t_{irr})$ is a function that is defined by the equation.

$$N_{c,i_c}(\vec{r}, t_{tot}) = N_{c,i_c}(\vec{r}, t_{irr}) e^{-d_{c,i_c} t_{dec}} + \sum_{j=1}^{i_c-1} N_{c,j}(\vec{r}, t_{irr}) B_{c,i_c,j}(t_{dec}) \tag{2.22}$$

$$N_{c,i}(\vec{r}, t_{irr}) = \int_{E^n} U_{c,i}(\vec{r}, E^n, t_{irr}) \phi(\vec{r}, E^n)\, dE^n \tag{2.23}$$

The GT-CADIS method showed that under certain criteria, called the Single Neutron Interaction and Low Burnup (SNILB), a solution to T can be found. Under such criteria it is assumed that the only flux-dependent pathway is from the parent to the first daughter in the chain and the production of the other nuclides in the chain can be assumed to be flux independent. The low burnup condition ensures that the concentrations of the other nuclides in the chain are not dependent at any time on the flux but only on the decay process of higher nuclides in the chain. Violation methods have been also provided to be used when the SNILB criteria are not met. It has also been shown that T is independent of the flux magnitude and is only a function of the irradiation scenario and the material composition. The T value could be calculated for each unique material composition in the problem using an arbitrary neutron spectrum that allows all reaction chains to be populated such that the SNILB criteria are satisfied.

2.5 Statistical Uncertainty of Shutdown Dose Rate

2.5.1 Introduction

FES like ITER, DEMO [27], and FNSF will produce neutron fluxes at energies that go far beyond anything so far encountered in nuclear technology. This will put very challenging demands on the design especially the selection of construction materials and it will necessitate that a high-quality simulation of neutronic processes be

performed for a successful development of a fusion device. A good understanding of biases and uncertainties on FES calculations is essential for assessing safety features and design margins. That results in an increasing demand for best estimate predictions to be provided with their confidence bounds, leading to the definition of several benchmarks for acquiring a realistic estimation of uncertainties to judge the reliability of the simulation results. As mentioned in the introduction, biases are induced by many sources such as modeling approximations (geometry simplification, spatial discretization), nuclear cross section data uncertainties, transport solution uncertainties, etc. In this section, the main sources of SDR uncertainties will be discussed as well as some methods in use for quantification.

2.5.2 Sources of SDR Uncertainty

2.5.2.1 Nuclear Cross Section Data Uncertainties

Whether evaluated through experimental methods or using dedicated codes, the importance of nuclear cross sections variance-covariance data rests on the proposition that there would be little sense in evaluating nuclear cross sections without the corresponding information on how well the values are known. Unless integral experimental results are available, without covariance files there will be no way to estimate the accuracy of calculated results using nuclear data. While nuclear cross sections covariance data are obtained using experimental methods, it is impractical to require experiments to validate all the calculated quantities - such as the SDR - using nuclear data especially those related to FES either in the design or operation phase. In such situation, covariance data are used to assess the reliability of the obtained results based on the uncertainty of the cross section data. In SDR workflows the neutron flux is calculated by simulating the physical processes in the medium which is quantified using nuclear data, so macroscopic neutronic calculations are related to microscopic nuclear data and is affected by any uncertainties in the data.

The obtained neutron flux distribution is used to collapse cross section data and calculate nuclear number densities of nuclides in the medium especially those emitting gamma through decay processes. It can be seen that an uncertainty in a cross

section value could affect the flux and the photon source distribution which is used to perform photon transport and quantify the SDR. Fusion shielding benchmarks are generally used to test design codes and nuclear data for fusion devices. In general, the nuclear data file for a given isotope or element, is created on the basis of theoretical nuclear model calculations and microscopic measurements, with eventually some adjustments due to a restricted number of integral measurements. Few methods exist to quantify the uncertainty in the SDR due to nuclear data uncertainty such as TMC [28] [29], GRS [29], etc.

2.5.2.2 Monte Carlo Statistical Uncertainty

In using the R2S workflow to quantify the SDR, MC methods are often used for neutron and photon transport calculations. As shown before, MC evaluates the mean values of the quantities of interested by simulating the random walk of particles in the medium and such mean values have statistical uncertainties associated with them. In R2S, it is often the case that the uncertainty of the calculated SDR contains only the statistical uncertainty of the last MC transport step, photon transport. As the neutron flux distribution calculated in the first step is used to quantify the photon source distribution that is used in the second step, the final uncertainty of the SDR obtained based only on that of the second step is expected to be underestimated. As the activation model is non-linear, these uncertainties can be compounded in time because of the nature of transmutation and decay calculations. The total uncertainty of the SDR can be thought of having two contributing terms; neutron transport uncertainty and photon transport uncertainty as given by Eq. (2.24) [12].

$$\sigma^2_{SDR,Total} = \sigma^2_{SDR,Neutron} + \sigma^2_{SDR,Photon} \tag{2.24}$$

2.5.3 Methods in Use for Uncertainty Propagation

2.5.3.1 Brute Force Method

The simplest and costly technique to quantify the *total* uncertainty in the SDR due to both the neutron and photon transport steps is the brute force. Multiple clones of the whole problem (neutron transport, activation, photon transport) with different inputs (different random number seeds in the transport steps) are run and the sample standard deviation of the obtained SDR is computed and taken to be the total uncertainty of that result as demonstrated in Fig. (2.2). The technique needs large computing resources and it is often the case that many such clones are needed to ensure statistical quality of the obtained uncertainty.

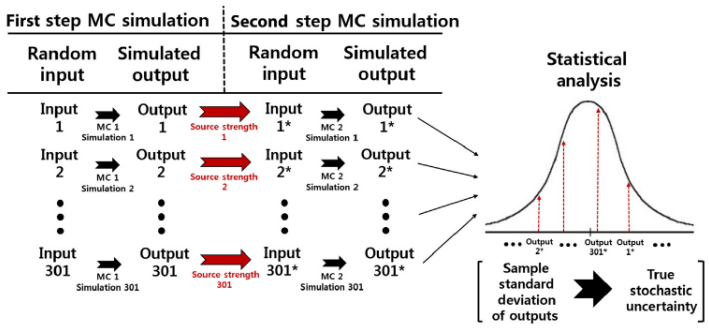

Figure 2.2: Uncertainty Quantification: Brute Force Method [30]

2.5.3.2 Adjoint Based Method

The MS-CADIS [14] method was extended [15] to estimate the contribution of the neutron transport step uncertainty to the calculated SDR uncertainty by seeking an adjoint neutron source that lead to an expression of the SDR as given by Eq. (2.25) where $q^{+}_{n,i}$ is the adjoint neutron source in mesh element i. Using error propagation techniques, the uncertainty of the SDR is then given by Eq. (2.26) where $\rho_{j,l}$ is the correlation between fluxes in mesh elements j and l. j and l are indices for mesh elements designated by space and energy (x,y,z,E). The correlation coefficients between adjacent elements are expected to be > 0 while it diminishes

for elements farther away apart. Because of the difficulty of obtaining correlation coefficients between all elements in the space-energy phase-space, the upper and lower bounds are only estimated using this method by setting all values of $\rho_{j,l}$ to 1 and 0, respectively. The upper and lower bounds are given in Eq. (2.27).

$$SDR = \sum_i \phi_{n,i} q^+_{n,i} \tag{2.25}$$

$$\sigma^2_{SDR,Neutron} = \sum_i (\frac{\partial SDR}{\partial \phi_{n,i}})^2 (\sigma_{\phi_{n,i}})^2 + 2 \sum_{j<l} (\frac{\partial SDR}{\partial \phi_{n,j}})(\sigma_{\phi_{n,j}})(\frac{\partial SDR}{\partial \phi_{n,l}})(\sigma_{\phi_{n,l}})\rho_{j,l} \tag{2.26}$$

$$(\sigma^{Lower}_{SDR,Neutron})^2 = \sum_i (q^+_{n,i})^2 (\sigma_{\phi_{n,i}})^2 \quad , \quad \sigma^{Upper}_{SDR,Neutron} = \sum_i (q^+_{n,i})(\sigma_{\phi_{n,i}}) \tag{2.27}$$

2.5.3.3 On-the-Fly Method

A new method [30] has been recently proposed to overcome the difficulty - as mentioned in the previous subsection - of calculating the correlation coefficients by means of substituting for the adjoint terms by other quantities that can be calculated using MC codes while performing the transport calculations. The SDR is considered as the summation over the contribution of all mesh elements as given by Eq. (2.28). The SDR_i from a mesh element i is just the photon source strength at that element, $q_{p,i}$, weighted by the importance of the contribution of that element to the SDR which is quantified by the adjoint flux, $\phi^+_{p,i}$, obtained using the response function at the detector as the adjoint source. Using the error propagation formula with Eq. (2.28) we end up with the formula in Eq. (2.29)

$$SDR = \sum_i SDR_i = \sum_i q_{p,i} \phi^+_{p,i} \tag{2.28}$$

$$\sigma^2_{SDR,Neutron} = \sum_i (\phi^+_{p,i})^2 (\sigma_{q_{p,i}})^2 + 2 \sum_{j<l} (\phi^+_{p,j})(\sigma_{q_{p,j}})(\phi^+_{p,l})(\sigma_{q_{p,l}})\rho_{j,l} \quad (2.29)$$

As the photon source strength in mesh element i, $q_{p,i}$, is proportional to the neutron reaction rate, $R_{n,i}$, then by multiplying and dividing Eq. (2.29) by the source strength, $q_{p,i}$, and substituting for $\frac{\sigma_{q_{p,i}}}{q_{p,i}}$ by $\frac{\sigma_{R_{n,i}}}{R_{n,i}}$ we end up with Eq. (2.30). $R_{n,i}$ is the neutron reaction rate in mesh element i calculated using MCNP and $\sigma_{R_{n,i}}$ is the statistical uncertainty. In Eq. (2.30), SDR_i is the contribution of mesh element i to the calculated SDR and this quantity is estimated by flagging photons from mesh elements during MCNP photon transport step. To calculate the correlation coefficients, the method uses a unit cell strategy, scoring the results in both the mesh elements and a set of unions of the mesh elements and use the given uncertainty to estimate the covariance terms. The covariance between mesh elements j and l is then calculated as given by Eq. (2.31).

$$\sigma^2_{SDR,Neutron} = \sum_i (SDR_i)^2 (\frac{\sigma_{R_{n,i}}}{R_{n,i}})^2 + 2 \sum_{j<l} (SDR_j)(\frac{\sigma_{R_{n,j}}}{R_{n,j}})(SDR_l)(\frac{\sigma_{R_{n,l}}}{R_{n,l}})\rho_{j,l} \quad (2.30)$$

$$Cov_{j,l} = \frac{\sigma^2_{R_{n,j+l}} - \sigma^2_{R_{n,j}} - \sigma^2_{R_{n,l}}}{2} \quad (2.31)$$

2.6 Summary

In this chapter, a literature review was given about SDR calculation in FES using the R2S workflow. It has been shown that the obtained neutron fluxes using MC methods has an associated uncertainty due to the stochastic nature of the simulation. While many sources of uncertainty has been introduced, the focus in this work will be on the uncertainty of both the photon sources and SDR in R2S workflow due to the neutron flux distribution uncertainties.

3 UNCERTAINTY QUANTIFICATION OF THE PHOTON SOURCE I (R2S WORKFLOW)

3.1 Introduction to the GT Method

As discussed in Chapter 2, transmutations in FES of nuclides exposed to a neutron radiation field take place and some interaction pathways lead to the formation of photon emitting nuclides that persist after the shutdown of the facility due to their long half lives. Monte Carlo (MC) codes such as MCNP [5] provide the capability to obtain the flux distribution with its associated statistical uncertainty. The neutron flux can be tallied over a mesh covering the problem geometry with custom energy bins structure making it easy to utilize the concept of group-wise (GT) transmutation. It has been shown [16] that the photon source can be expressed as a function of the energy dependent group-wise neutron flux distribution. Using a transformation function, T, that relates the photon emission density to the energy dependent neutron flux distribution, the energy dependent photon emission density can be expressed as shown in Eq. (3.1),

$$q(\vec{r}, E^p) = \int_{E^n} T(\vec{r}, E^p, E^n)\phi(\vec{r}, E^n)\, dE^n \tag{3.1}$$

where the superscript p and n are for photons and neutrons, respectively and $\phi(\vec{r}, E^n)$ is the neutron flux at point $\vec{r}$ and energy E.

Using MCNP to estimate high resolution - used to resolve the flux gradients in different regions of the system - neutron flux distribution, discretization in space and energy is needed. The discretization in MC is just a way to define a region of space and/or energy to tally over without introducing any changes to the problem geometry. Using MCNP meshtally capabilities, the typical procedure is to lay a mesh on top the problem geometry and divide the energy range into a number of intervals corresponding to the number of neutron energy groups of interest. The number of energy groups is related to the format available of the nuclear

data library used for cross section data for the interaction of neutrons with the different nuclides in the problem while the size/shape of the mesh is governed by the resolution needed in the calculated neutron flux.

Discretization of Eq. (3.1) in energy and space is carried out by integrating over the photon energy range of interest and a region of space corresponding to the spatial mesh size. Carrying out the discretization as in Eq. (3.2a), the result is a group-wise form as shown in Eq. (3.2b), where the subscript h is for a photon energy group and g is for a neutron energy group, and ν designates a spatial mesh voxel. The energy bin structure typically in use for SDR calculations corresponds to 24 photon energy groups and 175 neutron energy groups (175 groups logarithmically spaced between 0 and 19.64 MeV).

$$\iiint_R \int_{E^p}^{E^p+\Delta E^p} q(\vec{r}, E^p)\, dE^p\, dr^3 = \iiint_R \int_{E^p}^{E^p+\Delta E^p} \int_{E^n}^{E^n+\Delta E^n} T(\vec{r}, E^p, E^n)\phi(\vec{r}, E^n)\, dE^n\, dE^p\, dr^3 \tag{3.2a}$$

$$q_{\nu,E_h^p} = \sum_g T_{\nu,E_h^p,E_g^n}\phi_{\nu,E_g^n} \tag{3.2b}$$

The GT method builds on the concept of superposition of the photon source distribution when the SNILB criteria are met. This means that the collective contribution of the flux in every neutron energy group - when used individually - to the photon source distribution sums up to the contribution of the whole spectrum. When applied, the photon source distribution in every photon energy group h can be expressed as the sum of the photon sources at the same energy group h produced via individual transmutations with the neutron fluxes at every single energy group one-at-a-time as shown in Eq. (3.3a),

$$q_{\nu,E_h^p}(\phi_\nu) = \sum_g q_{\nu,E_h^p}(\phi_{\nu,E_g^n}) = \sum_g T_{\nu,E_h^p,E_g^n}\phi_{\nu,E_g^n} \tag{3.3a}$$

and ϕ_ν is given by;

$$\phi_\nu = \sum_g \phi_{\nu,E_g^n} \tag{3.3b}$$

It has been shown [16] that the concept of superposition - with the SNILB criteria

met - of the photon source distribution is satisfied for most materials used in FES and for most irradiation scenarios. A dedicated activation and nuclear inventory code (ALARA [19] is used in this work) can then be used to perform the analysis using the group-wise neutron flux distribution. The obtained photon emission density for each neutron energy group in each mesh voxel is then used along with the corresponding flux value to calculate the value of T as shown in Eq. (3.4). It is worth noting that the multi-group neutron flux, ϕ_{v,E_g^n}, used to calculate T_{v,E_h^p,E_g^n} does not need to be the actual local spectrum in the problem in the mesh voxel v - per [16] - as T is independent of the flux magnitude and only depends on the material composition and the irradiation scenario.

$$T_{v,E_h^p,E_g^n} = \frac{q_{v,E_h^p}(\phi_{v,E_g^n})}{\phi_{v,E_g^n}} \tag{3.4}$$

3.2 Modification of the GT Method

The calculation of the transformation function, T in Eqs. (3.1) & (3.2b), in the GT [16] method derives from an approximation of a nonlinear function, $f(\phi_n)$, which relates the photon emission density, $q(\vec{r}, E^p)$, to the multi-group neutron flux, $\phi(\vec{r}, E^n)$, as shown in Eq. (3.5).

$$q(\vec{r}, E^p) = \int_{E^n} f\left(\phi(\vec{r}, E^n)\right) dE^n \tag{3.5}$$

A Taylor expansion of such function showed that higher order terms can be ignored. The first order term was ignored based on the assumption that decay photons only result from neutron interactions. While that assumption is true for most materials used in FES, it ignores the fact that some elements have a naturally occurring radioactive isotopes. While ignoring the first term wouldn't affect the calculation of the photon emission density using Eq. (3.3a), a more accurate representation of the photon emission density is required for uncertainty quantification.

Further analysis of the photon emission density showed that, while it's true for most elements that the photon emission is a result of the radionuclides formed due to interaction with neutrons in the radiation field, some elements that are usually

present in fusion applications have natural emitting isotopes, initial activity. Such initial activity is not a function of the neutron flux and should appear explicitly in Eq. (3.3a). As a result, a modification in the implementation of the GT method has been thought and the photon emission density as a function of the multi-group neutron flux distribution can be expressed as in Eq. (3.6),

$$q_{v,E_h^p}(\phi_v) = q_{v,E_h^p}^{Initial} + \sum_g q_{v,E_h^p}(\phi_{v,E_g^n}) = q_{v,E_h^p}^{Initial} + \sum_g T_{v,E_h^p,E_g^n}\phi_{v,E_g^n} \tag{3.6}$$

where $q_{v,E_h^p}^{Initial}$ is the initial photon emission density at mesh voxel v and photon energy group h.

3.3 Statistical Error Propagation: From Neutrons to the Photon Source

In SDR calculations, MC methods are used to perform both the neutron and the photon transport calculations. As discussed in Chapter 2, MC creates a distribution for the contribution of the different histories to the quantity being calculated such as a flux in a mesh voxel or a reaction rate, etc. The final particle flux distribution (as a quantity of interest for SDR) in different space and energy phase-space regions is just the mean of all the contributions of the different histories in that region and a statistical uncertainty of such quantity can be calculated from the underlying distribution of individual histories scores.

Using the expression for the photon emission density given in Eq. (3.6), it is possible to propagate the statistical error of the calculated MC neutron fluxes to the obtained photon emission density. Further investigation of Eq. (3.6) showed that, on the right hand side, T_{v,E_h^p,E_g^n} encapsulates information about the material composition, decay constants, nuclear cross sections, and the irradiation scenario in a mesh voxel v, while ϕ_{v,E_g^n} contains information about the energy dependent neutron spectrum and the boundary conditions (BCs). As a result, T_{v,E_h^p,E_g^n} can be treated as a constant since the main focus here is on the uncertainty of the neutron

flux and does not consider that of the nuclear cross sections. By applying the error propagation formula to Eq. (3.6) it is possible to propagate the uncertainty of the neutron fluxes at every energy group to the calculated photon emission density as shown in Eq. (3.7),

$$\sigma^2_{q_{\nu,E^p_h}} = \sum_{g,g'} \left(\frac{\partial q_{\nu,E^p_h}}{\partial \phi_{\nu,E^n_g}}\right) \sigma_{\phi_{\nu,E^n_g}} \left(\frac{\partial q_{\nu,E^p_h}}{\partial \phi_{\nu,E^n_{g'}}}\right) \sigma_{\phi_{\nu,E^n_{g'}}} \rho(\phi_{\nu,E^n_g}, \phi_{\nu,E^n_{g'}}) \\ = \sum_{g,g'} T_{\nu,E^p_h,E^n_g} \sigma_{\phi_{\nu,E^n_g}} T_{\nu,E^p_h,E^n_{g'}} \sigma_{\phi_{\nu,E^n_{g'}}} \rho(\phi_{\nu,E^n_g}, \phi_{\nu,E^n_{g'}}) \quad (3.7)$$

where, $\sigma_{q_{\nu,E^p_h}}$ is the standard deviation of the photon emission density in mesh voxel ν and energy group h, $\rho(\phi_{\nu,E^n_g}, \phi_{\nu,E^n_{g'}})$ is the correlation between the neutron fluxes in groups g and g' in mesh voxel ν, and $\sigma_{\phi_{\nu,E^n_g}}$ is the standard deviation of ϕ_{ν,E^n_g}.

When the same mesh is used for both the neutron transport step - to obtain the energy dependent flux distribution - and the following activation analysis the number of the correlation terms between the neutron fluxes needed in the calculation of the standard deviation of the photon source can be reduced. It can be seen from Eq. (3.7) that the only correlation terms that exist are between the neutron fluxes in different energy groups within the same mesh voxel, ν. Eq. (3.7) can be written in a more simplified format as,

$$\sigma^2_{q_{\nu,E^p_h}} = \sum_{g} T^2_{\nu,E^p_h,E^n_g} \sigma^2_{\phi_{\nu,E^n_g}} + 2 \sum_{\substack{g,g' \\ g<g'}} T_{\nu,E^p_h,E^n_g} \sigma_{\phi_{\nu,E^n_g}} T_{\nu,E^p_h,E^n_{g'}} \sigma_{\phi_{\nu,E^n_{g'}}} \rho(\phi_{\nu,E^n_g}, \phi_{\nu,E^n_{g'}}) \quad (3.8)$$

As the neutron fluxes calculated using MC are means of the underlying distributions of scores of different histories, the correlation terms can be calculated given that such distributions are known. MCNP provides an output file (ptrac) which contains all the information of each particle along its path such as the position, energy, direction, statistical weight, etc. and the distributions can be obtained by means of processing such an output file. Using Eq. (3.8) the lower and upper bounds of the standard deviation of the photon emission density can be obtained

by letting $\rho(\phi_{\nu,E_g^n}, \phi_{\nu,E_{g'}^n})$ be 0 and 1, respectively. In the next section, the correlation matrix will be explored further to study its properties and how to be implemented in the uncertainty quantification of the photon source.

3.4 The Correlation Matrix Approximation

When simulating the behavior of neutrons in a medium, the fate of neutrons is determined by collision physics as well as the BCs. The population of neutrons in the problem domain as a whole is a function of the problem settings; source type and BCs of the geometry as leakage will be more significant in case of vacuum vs reflective BCs. Also it is a function of collision physics represented by the nuclear cross section, which is a measure of the probability that different reactions will take place, as neutrons disappear in absorption vs scattering collisions.

By analogy, the population of neutrons in any region - a mesh voxel - of the problem domain is a function of both local BCs and collision physics. Neutrons with low energies in a mesh voxel are either produced at such energies or scattered down from higher energies due to collisions with nuclides whether within the same mesh voxel or in a neighboring one and transported in. In MC calculations a change in the BCs - geometry BCs or meshing scheme (mesh size) - affects directly the population of particles/scoring and in turn the uncertainty of the calculated quantities such as a flux over a mesh.

The underlying distribution of scores of individual histories in every mesh element (spatial mesh voxel and energy bin) could be manipulated to calculate the correlation between the neutron fluxes in different energy bins within each spatial mesh voxel. In complex FES, obtaining the correlation matrix for every mesh voxel in the problem is impractical considering the computing resources needed to process and store the distributions of histories scores. By performing analyses on the correlation matrix for simple problems, few properties of the matrix where discovered that lead to a practical approximation and facilitated using Eq. (3.8) for uncertainty quantification of photon sources in complex FES.

3.4.1 Hypotheses

The correlation of two random variables is a measure of the degree of linear dependence between them. When applying this to neutron fluxes in different energy groups within the same mesh voxel it becomes intuitive to link such correlation to the collision physics, nuclear cross sections. The population of neutrons in a mesh voxel will affect the scoring and in turn the statistical uncertainty of the fluxes. Since the nuclear cross section is unique for each element/mixture, it follows that the correlation matrix could be dependent on the material composition and in turn unique. As a result, the correlation matrix approximation assumes that a unique matrix could be obtained for each element/mixture to a high degree of accuracy with all the neutron energy bins populated.

A change in the population of neutrons present, due to changing the meshing scheme or a change in BCs, at constant material composition, could yield some changes in the resulting correlation matrix but is expected to retain some properties of the "original" and more accurate one. That is because in MC a change in the population of neutrons is linked to scoring and in turn to the uncertainty of the obtained quantities. In other words, a pattern, representative of the relative values of correlation at different energies, is expected to be identifiable in all cases with some changes in the relative magnitudes of the values of the correlation at some energy groups as a response to a change in statistics or due to under-sampling. Analyses where performed on simple problems to assess the properties of the correlation matrix; **uniqueness** and **convergence**.

3.4.2 Properties of the Correlation Matrix

3.4.2.1 Uniqueness

The first set of analyses involved calculating the correlation matrix on a simple geometry for different elements/mixtures. The problem consisted of a cube with uniform material and vacuum BCs on all sides and an external planar boundary 14.1 MeV source facing one side of the cube. The choice of the planar boundary source

and the energy were to simulate cases relevant to FES. The energy dependent multi-group neutron fluxes were tallied on a single mesh voxel covering the entire cube and 175 energy groups. By processing the underlying distribution of histories scores, the correlation matrix was obtained for different elements/mixtures arbitrarily chosen. A mapping of the correlation matrices for different elements is shown in Fig. (3.1) where only the relevant elements, absolute(correlation value) $\geqslant 0.1$, are shown. The energy group numbers on the axes increase with energy; group 175 corresponds to 19.64 MeV. It can be seen from the mappings of the correlation matrices that a unique pattern for each element/mixture is identifiable. Such pattern represents the relative values of the correlation coefficients at different energy groups and has to be dependent on the nuclear cross section of the material.

The second set of analyses involved examining the effect of changing the boundary source energy on the obtained correlation matrices. Should the uniqueness hypothesis be true, the uniqueness property should prevail for any subsets of the correlation matrix. In other words, if the source energy varied then the mapping of the correlation matrix should be a cut of the mapping produced at higher energies, a subset. That follows directly from the hypothesis that the correlation between the fluxes at different energy groups is directly linked to the nuclear cross section of the material. Fig. (3.2) shows mappings of the correlation matrix using 14.1, 7, 3, and 0.25 MeV sources for the same problem described in the previous paragraph and for Steel (SS316L), composition is given in Table 3.1.

Table 3.1: Material Composition for SS316L

Element	Mass %	Element	Mass %
Fe	64.0135	Ta	0.1500
Cr	17.5000	N	0.1100
Ni	11.5000	Nb	0.1000
Mo	2.2500	Ti	0.1000
Mn	2.0000	C	0.0300
Cu	1.0000	P	0.0300
Si	1.0000	S	0.0150
Co	0.0200	B	0.0018

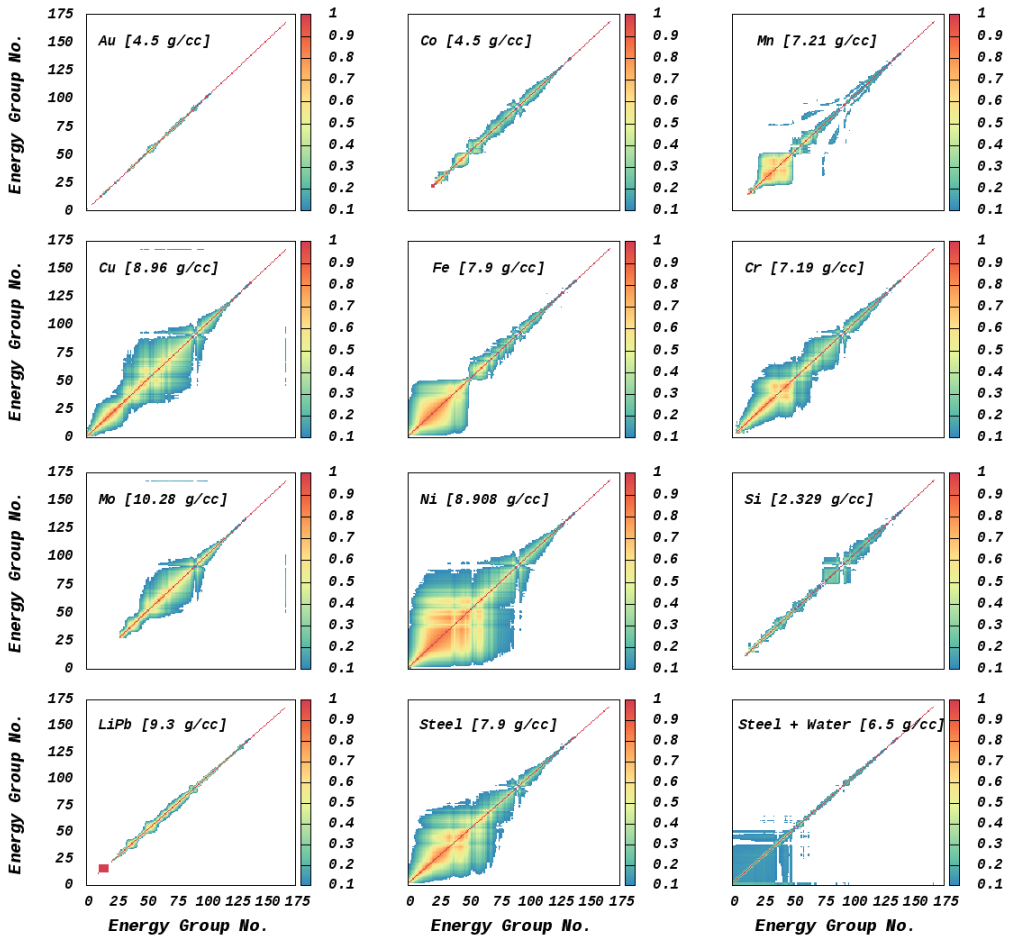

Figure 3.1: Correlation Matrices for Different Elements

The third set of analyses involved obtaining the correlation matrices over a mesh and examining the mappings of matrices inside each mesh voxel. One example of such calculations involved obtaining the correlation matrices for steel (SS316L) over the same cube problem described at the beginning of this section. The problem was divided into five mesh voxels in the z direction and matrices were obtained inside each voxel as well as the matrices for cross-correlation between different voxels as shown in Fig. (3.3). Along the diagonal, the matrices for each mesh voxel can be seen starting from the left-bottom corner on the figure, the far side of the source, and moving along the diagonal till the top-upper corner which is the closest

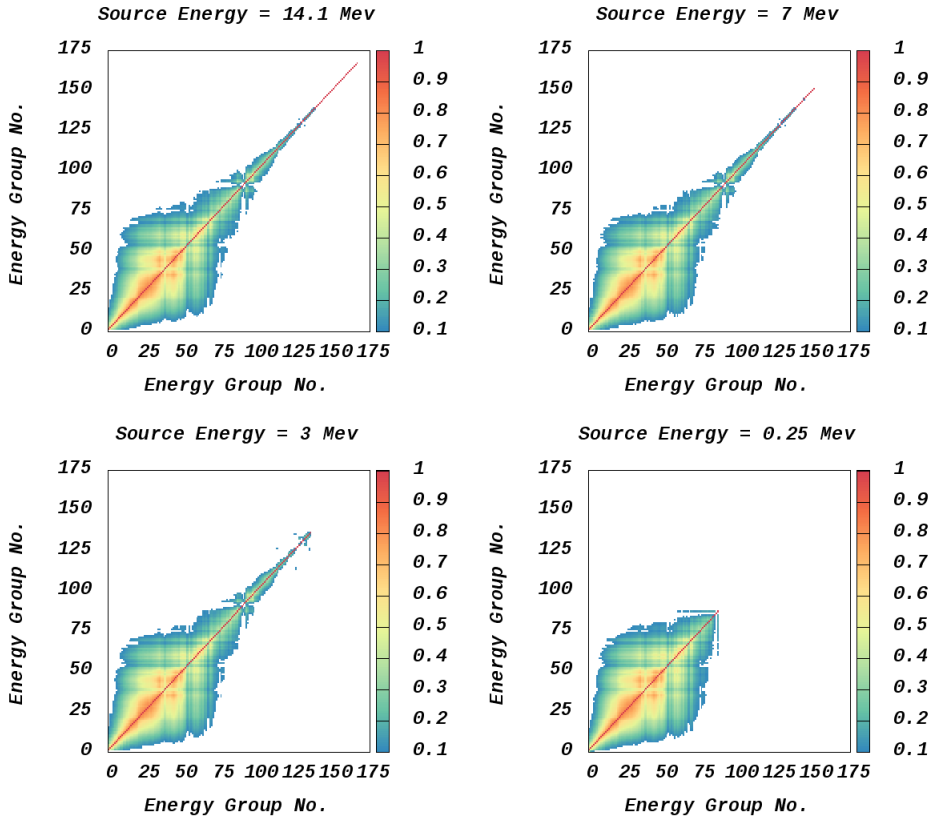

Figure 3.2: Correlation Matrix for SS316L Using 14.1, 7, 3, and 0.25 MeV Sources

voxel to the source. It can be seen that the matrices resemble that of Steel shown in Fig. (3.1). It can also be seen on the figure that the correlation between the neutron fluxes at different energy groups in different mesh voxels, cross-correlation, diminishes as mesh voxels become far apart. This observation has been speculated about before in literature [12], although not by analysis, that neighboring voxels are highly correlated compared to distant ones. Also, from the figure, it can be noticed the loss of symmetry in the correlation between distant voxels. Take for example the third matrix on the bottom row of the figure, the correlations that appear on the matrix is for each energy group and all the groups lower than it. This is due to down-scattering, since ,as mentioned before, neutrons of low energy in a mesh voxel are either slowed down inside the voxel or transported in from neighboring

voxels.

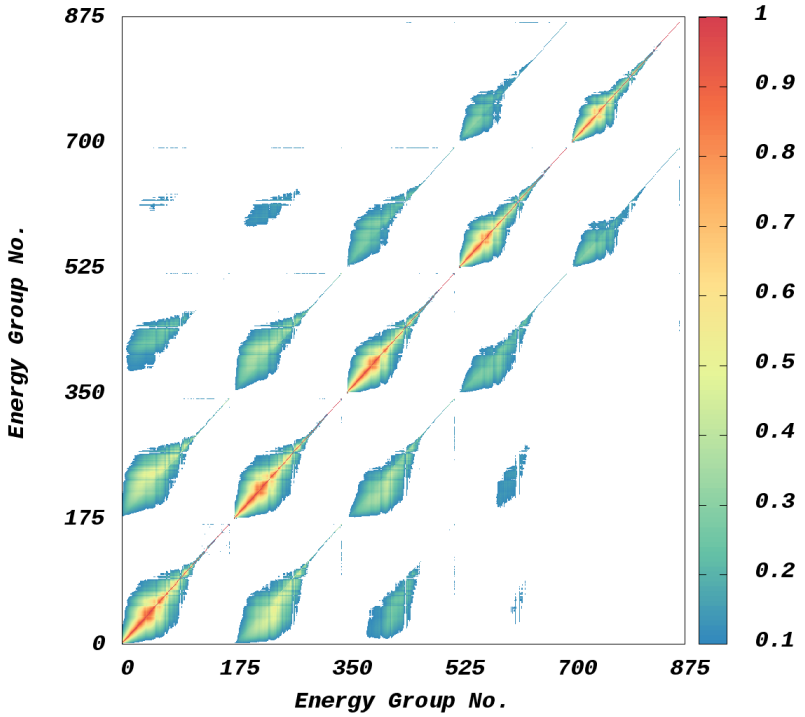

Figure 3.3: The Correlation Matrix for SS316L over a $1 \times 1 \times 5$ Mesh

3.4.2.2 Convergence: Statistical Uncertainty

To study the effect of the uncertainties of neutron fluxes on the correlation matrix, analyses were performed with a cube with isotropic source uniformly distributed inside the cube and reflective BCs on all sides for different materials. To simulate a variation from the condition of bad to acceptable statistical uncertainties, the number of histories processed was varied from 10^3 to 10^6, respectively. It can be seen on Fig. (3.4) how the lower energies are populated and the relative magnitudes in some regions changed as the number of histories increased - as more particles contribute to the calculated flux at lower energies - and a pattern begins to take shape as a result. This further supports the hypothesis of uniqueness, with good statistics a unique pattern for each material could be identified.

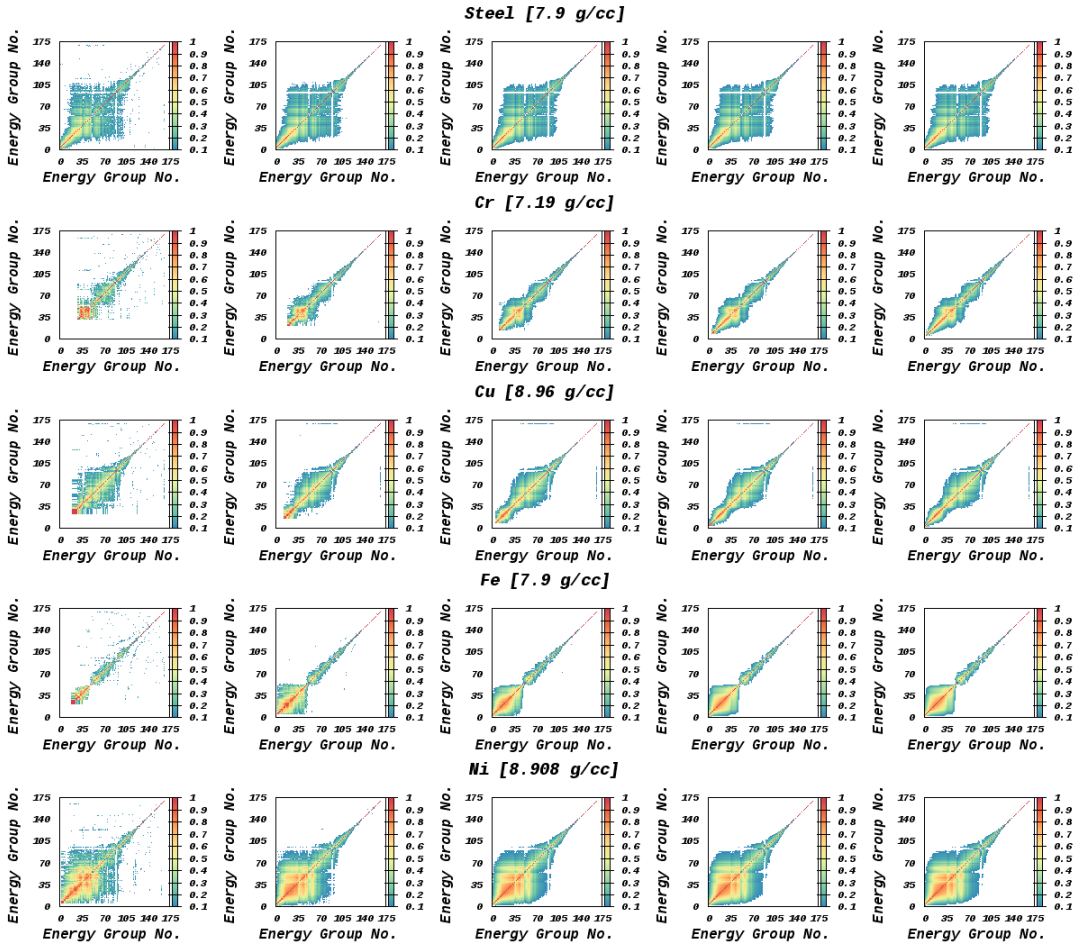

Figure 3.4: Convergence of the Correlation Matrices. Number of Histories; 10^3 (far left), 10^4, 10^5, 10^6, 10^7 (far right)

3.4.2.3 Convergence: Boundary Conditions

To study the effect of problem settings on the correlation matrix, two parameters where considered; the neutron source and BCs. Two cases for each parameter where studied on a cube with uniform Steel (SS316L) and the correlation matrix was calculated in each case as shown in Fig. (3.5). The changes were found to affect the statistics of the obtained energy dependent fluxes and resulted in a change in the relative magnitudes of some correlation coefficients while each matrix still

resembles the pattern for Steel to some extent, as expected.

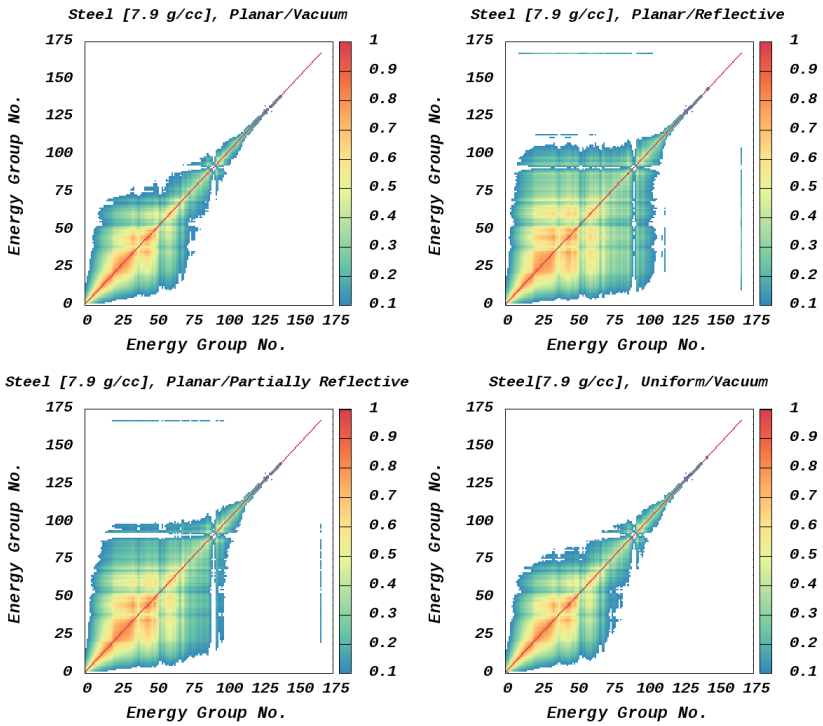

Figure 3.5: The Effect of Source Type & BCs on the Correlation Matrix for Steel (SS316L)

The first change is the BCs, the effect of which could be seen by comparing the mapping of the correlation matrix obtained for the planar source using vacuum, reflective, partially reflective (reflective on three sides and vacuum on the other three) BCs. Using reflective boundary conditions, neutrons are forced to stay in the medium and interact and as a result populate the lower energy bins and this is apparent by comparing the top two subfigures on Fig. (3.5). On the top-right subfigure, where reflective BC was used, it can be seen that the correlation between some energy groups becomes relevant and the figure spreads more near lower energies compared to the top-left subfigure where vacuum BCs were used. Comparing the bottom-left subfigure where partially reflective BCs were used to the top two subfigures, it can be seen that the correlation matrix is somewhat between

the top two cases. This is suggestive that, as was the case for subsets discussed previously for different source energies, the correlation matrix for a flux with all energy groups populated with low uncertainty is inclusive of lower cases where uncertainty is higher due to missing correlation coefficients at lower energy groups. In other words, the correlation matrix for a flux with high uncertainty is a subset of the correlation matrix for a flux with low uncertainty, with the material composition fixed.

The second change is the source type, a planar source with particles directed to the cube will have less lost particles from the medium compared to a uniform isotropic source distributed inside the cube (using vacuum BCs in both cases). Such changes affect the population of neutrons inside the cube and directly affect the statistical uncertainty of the obtained fluxes. For example, histories in the uniform case might be terminated before having a chance to score in lower energy bins due to leakage outside the cube. This can be seen by comparing the top-left and bottom-right subfigures on Fig. (3.5). From both conditions it can be said that the effect of boundary conditions is more relevant than that of changing the source type.

3.5 Implementation of the Correlation Matrix

In the previous section, the properties of the correlation matrix were discussed. From the discussion, it was concluded that the correlation matrices are mainly dependent on nuclear cross sections which govern how neutrons behave in a medium. Decomposition of the correlation matrix after a change was introduced in the problem settings and comparing it to a reference matrix will shed more light on the matrix properties. As discussed in previous sections, the effect of changing the problem settings (source type & spectrum and BCs) can be perceived as having a direct effect on the population of neutrons at different energy groups. As a result, it is possible to decompose the correlation matrix of a system into its basic components.

3.5.1 Correlation Decomposition

Assume we have a cube with specific settings (source type & spectrum, BCs, and material composition) and we obtained the correlation coefficient between the neutron fluxes at two different energy groups, $\mathrm{Corr}(\hat{x}, \hat{y})$, call it ref_A. Now assume a change was made to the BCs, such change will have direct impact on the population of neutrons at the two energy groups and the new correlation coefficient would be, $\mathrm{Corr}(\hat{x} + \delta\hat{x}, \hat{y} + \delta\hat{y})$, call it ref_B. The new correlation coefficient, ref_B, can also be expressed as in Eq. (3.9) (full derivation is given by Appendix A.1).

$$\begin{aligned}\mathrm{Corr}(\hat{x} + \delta\hat{x}, \hat{y} + \delta\hat{y}) = \mathrm{Corr}(\hat{x}, \hat{y})\frac{\sigma_{\hat{x}}\sigma_{\hat{y}}}{\sigma_{\hat{x}+\delta\hat{x}}\sigma_{\hat{y}+\delta\hat{y}}} + \mathrm{Corr}(\hat{x}, \delta\hat{y})\frac{\sigma_{\hat{x}}\sigma_{\delta\hat{y}}}{\sigma_{\hat{x}+\delta\hat{x}}\sigma_{\hat{y}+\delta\hat{y}}} \\ + \mathrm{Corr}(\delta\hat{x}, \hat{y})\frac{\sigma_{\delta\hat{x}}\sigma_{\hat{y}}}{\sigma_{\hat{x}+\delta\hat{x}}\sigma_{\hat{y}+\delta\hat{y}}} + \mathrm{Corr}(\delta\hat{x}, \delta\hat{y})\frac{\sigma_{\delta\hat{x}}\sigma_{\delta\hat{y}}}{\sigma_{\hat{x}+\delta\hat{x}}\sigma_{\hat{y}+\delta\hat{y}}} \quad (3.9)\end{aligned}$$

The four main components are; ref_A correlation value, $\mathrm{Corr}(\hat{x}, \hat{y})$, correlation between the neutron flux in one energy group and the change introduced to the flux at the other energy group due to the change in BCs, $\mathrm{Corr}(\hat{x}, \delta\hat{y})$ & $\mathrm{Corr}(\delta\hat{x}, \hat{y})$, and finally the correlation between the changes in the fluxes at the two energy groups, $\mathrm{Corr}(\delta\hat{x}, \delta\hat{y})$. By examining each term it can be seen that the four terms are just re-normalization of the respective covariances by the product of the standard deviations in the problem after the change in the BCs, $\sigma_{\hat{x}+\delta\hat{x}}\sigma_{\hat{y}+\delta\hat{y}}$. By the hypothesis of uniqueness and as the material composition is the same in the problem before and after the change in BCs, the four correlation terms are expected to be similar.

To examine the possible similarity between the four correlation coefficients, analysis was performed on a simple problem. The problem consists of a cube filled with Steel (SS316L) with reflective BCs on all sides but the side facing a planar boundary source emitting 14.1 MeV neutrons. Neutron transport was performed using MCNP5 and the distribution of histories scores over 175 energy groups was obtained by processing MCNP output ptrac file and the *reference* correlation matrix was obtained, ref_A. A change was then introduced to the boundary conditions by removing all reflective BCs, changing to vacuum BCs and a *new* correlation matrix was obtained for the problem, ref_B. Having calculated the distribution of histories

scores, the correlation between the reference fluxes and the changes in the fluxes in the new problem were also calculated.

A mapping of $\mathtt{ref}_A$ and $\mathtt{ref}_B$ correlation matrices, as well as the matrix obtained for the new problem using Eq. (3.9), *calculated* correlation matrix, are shown in the Fig. (3.6). As seen on the figure by comparing the subfigures for $\mathtt{ref}_A$ and $\mathtt{ref}_B$, the mapping of $\mathtt{ref}_A$ for energy groups below 115 is wider than that for $\mathtt{ref}_B$. This is because reflective BCs force neutrons to remain in the system and populate lower energy groups which results in higher correlation among those groups because of scattering. While both mappings for $\mathtt{ref}_A$ and $\mathtt{ref}_B$ are slightly different, using Eq. (3.9) the correlation matrix for $\mathtt{ref}_B$ is reproduced. Figure (3.7) shows mappings of the four correlation matrices mentioned before; $\mathtt{Corr}(\hat{x}, \hat{y})$ (ref-ref on the top-left corner), $\mathtt{Corr}(\hat{x}, \delta\hat{y})$ (ref-delta on the top-right corner), $\mathtt{Corr}(\delta\hat{x}, \hat{y})$ (delta-ref on the bottom-left corner), and $\mathtt{Corr}(\delta\hat{x}, \delta\hat{y})$ (delta-delta on the bottom-right corner). The matrices $\mathtt{Corr}(\hat{x}, \hat{y})$ & $\mathtt{Corr}(\delta\hat{x}, \delta\hat{y})$ are similar with the exception of some correlation values missing on the latter. The other two, $\mathtt{Corr}(\delta\hat{x}, \hat{y})$ & $\mathtt{Corr}(\hat{x}, \delta\hat{y})$ are transpose of each other. An interesting observation is that the correlation matrices $\mathtt{Corr}(\delta\hat{x}, \hat{y})$ & $\mathtt{Corr}(\hat{x}, \delta\hat{y})$, have negative values and similar structure to the other two matrices. Such an observation leads to an approximation of the correlation matrix and will be discussed in the following subsection under local approximation.

The conclusion from this discussion is that a correlation matrix for neutron spectrum under some problem settings is just the superposition of other matrices that account for the problem settings individually. In the problem discussed, the correlation matrix for the material with vacuum BCs and planar source was found to be the superposition of four matrices. One matrix accounts for the reference correlation between the different energy groups, correlation obtained with reflective BCs. The other three accounted for the changes of the reference correlation due to a change in the problem settings like the BCs. We can go as far as saying that even considering the cross section as being part of the problem settings, we can obtain a correlation matrix for any material using the four component matrices mentioned above.

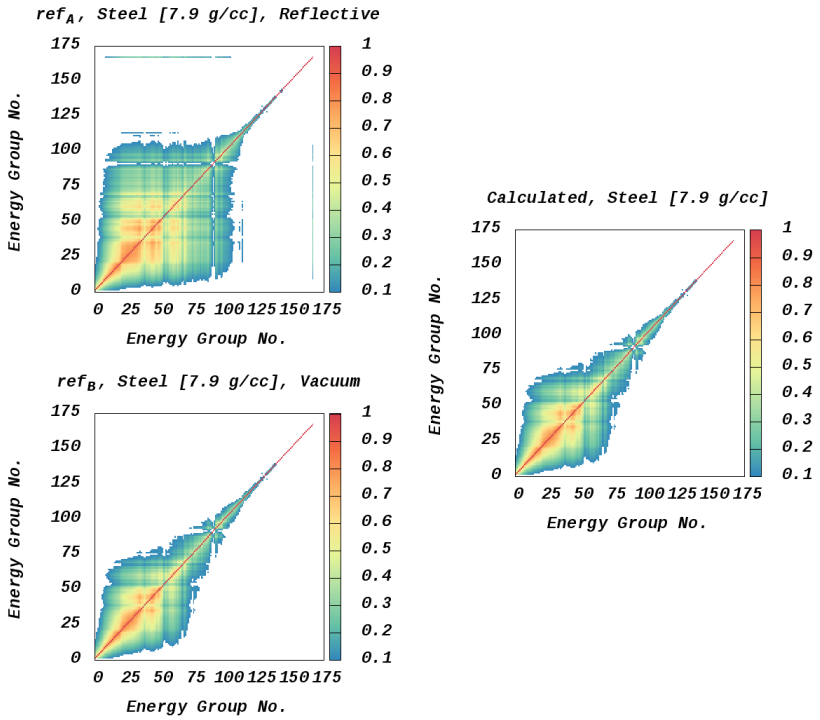

Figure 3.6: Calculating the Correlation Matrix for SS316L Using Reference Matrix

3.5.2 Approximations

The main goal of the correlation matrix approximation, discussed in sections 3.4 & 3.5.1, is to facilitate obtaining the correlation matrices for different materials on simple problems. Also, to validate the application of these matrices to calculate the uncertainty of the photon sources in the respective materials over a mesh where the boundary/source conditions might have changed compared to the conditions under which the matrices were obtained. This is motivated by the fact that producing ptrac files for all histories in complex problems to obtain the correlation matrices over the mesh is prohibitive as the size of such files will in general be large (depending on materials and BCs); a cube problem of $40 \times 40 \times 100$ cm steel and water mixture with 10^6 histories could amount to 100+ GB (ASCII format) file. Two main possible approximations were studied; global and local.

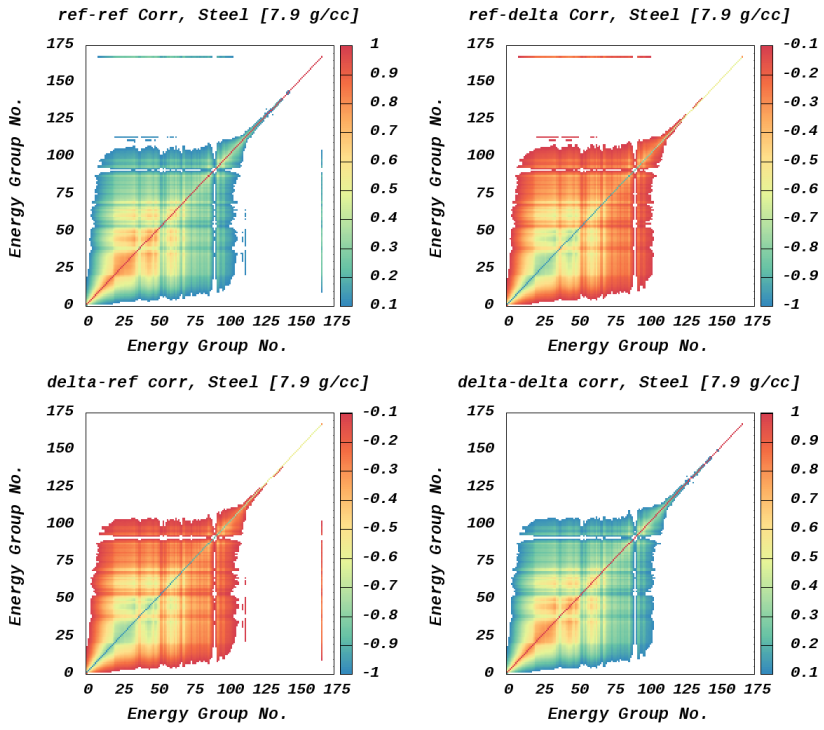

Figure 3.7: Decomposition of the Correlation Matrix for SS316L

3.5.2.1 Global Approximation

In Fig. (3.3) it can be seen that, for the matrices along the diagonal, although reflective BCs were used and neutrons were forced to stay in the system and populate lower energy groups, the matrices in each mesh voxel were slightly different. This could be due to a change in the neutron spectrum which resulted in a change in the relative magnitudes of the correlation coefficients in the matrices. This is to say that the neutron population in each mesh voxel is different resulting from a change in the spectrum. Applying a generic correlation matrix to all mesh voxels across the model with similar material composition will need a correction of some kind. The correction of the correlation matrix has to take into account the local neutron spectrum and the corresponding statistical uncertainty. Using a MCNP meshtally output such a correction can be found by comparing the total standard

deviation from MCNP with that calculated using both the standard deviations of the individual groups from MCNP and the calculated correlation matrix.

The total standard deviation of the neutron flux in a mesh voxel, v, given by MCNP can be expressed as in Eq. (3.10a), where $\sigma_{\phi_{v,E_g^n},\phi_{v,E_{g'}^n}}$ is the covariance between ϕ_{v,E_g^n} and $\phi_{v,E_{g'}^n}$. As MCNP gives the total standard deviation of the neutron flux and the individual standard deviations of each energy group, the covariance term can be calculated and compared against that obtained using the correlation matrix. Comparing the expressions for the covariance term calculated using MCNP values of standard deviations (Eq. (3.10b)) and the one calculated using the correlation matrix (Eq. (3.10c)) will yield a correction factor, Γ, as given in Eq. (3.10d). Although the uncertainty of the neutron flux in each mesh voxel could in general be higher than the case with which the correlation matrix was obtained, it can be thought of as a custom fitting of the correlation matrix to each mesh voxel by re-normalization using the local product of the respective standard deviations of the neutron fluxes.

$$\sigma_{\phi_v}^2 = \sum_g \sigma_{\phi_{v,E_g^n}}^2 + 2 \sum_{\substack{g,g' \\ g<g'}} \sigma_{\phi_{v,E_g^n},\phi_{v,E_{g'}^n}} \tag{3.10a}$$

$$\sigma_{\phi_v}^2 - \sum_g \sigma_{\phi_{v,E_g^n}}^2 = 2 \sum_{\substack{g,g' \\ g<g'}} \sigma_{\phi_{v,E_g^n},\phi_{v,E_{g'}^n}} \tag{3.10b}$$

$$2 \sum_{\substack{g,g' \\ g<g'}} \sigma_{\phi_{v,E_g^n}} \rho(\phi_{v,E_g^n}, \phi_{v,E_{g'}^n}) \sigma_{\phi_{v,E_{g'}^n}} \tag{3.10c}$$

$$\Gamma_v = \frac{\sigma_{\phi_v}^2 - \sum_g \sigma_{\phi_{v,E_g^n}}^2}{2 \sum_{\substack{g,g' \\ g<g'}} \sigma_{\phi_{v,E_g^n}} \rho(\phi_{v,E_g^n}, \phi_{v,E_{g'}^n}) \sigma_{\phi_{v,E_{g'}^n}}} \tag{3.10d}$$

Now the correlation matrix for each mesh voxel, v, can be obtained by applying the correction factor, Γ_v, and the final formula for the standard deviation of the

photon emission density in mesh voxel, v, is given in Eq. (3.11).

$$\sigma^2_{q_{v,E_h^p}} = \sum_g T^2_{v,E_h^p,E_g^n} \sigma^2_{\phi_{v,E_g^n}} + 2\Gamma_v \sum_{\substack{g,g' \\ g<g'}} T_{v,E_h^p,E_g^n} \sigma_{\phi_{v,E_g^n}} \rho(\phi_{v,E_g^n}, \phi_{v,E_{g'}^n}) T_{v,E_h^p,E_{g'}^n} \sigma_{\phi_{v,E_{g'}^n}} \tag{3.11}$$

From preliminary analyses, it has been found that such global correction, although easy to apply, underestimates the total uncertainty of the photon emission density. The correlation matrix should be obtained on a problem with all the neutron fluxes at the different energy groups populated with low enough uncertainty. A global correction based on the local spectrum in each mesh voxel is bound to be either missing some energy groups or have high uncertainty in many cases. Although such correction scales all the elements in the correlation matrix by the same amount, hence preserving the unique pattern for the material, it's not advised that such global correction be used. In the following section an example will be given showing how the global correction decreases the estimation of the photon source uncertainty.

3.5.2.2 Local Approximation

Local approximation of the correlation matrix refers to a correction applied to each element in the correlation matrix based on the local neutron spectrum in each mesh voxel. Such a correction derives directly from the correlation matrix decomposition that was presented for one correlation value in Eq. (3.9). While Eq. (3.9) shows the decomposition of the correlation coefficient as a function of four separate correlation components between the distribution of histories scores in the reference and new problem, it is possible to introduce further approximation based on a study of the mapping of the decomposed correlation matrix. In Fig. (3.7), mapping of the four component correlation matrices is shown. It can be seen that the ref-ref and delta-delta matrices - which refer to $\mathrm{Corr}(\hat{x}, \hat{y})$ and $\mathrm{Corr}(\delta\hat{x}, \delta\hat{y})$, respectively - are similar. The other two correlation matrices, ref-delta and delta-ref - which refer to $\mathrm{Corr}(\hat{x}, \delta\hat{y})$ and $\mathrm{Corr}(\delta\hat{x}, \hat{y})$, respectively - are the transpose of each other. Both bear resemblance to the $\mathrm{Corr}(\hat{x}, \hat{y})$ with negative values.

In addition to the mapping of the matrices, analysis of the matrices norms also revealed similarity. The value of three norms are given in Table 3.2. It can be seen from the table that the norms of the four matrices are similar. This is suggestive that a local approximation can be derived as given in Eq. (3.12). The value of such correction term, the sum of four terms in square brackets, can be examined by looking at the ratio of $\mathrm{Corr}(\hat{x} + \delta\hat{x}, \hat{y} + \delta\hat{y})$ and $\mathrm{Corr}(\hat{x}, \hat{y})$. Figure (3.8) shows a mapping of the ratio of $\mathrm{Corr}(\hat{x} + \delta\hat{x}, \hat{y} + \delta\hat{y})$ and $\mathrm{Corr}(\hat{x}, \hat{y})$ for Steel (SS316L) and it can be seen that for the important elements in the correlation matrices (elements with values $\geqslant 0.1$) the ratio is around 1. The result of this analysis adds to the conclusions from the previous discussion on matrix decomposition; the correlation matrix for a voxel in a mesh resembles more the one obtained using reflective BCs (Fig. 3.3) and the correlation matrices are expected to have values > 0 for most materials in FES. It can be said that the best approximation to a correlation matrix in a mesh is one that is obtained using reflective BCs.

Table 3.2: Correlation Matrices Norms

Matrix	1st norm	infinity norm	2nd norm
$\mathrm{Corr}(\hat{x}, \hat{y})$	48.3929	48.3929	36.4389
$\mathrm{Corr}(\hat{x}, \delta\hat{y})$	47.2342	44.6562	34.8845
$\mathrm{Corr}(\delta\hat{x}, \hat{y})$	44.6562	47.2342	34.8844
$\mathrm{Corr}(\delta\hat{x}, \delta\hat{y})$	46.0598	46.0598	35.3403

$$\mathrm{Corr}(\hat{x} + \delta\hat{x}, \hat{y} + \delta\hat{y}) = \mathrm{Corr}(\hat{x}, \hat{y}) \left[\frac{\sigma_{\hat{x}}\sigma_{\hat{y}}}{\sigma_{\hat{x}+\delta\hat{x}}\sigma_{\hat{y}+\delta\hat{y}}} - \frac{\sigma_{\hat{x}}\sigma_{\delta\hat{y}}}{\sigma_{\hat{x}+\delta\hat{x}}\sigma_{\hat{y}+\delta\hat{y}}} - \frac{\sigma_{\delta\hat{x}}\sigma_{\hat{y}}}{\sigma_{\hat{x}+\delta\hat{x}}\sigma_{\hat{y}+\delta\hat{y}}} + \frac{\sigma_{\delta\hat{x}}\sigma_{\delta\hat{y}}}{\sigma_{\hat{x}+\delta\hat{x}}\sigma_{\hat{y}+\delta\hat{y}}} \right] \quad (3.12)$$

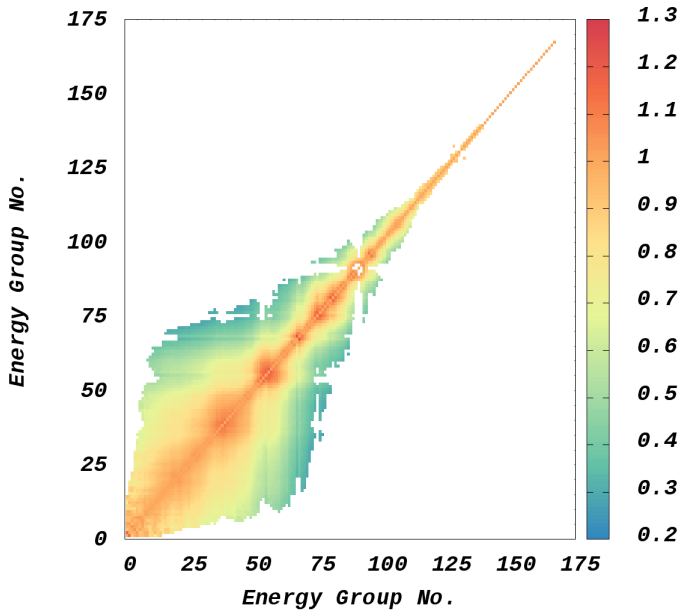

Figure 3.8: Ratio of $\mathrm{Corr}(\hat{x} + \delta\hat{x}, \hat{y} + \delta\hat{y})$ and $\mathrm{Corr}(\hat{x}, \hat{y})$ for Steel (SS316L)

3.6 Demonstration Problem

To complete the analysis on the correction factors and to demonstrate the feasibility of the quantification of the uncertainty of the photon emission density, a demonstration problem has been set up. The problem consists of a source cell, tally cells, and cylindrical region, as shown in Fig. (3.9). The cylindrical region has a radius of 100 cm and has been divided in the z direction according to the radial build of the OB region of the FNSF facility. The cylindrical region consists of a 4 cm first wall (FW), 96 cm breeding zone (BZ), 6 cm He manifold, 3 cm tungsten shell, and finally a 20 cm structural ring (SR). The complete details of the composition of each region and of the FNSF facility can be found in chapter 6.

3.6.1 Neutron Flux Mapping

Figure (3.10) shows a mapping of the total neutron flux in the problem over $10 \times 10 \times 10$ cm^3 mesh. It can be seen that the flux is high at the FW and BZ, at the source

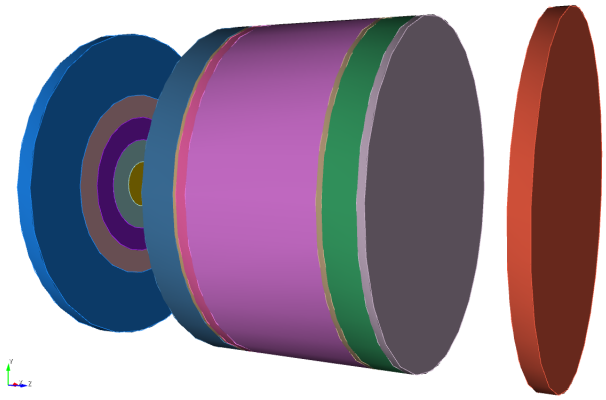

Figure 3.9: Demonstration Problem Based of FNSF OB Radial Build. Source (right) and Tally Cells (left)

side, where the former faces the source and the latter has neutron multipliers. The neutron flux decreases by about three orders of magnitude from the FW to the SR. The statistical uncertainty of the neutron flux in all energy groups in all mesh voxels is $\leqslant 10\%$. For the approximation analyses that follow, the neutron spectrum was obtained at four points along a direction, at x = 60 & y = 60 cm, parallel to the axis of the cylinder corresponding to FW, front of BZ, back of BZ, and SR. The spectrum at the four points is shown in Fig. (3.11). The spectrum shifts to lower energies as we move from the FW to the SR as high energy neutrons attenuate due to interactions with the FW, BZ, shells, etc.

3.6.2 Correlation Approximation Analysis

3.6.2.1 Global Correction

To study the effect of global correction of the correlation matrix on the estimation of the photon source uncertainty, R, the uncertainty was calculated at the four previously mentioned locations; FW, front BZ, back BZ, SR. R was obtained using correlation matrices obtained on reflective BCs one time without correction, R_{ref}, and the second time with global correction applied,R_c . Figure (3.12) shows a plot of the ratio of R_{ref} and R_c, for different irradiation and decay times. The irradiation

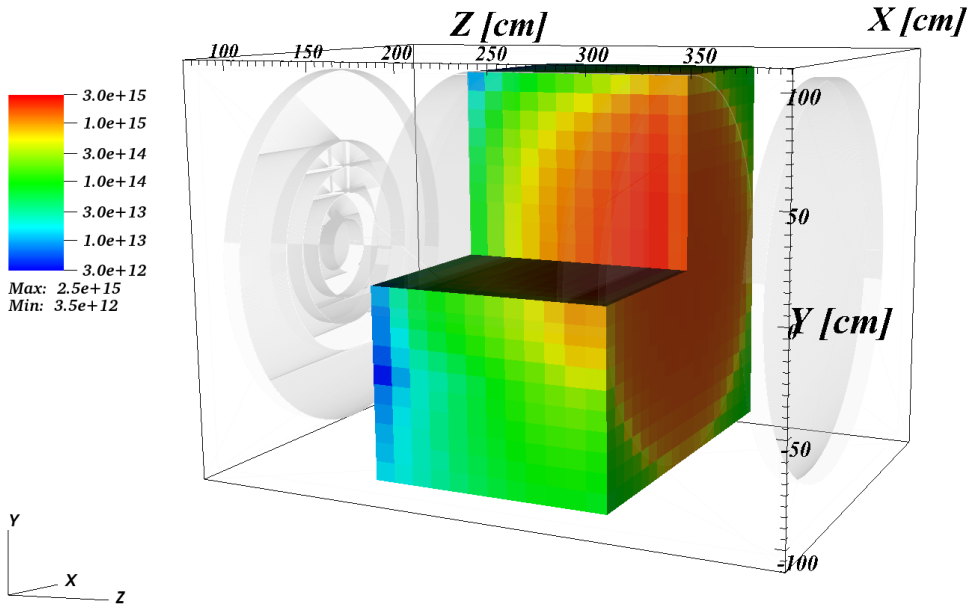

Figure 3.10: Neutron Flux [n/cm^2 · s] Mapping for FNSF Radial Problem

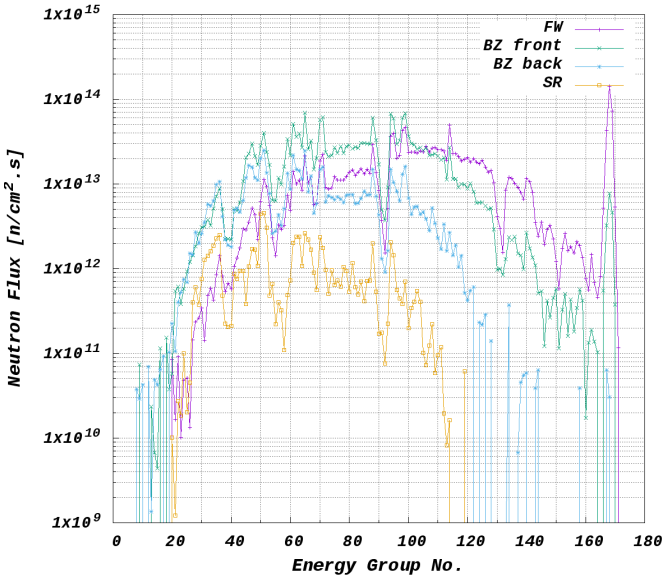

Figure 3.11: Neutron Spectrum [n/cm^2 · s] at FW, BZ, and SR

times chosen are; 10^3, 10^5, 8.7×10^7, and 10^9 s. The decay times chosen are; 0, 10^3, 10^5, 10^7, 10^9 s.

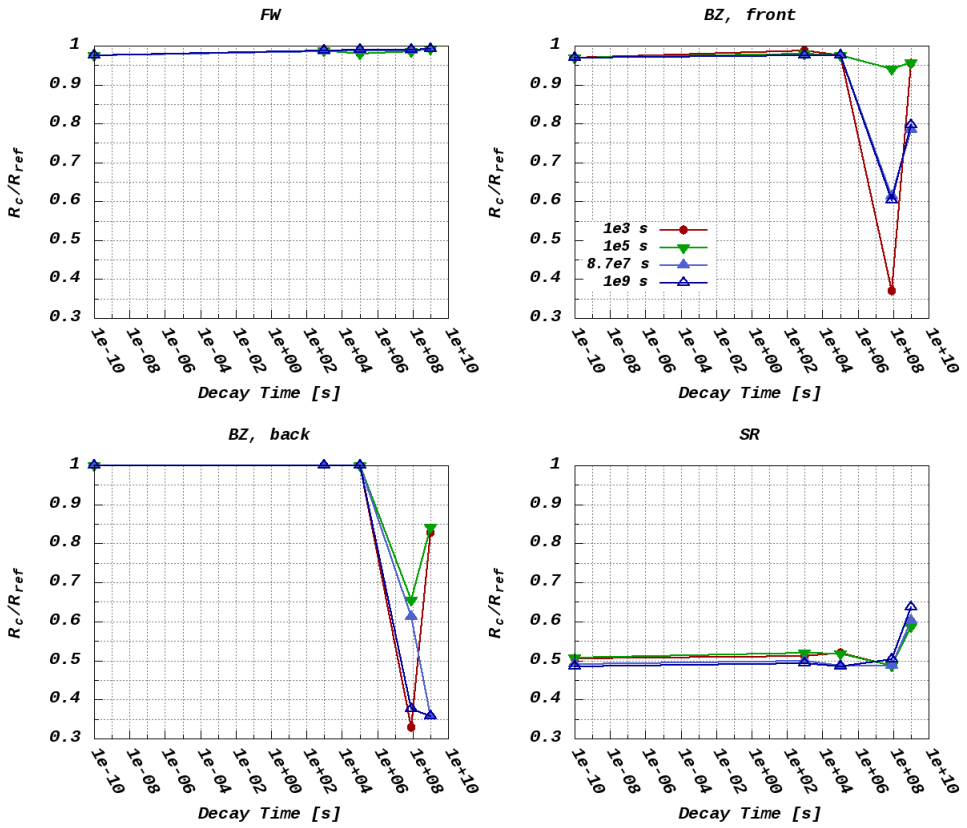

Figure 3.12: Ratio of the Photon Source R with Global Correction Applied to R without Correction

From the figure it can be seen that at the FW the correction factor nearly doesn't introduce any changes to the calculated R. At the BZ it was found that the correction factor lowers the estimate of R especially at high decay times, as well as at the SR. This is due to the fact that some energy groups have higher or missing uncertainty at the BZ and SR such as the higher energy groups where neutrons have already collided and deposited energy in traversing the FW and the first part of the BZ. As a result, the correction factor is expected to be $\leqslant 1$ and will scale down the correlation matrix, hence reducing R of the photon source. Although the same

flux was used for all decay and irradiation times, which means the same correction factor applied, the T matrix has changed. The combined effect of changing T matrix and a correction factor $\leqslant 1$ results in a change in the estimation of the uncertainty at different decay and irradiation times compared to the reference. As a result, the global correction has been rejected for the correlation matrix approximation.

3.6.2.2 Local Correction

To study the effect of using different correlation matrices, R of the photon source was obtained at the four locations mentioned before once using correlation matrices obtained over vacuum BCs, R_{vac}, and another time with matrices obtained over Reflective BCs, R_{ref}. The ratio of R_{vac} to R_{ref} is shown in Fig. (3.13). From the figure, it can be seen that the ratio is nearly 1 for most of the cases at decay times up to 10^5 s. Following that, as decay times gets larger the ratio was found to go below 1 suggesting that R obtained using correlation matrices over vacuum BCs, R_{vac}, underestimates the photon source uncertainty, from a conservative perspective. This aligns with intuition, as discussed before, that as we move deeper into the material the uncertainty of the neutron flux at the differed energy groups gets higher and the correlation matrix will be distorted compared to the original and more accurate one obtained using reflective BCs with all groups populated. A correlation matrix obtained over vacuum BCs will lack some elements that are found in one obtained over reflective BCs. For the FW, it can be seen that while all the neutron energy groups are expected to be populated in the spectrum, using vacuum BCs matrix means ignoring a contribution of some of the energy groups, hence underestimating R of the photon source.

As a result, it's a more acceptable approximation to calculate the correlation matrices over reflective BCs for each material and use it for mesh voxels that contain the respective materials. It's also worth mentioning that, the covariance between the neutron flux at different energy groups goes down with the size of the mesh as more neutrons will have less chance to score in the same mesh voxel at different energies before leaking out. This could mean that calculating the uncertainty of a

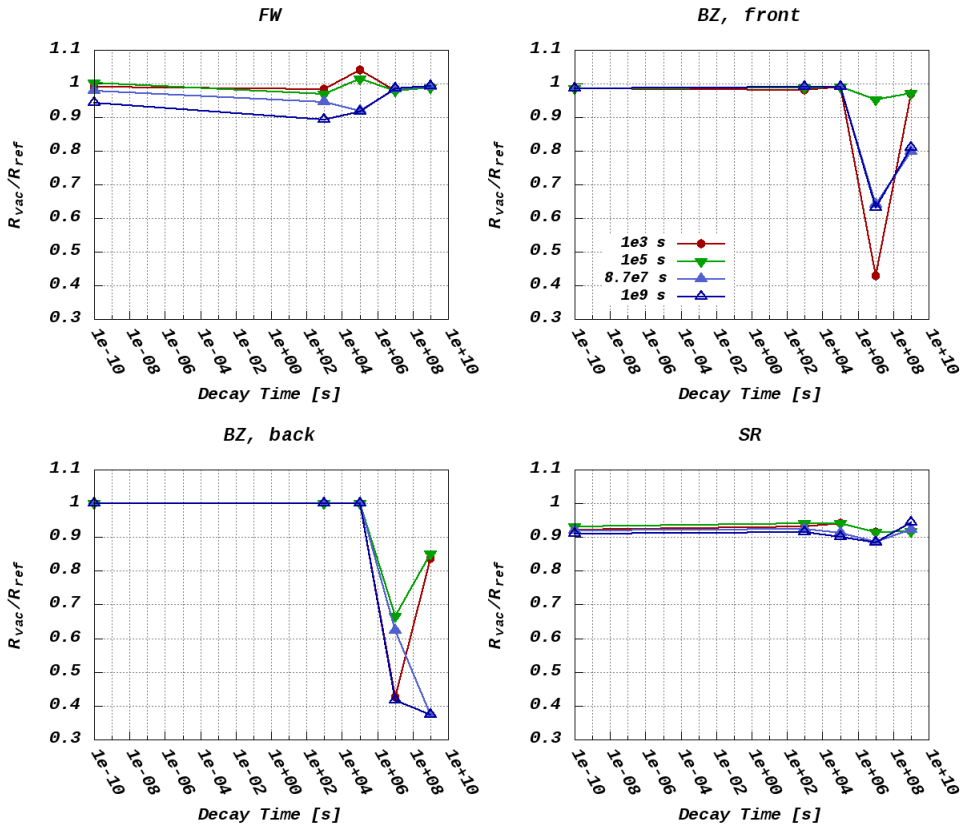

Figure 3.13: Ratio of the Photon Source R with Correlation over Vacuum BCs to R with Correlation over Reflective BCs

photon source over fine mesh will eliminate the sensitivity to the correlation matrix and facilitate applying the local approximation.

3.6.3 Uncertainty Quantification of the Photon Source

To show the estimated uncertainty of the photon emission density, an irradiation time of 10^5 s and a decay time of 0 s have been chosen arbitrarily. Figure (3.14) shows a mapping of the photon emission density obtained using a neutron spectrum over a $10 \times 10 \times 10$ cm^3 spatial mesh. The planar source is at the right side of the figure and it can be seen that the photon emission density is high in the FW and first

few centimeters of the BZ facing the source. This is mainly due to lead which is present in both layers and is the main contributor to the photon emission density. The photon emission density goes down by about four orders of magnitude from the FW to the back end of the SR. Figures (3.15 & 3.16 & 3.17) show the minimum R, R obtained using correlation matrices, and maximum R of the photon emission density, respectively. It can be seen from the figures that the calculated R of the photon emission density is closer to the minimum value. Also, it's worth noting that R is high near the end of BZ and beginning of the SR at 250 cm due to a high local photon emission density due to the presence of the tungsten shell and a high uncertainty of the neutron flux at that region.

Figure (3.19) shows a mapping of R of the photon emission density obtained using a neutron spectrum over a $5 \times 5 \times 5$ cm^3 spatial mesh. It can be seen by comparing figures (3.16) and (3.19) that the uncertainty of the photon source at 250 cm went up as a result of using a finer mesh. This is expected since R of the neutron flux will become larger as the mesh size gets smaller.

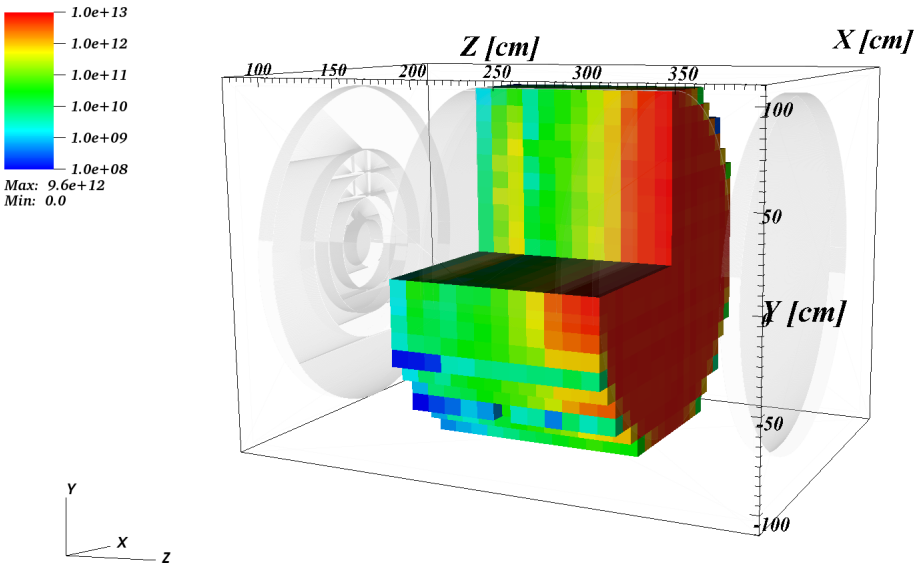

Figure 3.14: Photon Emission Density [p/cm^3 · s] Distribution over a $10 \times 10 \times 10$ cm^3 Mesh for 10^5 s Irradiation and 0 s Decay Times

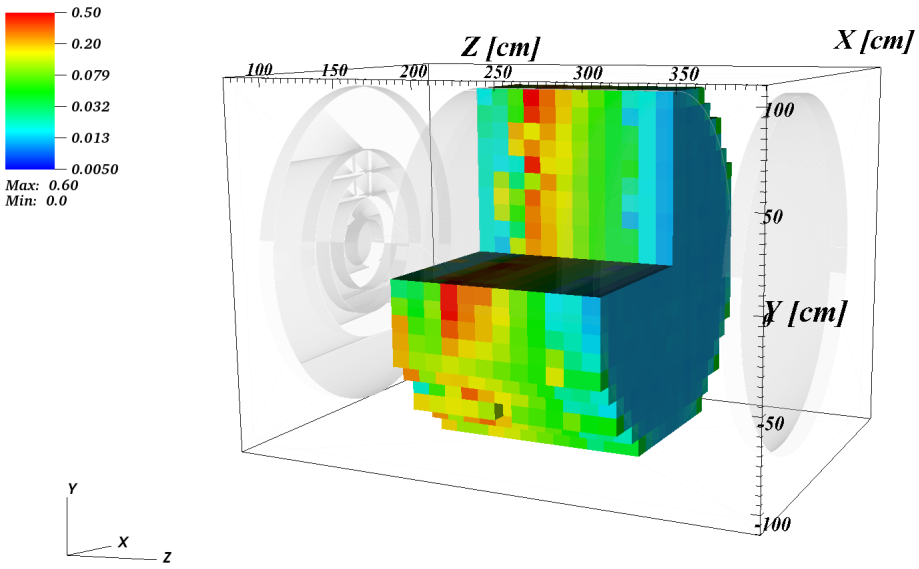

Figure 3.15: Minimum R of the Photon Emission Density over a $10 \times 10 \times 10$ cm^3 Mesh for 10^5 s Irradiation and 0 s Decay Times

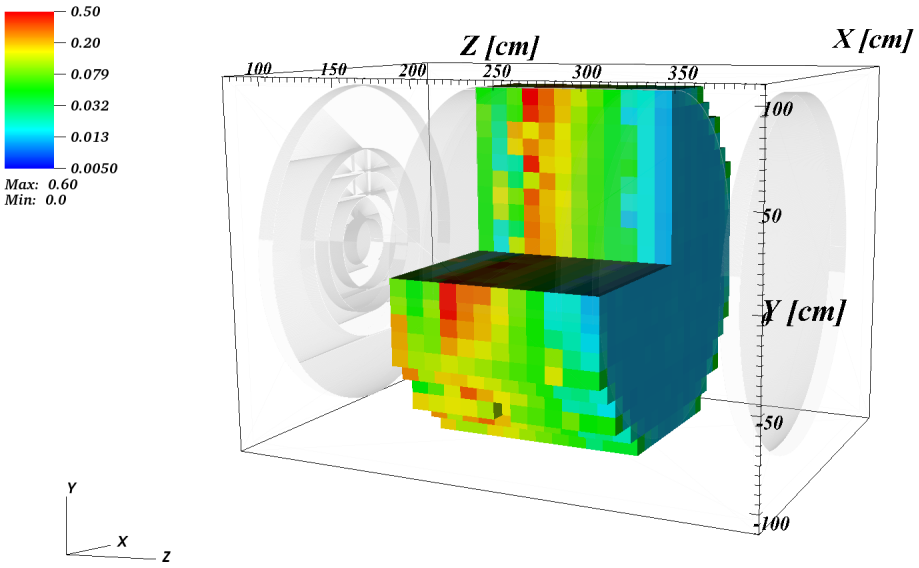

Figure 3.16: R of the Photon Emission Density (Obtained Using Correlation Matrices) over a $10 \times 10 \times 10$ cm^3 Mesh for 10^5 s Irradiation and 0 s Decay Times

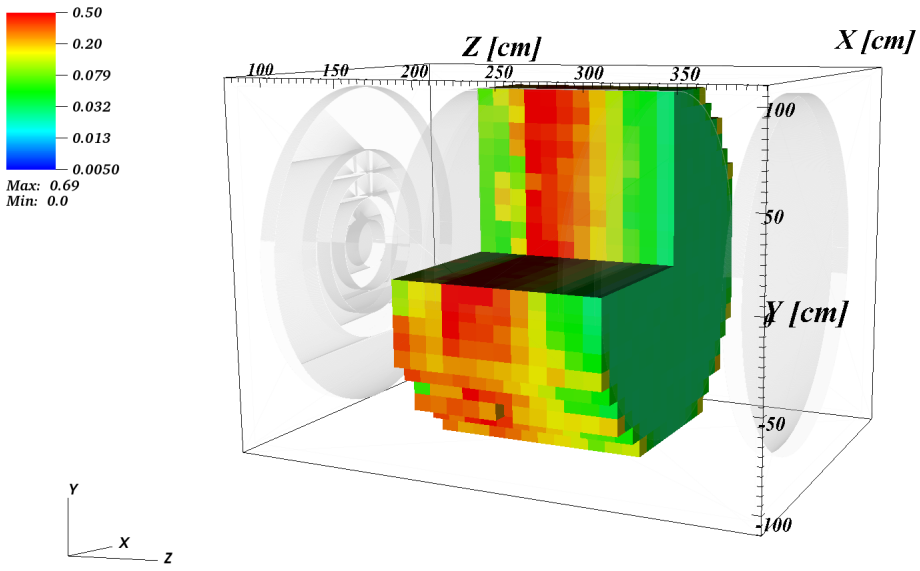

Figure 3.17: Maximum R of the Photon Emission Density over a $10 \times 10 \times 10$ cm^3 Mesh for 10^5 s Irradiation and 0 s Decay Times

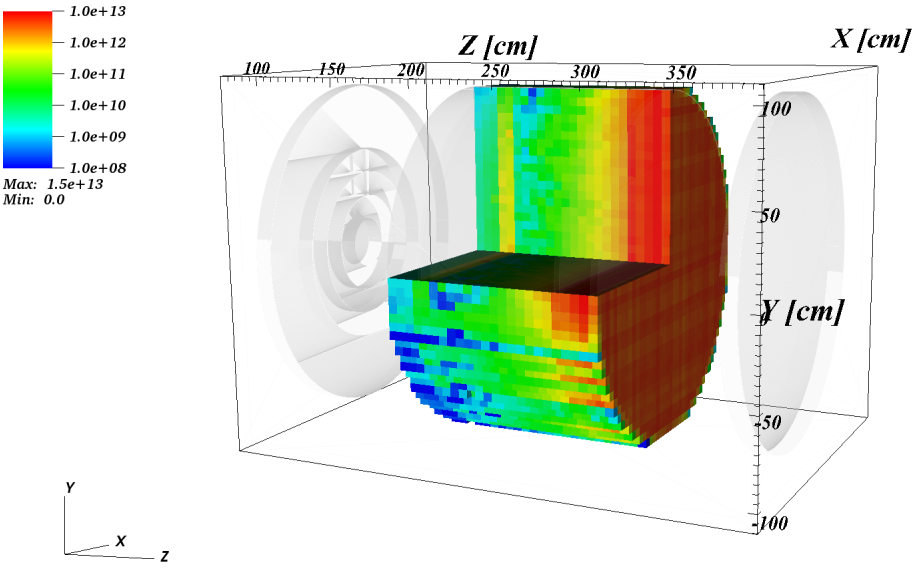

Figure 3.18: Photon Emission Density [p/cm^3 · s] Distribution over a $5 \times 5 \times 5$ cm^3 Mesh for 10^5 s Irradiation and 0 s Decay Times

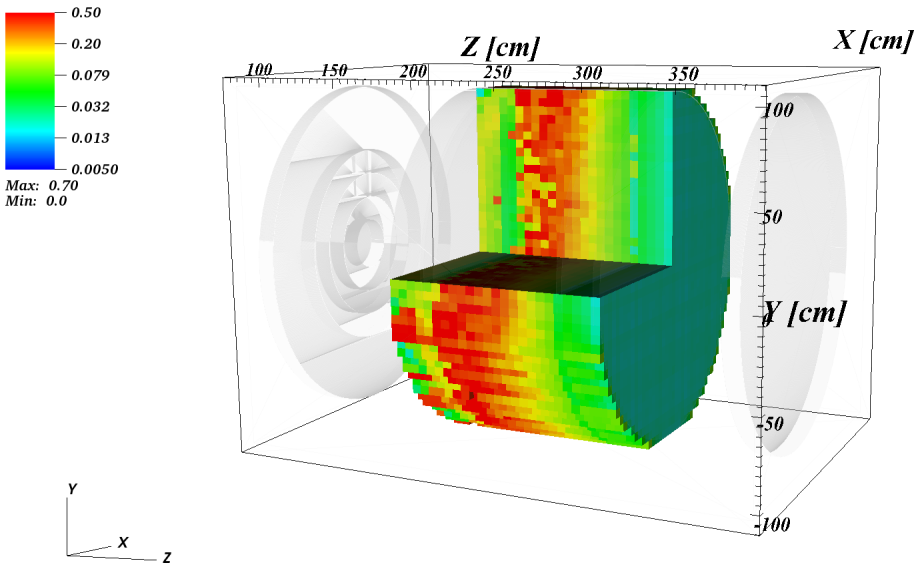

Figure 3.19: R of the Photon Emission Density (Obtained Using Correlation Matrices) over a $5 \times 5 \times 5$ cm^3 Mesh for 10^5 s Irradiation and 0 s Decay Times

3.7 Conclusions

In this chapter, the standard error propagation technique was applied to an expression of the photon emission density yielding an expression for the uncertainty that results from that of the neutron flux distribution in MC simulations of FES. Analyses have been conducted to study the correlation between the neutron fluxes at different energy groups and it lead to the discovery of some characteristics of the correlation coefficients such as uniqueness and convergence. Building on the discovered properties, approximations where studied to facilitate the quantification of the uncertainty of the photon emission density. While the derived formula for the photon emission uncertainty can be efficiently used to estimate the upper and lower bounds, analyses showed that the correlation matrices for different elements/mixtures can be obtained separately and used to estimate the uncertainty over a mesh and is considered a good approximation to the correlation coefficients. The developed method has been demonstrated on a simple cylindrical problem using the neutron spectrum over two different mesh configurations.

4 UNCERTAINTY QUANTIFICATION OF THE PHOTON SOURCE II (R2SMESH WORKFLOW)

4.1 Introduction

One variation of the R2S method [17] aimed at improving the spatial resolution of the photon source distribution, potentially increasing the computational cost in two ways. The first potential cost is in maintaining a reasonable statistical uncertainty across all neutron flux groups as mesh voxels shrink. In addition, there is a cost associated with each nuclear inventory calculation, with one for each mesh voxel. To reduce the number of activation calculations, the photon source is obtained using a neutron energy spectrum with high energy resolution on a coarse spatial mesh, also reducing the computational cost of achieving reasonable statistical errors. The photon source distribution is then scaled with a total neutron flux distribution over the desired fine mesh and the resulting source distribution is used to calculate the SDR.

4.2 Theory

The photon emission density at point $\vec{r}$ and energy E^p, $q(\vec{r}, E^p)$, resulting from the decay of nuclides produced by the interaction of neutrons with the material at point $\vec{r}$ can be expressed as;

$$q(\vec{r}, E^p) = \int_{E^n} T(\vec{r}, E^p, E^n)\phi(\vec{r}, E^n)\, dE^n \tag{4.1}$$

where superscripts n and p denote neutron and photon, respectively and T is a transformation function that encapsulates information about the material composition, interaction cross sections, irradiation scenario, etc. and is defined by this equation.

Eq. (4.1) can be written in group form by discretization of the neutron and

photon energy ranges. Also a discretization in space is achieved by integrating over a range of $\vec{r}$ corresponding to the size of a mesh voxel centered at location r_f. The discretized form is then:

$$q(r_f, E_f^p) = \sum_{E_f^n} T(r_f, E_f^p, E_f^n)\phi(r_f, E_f^n) \tag{4.2}$$

where f refers to a "fine" space/energy interval such that r_f denotes a fine mesh voxel, E_f^p is a fine photon energy group, E_f^n is a fine neutron energy group, and $\phi(r_f, E_f^n)$ is the neutron flux in a fine mesh voxel as a function of the fine energy groups.

As pointed out in section 4.1, the modified R2S workflow uses a high energy resolution neutron spectrum over a coarse spatial mesh, $\phi(r_c, E_f^n)$, to perform the activation calculations and obtain the photon source distribution over the coarse spatial mesh, $q(r_c, E_f^p)$, which is then scaled by the flux magnitude over a respective fine spatial mesh, $F(r_f, E_c^n)$, to obtain the fine photon source distribution, $q(r_f, E_f^p)$. In the same notation of Eq. (4.2) this can be expressed as:

$$q(r_f, E_f^p) = q(r_c, E_f^p)F(r_f, E_c^n) = \left[\sum_{E_f^n} T(r_c, E_f^p, E_f^n)\phi(r_c, E_f^n)\right] F(r_f, E_c^n) \tag{4.3a}$$

where the subscript c denotes a coarse mesh voxel and the scaling factor F is defined by:

$$F(r_f, E_c^n) = \frac{\phi(r_f, E_c^n)}{\phi(r_c, E_c^n)} = \frac{\phi(r_f, E_c^n)}{\sum_{E_f^n} \phi(r_c, E_f^n)} \tag{4.3b}$$

4.3 Constructed Mesh-Based Fluxes

The method defined by Eq. (4.3a) is related to another procedure where the flux distribution in Eq. (4.2), $\phi(r_f, E_f^n)$, is replaced by an equivalent distribution "constructed" from two separate neutron transport results, a high spatial resolution (fine r & coarse E) and a spectrum with high energy resolution over a coarse spatial mesh

(coarse r & fine E). Although the total neutron flux is preserved, the distribution in each fine spatial mesh is altered by the scaling process that imposes the shape of the neutron energy spectrum in each coarse mesh on every fine mesh that it constitutes. The concept of constructed fluxes can be expressed as;

$$\phi(r_f, E_f^n) = \frac{\phi(r_f, E_c^n)\phi(r_c, E_f^n)}{\phi(r_c, E_c^n)} \tag{4.4}$$

As the flux intensities are calculated using Monte Carlo (MC) methods, the obtained magnitudes are the mean of scores of many histories normalized to a single source particle and because the mean of a ratio of random variables (histories scores) is not equal to the ratio of their means [31], the expression in Eq. (4.4) is biased and a correction is needed. The corrected formulas for both the mean and its relative error are shown in Eq. (4.5a) and Eq. (4.5b) (the full derivation is given by Appendix A.2),

$$\begin{aligned}\phi(r_f, E_f^n) = \frac{\phi(r_f, E_c^n)\phi(r_c, E_f^n)}{\phi(r_c, E_c^n)} \Bigg[1 - R^2(r_c, E_c^n) - \frac{Cov[\phi(r_f, E_c^n), \phi(r_c, E_f^n)]}{\phi(r_f, E_c^n)\phi(r_c, E_f^n)} \\ + \frac{Cov[\phi(r_f, E_c^n), \phi(r_c, E_c^n)]}{\phi(r_f, E_c^n)\phi(r_c, E_c^n)} + \frac{Cov[\phi(r_c, E_f^n), \phi(r_c, E_c^n)]}{\phi(r_c, E_f^n)\phi(r_c, E_c^n)} + O(3)\Bigg]\end{aligned} \tag{4.5a}$$

$$\begin{aligned}R^2(r_f, E_f^n) = \Bigg[R^2(r_f, E_c^n) + R^2(r_c, E_f^n) + R^2(r_c, E_c^n) + 2\frac{Cov[\phi(r_f, E_c^n), \phi(r_c, E_f^n)]}{\phi(r_f, E_c^n)\phi(r_c, E_f^n)} \\ - 2\frac{Cov[\phi(r_f, E_c^n), \phi(r_c, E_c^n)]}{\phi(r_f, E_c^n)\phi(r_c, E_c^n)} - 2\frac{Cov[\phi(r_c, E_f^n), \phi(r_c, E_c^n)]}{\phi(r_c, E_f^n)\phi(r_c, E_c^n)} + O(3)\Bigg]\end{aligned} \tag{4.5b}$$

where $R(r_c, E_c^n)$ is a relative error for $\phi(r_c, E_c^n)$ and is defined as in Eq. (4.6) and $\sigma_{\phi(r_c, E_c^n)}$ is the standard deviation of $\phi(r_c, E_c^n)$.

$$R(r_c, E_c^n) = \frac{\sigma_{\phi(r_c, E_c^n)}}{\phi(r_c, E_c^n)} \tag{4.6}$$

4.3.1 Convergence of Correction Terms

One of the capabilities of MCNP is that it can produce an output file (ptrac) with all the relevant information of the random walk of each particle as it traverses the medium. For each history, the output file contains information about the location (x, y, z), direction cosines (u, v, w), energy (E), statistical weight (w), etc. at each interaction point along the path from the beginning at the source location up to the termination of the history. This information can be used to calculate the covariance terms. Producing a ptrac file for big models with all the relevant details of the particles histories is exhausting for both memory and computing resources, so attention was directed to the correction terms in Eq. (4.5a) and Eq. (4.5b) for a possible derivation of an approximation for the terms. By solving Eqs. (4.5a) and (4.5b) (see appendix A.4) simultaneously for the condition under which the covariance terms could be ignored, it was found that this condition can be reduced to $R(r_c, E_c^n) << 10\%$. In other words; obtaining the neutron fluxes distributions with acceptable statistics ($R < 10\%$) removes the bias from Eq. (4.4).

To test this hypothesis, analysis was performed by processing MCNP ptrac output files and calculating the constructed fluxes with and without the correction terms. The difference was found to converge as a function of R over the coarse mesh in accordance with the derived condition. Fig. (4.1) shows the relative difference between the corrected flux, $\hat{\phi}$, and the uncorrected flux, $\tilde{\phi}$,

$$\Delta = \frac{\hat{\phi} - \tilde{\phi}}{\hat{\phi}} \tag{4.7}$$

for a tally population as a function of R. The number of histories processed were varied to simulate a change in R over the coarse mesh from high (at 10^3) to acceptable (at 10^6). The calculations were performed for five neutron energy groups with the following upper bounds; 2.8, 5.64, 8.46, 11.28, 14.1 MeV. The choice of the number of energy groups is arbitrary, so five were chosen as it was possible for the simulation to be done in a reasonable time. It is also worth noting that the derivation of the condition ($R < 10\%$) is mathematically correct based on the solution of both

equations (Eq. (4.5a) and Eq. (4.5b)) and is independent of any other problem specific parameters.

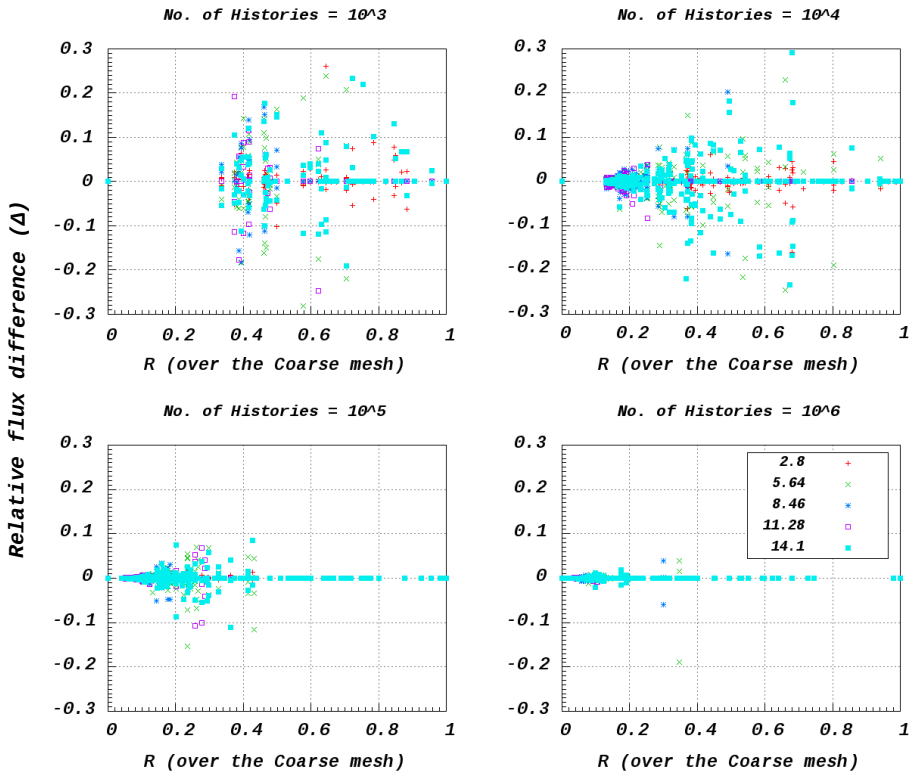

Figure 4.1: Convergence of the Correction Terms in the Construed Flux Formula

4.3.2 Scaled Photon Sources

4.3.2.1 Model

The model used in this study is the ITER shutdown dose rate benchmark problem [32], shown in Fig. (4.2). Because the shielding material will result in a steep flux gradient along the cylinder and variance reduction tools will need to be used, the height of the main cylinder (550 cm) is reduced to 150 cm with all the other dimensions unchanged. A source strength of 10^{18} n/s was used with a simple

irradiation scenario which consisted of a single constant pulse for 4 years with the calculation of photon source distribution at shutdown (0 s).

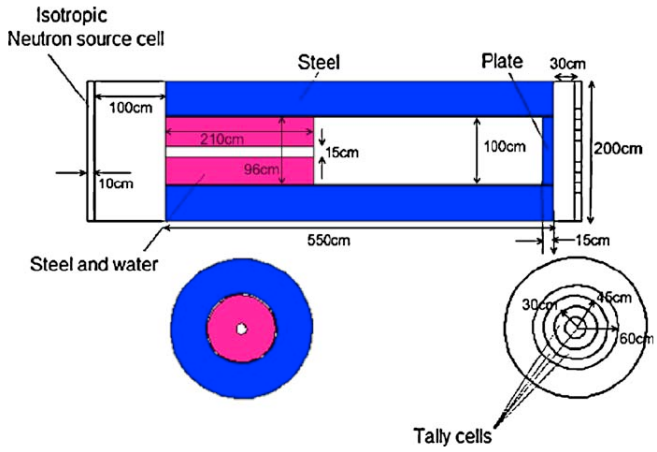

Figure 4.2: ITER Shutdown Dose Rate Benchmark [32]

4.3.2.2 Difference in Neutron Flux Mapping

Although ignoring the correction terms under the condition introduced in the previous subsection will yield unbiased constructed fluxes, another source of error is introduced in the construction process. This approximation error can be seen by mapping the difference between fluxes obtained by single-run using MCNP and by construction as described in Eq. (4.4), relative to the standard deviation of the MCNP result in each mesh voxel. Fig. (4.3) shows a mapping of the relative difference, expressed as multiples of the relative error, along mesh voxels parallel to the axis of the cylinder with their center at $(x, y) = (-10, -10)$ cm (10 cm away from the axis of the cylinder). The fine mesh used for MCNP run is $20 \times 20 \times 6.19$ cm^3 with 5 energy groups covering a range from 0 - 14.1 MeV. For construction of fluxes the fine mesh used is $20 \times 20 \times 6.19$ cm^3 with one energy group and the coarse mesh is $20 \times 20 \times 18.56$ cm^3 with 5 energy groups.

From the mapping it can be seen that the constructed fluxes deviate from MCNP results in most of the space-energy mesh and in some of them by more than 3

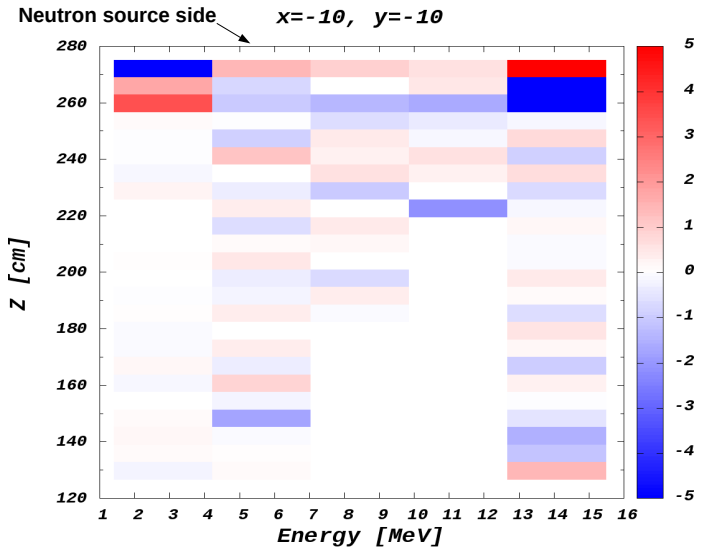

Figure 4.3: Flux Difference (MCNP Flux - Constructed Flux) as Multiples of the Standard Deviation of MCNP Flux

standard deviations. This is caused by scaling which imposes the spectrum shape in the coarse mesh on every fine mesh voxel it constitutes. This scaling does not take into account changes in the flux gradient for all energy groups over space due to averaging over a coarse mesh. Considering the three voxels nearest the source ($z = 275$ cm), the course mesh spectrum is softer than the reference spectrum in the first voxel and harder than the reference spectrum of the third voxel.

4.3.2.3 Difference in Photon Source Distribution

The photon source distribution and SDR were calculated for three different cases. A *reference* case using a neutron flux distribution over $8 \times 8 \times 3.3$ cm^3 and 175 energy groups, a second case using *constructed* fluxes with $8 \times 8 \times 3.3$ cm^3 and one energy group for the fine spatial flux and $8 \times 8 \times 9.9$ cm^3 and 175 energy groups for the energy spectrum, and a final case with the photon emission density calculated using a flux over $8 \times 8 \times 9.9$ cm^3 and 175 energy groups which is then *scaled* by the fine mesh flux $8 \times 8 \times 3.3$ cm^3 with one energy group.

In Fig. (4.4), by comparing the mapping of the photon emission density (top

row of subfigures) for the 6^{th} photon energy group two differences are apparent. The first is that the photon source near the closure plate at the left edge of the *scaled* case covers a region of vacuum since the source is based on a coarse spectrum that is averaged over a region that contains vacuum. This necessitates a correction of some kind to be applied when sampling the source to avoid sampling photon source particles in the vacuum region. The second is that the strength of the source is different especially near the neutron source (240 - 275 cm). Although the distribution is similar in shape, the magnitude is different in regions with the highest photon emission.

On the middle bottom sub-figure, mapping of the difference between the *reference* and *scaled* photon sources shows a pattern similar to that in Fig. (4.3). These differences originate from a similar effect as described in the previous section, in which the approximation in the neutron spectrum does not properly account for different gradients in different neutron energy groups within a coarse mesh voxel.

The similarity between the *scaled* and *constructed* photon source distribution mapping - which can be seen quantitatively from the mapping of the {*Constructed - scaled*} difference on the bottom left subfigure - confirms that the *scaled* method is equivalent to the *constructed* flux method. The similarity between the differences; {*reference - scaled*} and {*reference - constructed*} also supports that hypothesis. Although similar in shape, differences exist in the source magnitudes in many mesh voxels and both methods, *scaled* and *constructed*, give different results for the photon flux and SDR compared to the *reference* case as will be discussed in the following subsection.

4.3.2.4 SDR Results

Both the photon flux and the shutdown dose rate were calculated at the tally cells defined in Fig. (4.2). Table 4.1 gives the results for case 1, based on the results presented in Fig. (4.4): $8 \times 8 \times 3.3$ cm^3 and $8 \times 8 \times 9.9$ cm^3 for fine and coarse spatial meshes, respectively. At such small size of the coarse mesh, changes in the flux gradient are captured well enough for the *scaled* results to approach those of

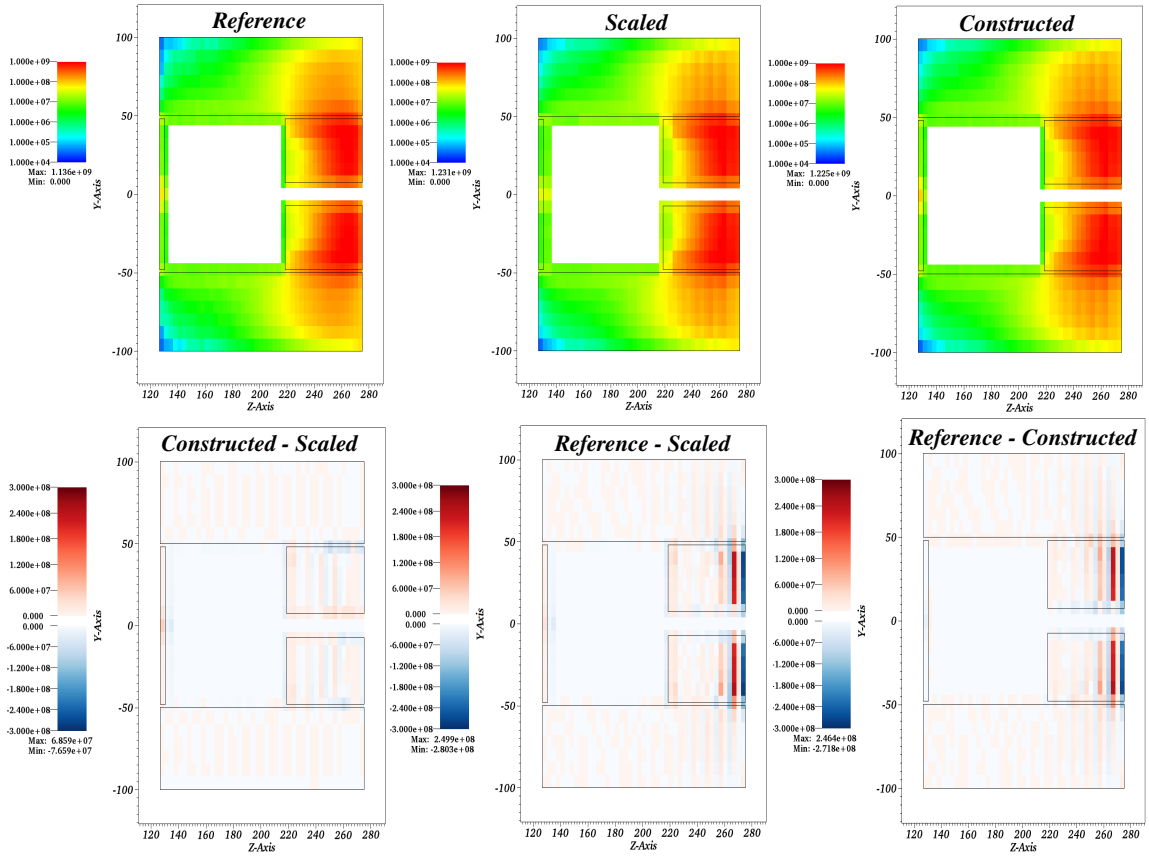

Figure 4.4: Mapping the Photon Emission Density [$p/cm^3 \cdot s$] (sliced at x = 0 cm)

reference and *constructed*.

As the coarse mesh size is made larger (as it should be with the new R2S workflow, *scaled* method) it can be shown that the scaled results begin to diverge from both the *reference* and *constructed*. Table 4.2 gives the results for case 2 in which the SDR is calculated over a different mesh: $8 \times 8 \times 9.9$ cm^3 and $8 \times 8 \times 29.7$ cm^3 for the fine and coarse meshes, respectively.

4.3.2.5 Difference in Photon Flux

Fig. (4.5) shows the results for the photon flux in the tally cells for cases 1 and 2. In both cases the photon flux for the *scaled* method is lower than those from either the

Table 4.1: SDR [μ Sv/h] for Case No. 1

	Reference	Scaled	Constructed
r=15 [cm]	3.578×10^9	3.341×10^9	3.569×10^9
r=30 [cm]	2.982×10^9	2.913×10^9	2.921×10^9
r=45 [cm]	3.229×10^9	3.154×10^9	3.139×10^9
r=60 [cm]	2.462×10^9	2.389×10^9	2.396×10^9

Table 4.2: SDR [μ Sv/h] for Case No. 2

	Reference	Scaled	Constructed
r=15 [cm]	3.599×10^9	2.964×10^9	3.610×10^9
r=30 [cm]	2.995×10^9	2.823×10^9	2.929×10^9
r=45 [cm]	3.227×10^9	3.135×10^9	3.129×10^9
r=60 [cm]	2.457×10^9	2.420×10^9	2.393×10^9

reference method and *constructed* flux method, especially for the center tally cells. Since the only difference between these cases is the space-energy photon source distribution, these differences has to be directly related to the altered photon source distribution due to scaling compared to using a one step neutron transport over the desired mesh to perform activation calculations.

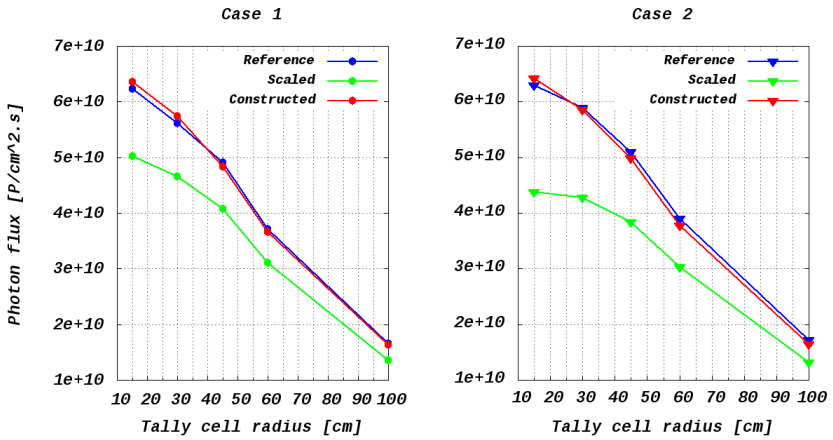

Figure 4.5: Photon Flux [$p/cm^2 \cdot s$] at the Tally Cells

4.3.2.6 Remarks

From the above discussion three points were made clear. The first is that using the new R2S workflow (*scaling* the photon source) gave similar results to the original R2S workflow for coarse meshes "fine" enough to capture the important details of the flux gradient and the results were comparable only for the SDR. The reason for that could be related to the relative importance of photons at different energy groups to the SDR, in other words the changes in the photon flux were in groups that are less important to SDR. The second point is that using the *scaling* method to calculate the heating or energy deposition might result in different values of the calculated quantities compared to the original R2S workflow as the photon flux at the tally bins was different as a result of the changes introduced to the photon source distribution by the scaling process. Finally, as seen from the flux mapping, some changes in the flux deviate by more than 3 standard deviations of the single-run MCNP value which necessitates a propagation of error to the calculated SDR to test the reliability of the results.

4.4 Statistical Error Propagation: from Neutrons to the Photon Source

In the previous sections, it has been demonstrated that a variation of the R2S workflow [17] that aimed at a reduction in the number of activation calculations along with an increase in the spatial resolution of the obtained photon source distribution was equivalent to the method of constructing the fine r - fine E fluxes using two separate transport simulations. The modified R2S workflow uses a high energy resolution neutron spectrum over a coarse spatial mesh, $\phi(r_c, E_f^n)$, for the activation step to obtain the photon emission density over the coarse spatial mesh, $q(r_c, E_f^p)$. It is then scaled by the total flux magnitude over the desired fine spatial mesh, $F(r_f, E_c^n)$, producing the photon emission density, $q(r_f, E_f^p)$. The final

expression is copied here, Eq. (4.8).

$$q(r_f, E_f^p) = q(r_c, E_f^p)F(r_f, E_c^n) = \left[\sum_{E_f^n} T(r_c, E_f^p, E_f^n)\phi(r_c, E_f^n)\right] F(r_f, E_c^n) \tag{4.8}$$

By analogy to the method for uncertainty quantification of the photon emission density in the R2S workflow, as discussed in chapter 3, the uncertainty of the photon emission density over the coarse spatial mesh can be estimated as shown in Eq. (4.9). By applying the error propagation formula to Eq. (4.8), the uncertainty of the photon emission density over the fine spatial mesh (scaled photon source) can be obtained using Eq. (4.10). Note that the covariance terms in the calculation of the relative error of F_{r_f,E_c^n} are ignored as demonstrated in the derivation of the expression for $\sigma^2_{F(r_f,E_c^n)}$ in Appendix A.3. Also, the covariance between q_{r_c,E_f^p} and F_{r_f,E_c^n} was also ignored since the covariance between ϕ_{r_c,E_f^n} and F_{r_f,E_c^n} where shown to be irrelevant under some conditions per Appendix A.4.

$$\sigma^2_{q_{r_c,E_f^p}} = \sum_{E_f^n} T^2_{r_c,E_f^p,E_f^n}\sigma^2_{\phi_{r_c,E_f^n}} + 2\sum_{E_f^n<E_{f'}^n} T_{r_c,E_f^p,E_f^n}\sigma_{\phi_{r_c,E_f^n}} T_{r_c,E_f^p,E_{f'}^n}\sigma_{\phi_{r_c,E_{f'}^n}}\rho(\phi_{r_c,E_f^n},\phi_{r_c,E_{f'}^n}) \tag{4.9}$$

$$\sigma^2_{q_{r_f,E_f^p}} = (q_{r_f,E_f^p})^2\left[\left(\frac{\sigma_{q_{r_c,E_f^p}}}{q_{r_c,E_f^p}}\right)^2 + \left(\frac{\sigma_{F_{r_f,E_c^n}}}{F_{r_f,E_c^n}}\right)^2\right] \tag{4.10}$$

Similar to the analysis of the uncertainty of the photon source in chapter 3, the minimum and maximum uncertainty could also be obtained for the scaled photon source using Eqs. (4.9) & (4.10). This can be achieved by setting the values of the correlation coefficient, $\rho(\phi_{r_c,E_f^n},\phi_{r_c,E_{f'}^n})$, to 0 or 1 to calculate the minimum and maximum uncertainty, respectively.

4.5 Demonstration Problem

For demonstration, the same model used in section 3.6 is used here. First, the uncertainty of the photon emission density at several decay and irradiation times

was estimated and the ratio between R of the photon sources obtained using the R2Smesh workflow to R of the photon sources from R2S workflow, *reference*, were compared. Figures showing plots of the ratio at four mesh voxels corresponding to FW, front of BZ, back of BZ, and SR are presented. Second, a mapping of the photon emission density at shutdown for an irradiation time of 10^5 s is presented.

4.5.1 Mesh Sensitivity Study

To study the effect of scaling the photon source on the uncertainty, the photon emission density for several fine and coarse mesh combinations were compared to the photon emission density from R2S workflow over the same spatial fine mesh. The photon emission density was obtained in the R2S workflow, *reference*, using a neutron flux distribution over a $10 \times 10 \times 10$ cm^3 spatial mesh and 175 energy groups. The photon emission density was also obtained in the R2S workflow using neutron spectrum over several coarse meshes, $20 \times 20 \times 21$, $40 \times 40 \times 32$, $50 \times 50 \times 42$, and $100 \times 100 \times 64$ cm^3, and scaled using the total neutron flux over $10 \times 10 \times 10$ cm^3 fine spatial mesh.

Figure (4.6) shows a plot of the ratio between R for the photon emission density at the four chosen locations (FW, BZ front, BZ back, and SR) and R of the reference photon emission density obtained in R2S workflow for 10^5 s irradiation time and several decay times; 0, 10^3, 10^5, 10^8, and 10^9 s. It can be seen, except for FW and back BZ regions, that R of the photon source in the new R2S workflow is lower than that of the reference. This can be seen to be mainly due to an overestimation of the photon emission density as shown in Fig. (4.7). In Fig. (4.8) a similar plot is shown for the comparison of R for R2S and R for the modified R2S workflows for a photon source over a $5 \times 5 \times 5$ cm^3 fine spatial mesh.

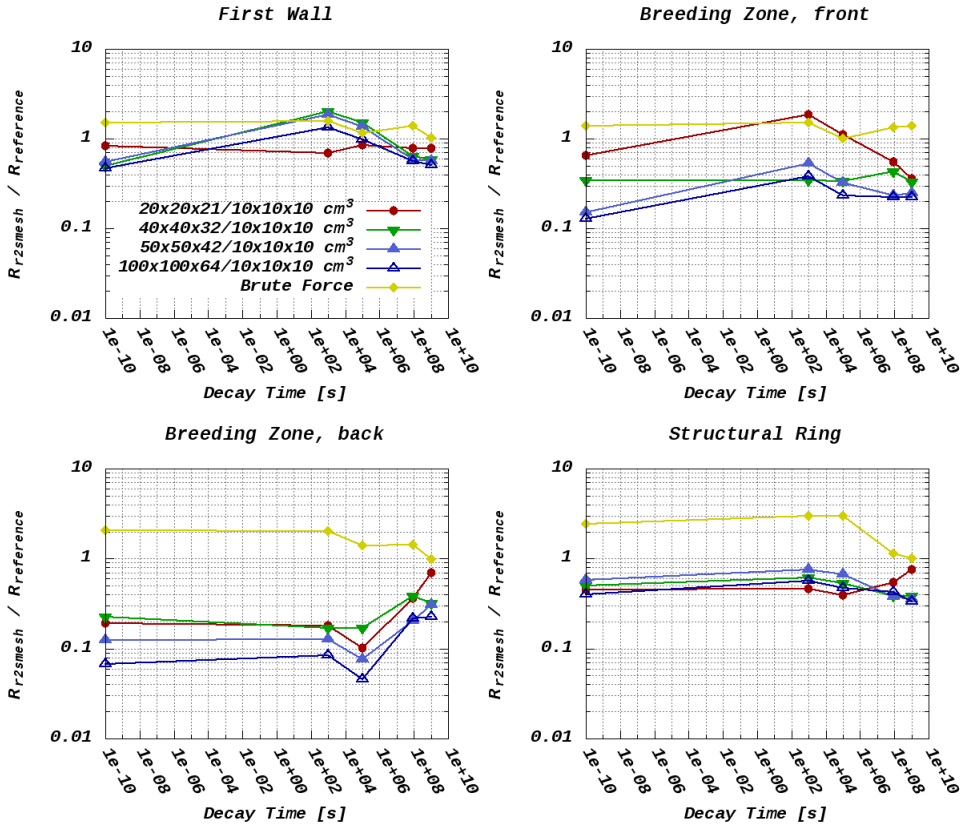

Figure 4.6: Ratio of R at Different Fine-Coarse Mesh Combinations to a Reference $10 \times 10 \times 10$ cm^3 Mesh

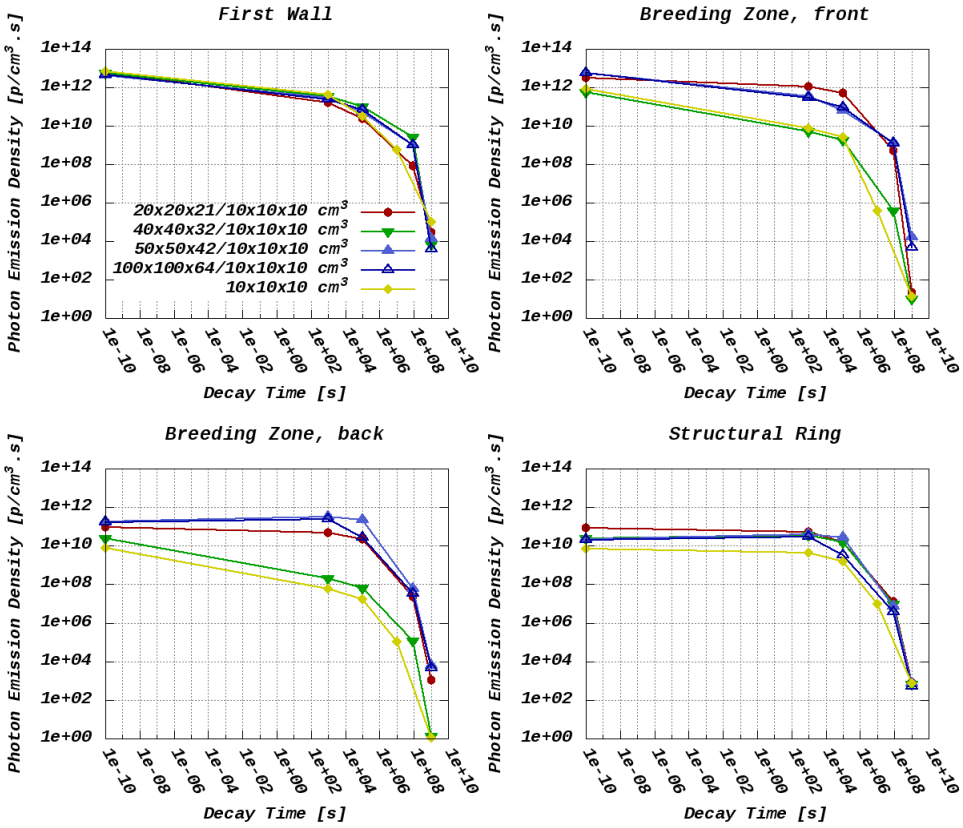

Figure 4.7: Photon Emission Density [$p/cm^3 \cdot s$] Distribution over Different Mesh Configurations

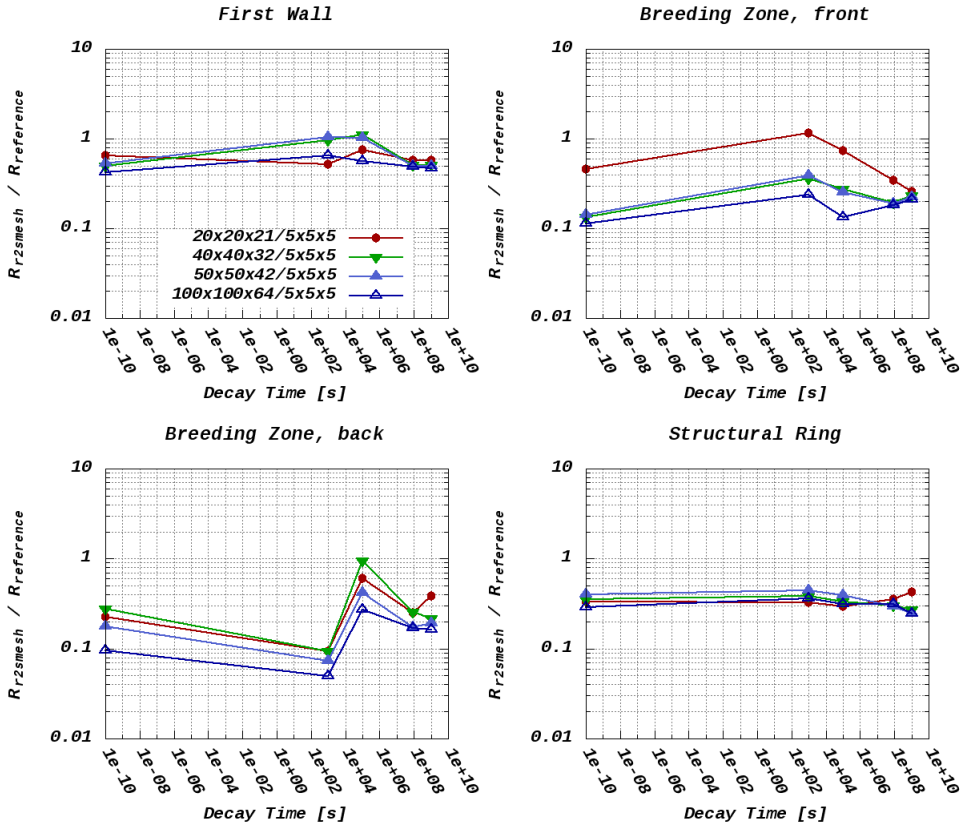

Figure 4.8: Ratio Of R at Different Fine-Coarse Mesh Combinations to a Reference $5 \times 5 \times 5$ cm^3 Mesh

4.5.2 Uncertainty Quantification of the Scaled Photon Source

Figure (4.9) shows a mapping of the photon emission density obtained using $20 \times 20 \times 21$ cm^3 spectrum over a coarse spatial mesh and scaled using a total neutron flux over a $10 \times 10 \times 10$ cm^3 fine spatial mesh. Compared to Fig. (3.14), at the end of chapter 3, it's clear from the strips near the source that the spectrum in each coarse mesh is imposed during the scaling process on every fine mesh it constitutes. This, although acceptable for coarse meshes small enough to resolve the neutron flux gradients, could alter the photon emission density the coarser the mesh becomes. Figures (4.10, 4.11, and 4.12) show the minimum R, R, and maximum R, respectively. As mentioned before in chapter 3, R of the photon emission density obtained using correlation matrices is close to the minimum. Also, it's noticeable that the lowest R of the source occurs near the neutron source where the photon emission density is high. R of the photon emission density near the end of the BZ, Fig. (4.11), is high as the neutron flux is expected to have higher uncertainties in that region being far from the source. Similarly, Fig. (4.13) & (4.14) show mapping for the case of scaling a photon source over a $20 \times 20 \times 21$ cm^3 by the total neutron flux over a $5 \times 5 \times 5$ cm^3 mesh.

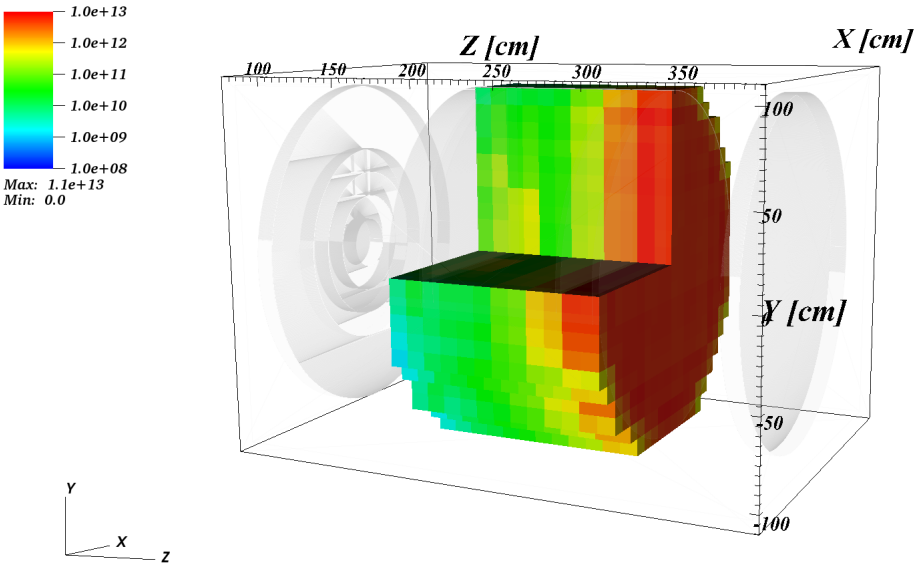

Figure 4.9: Photon Emission Density [p/cm^3 · s] Distribution for 10^5 s Irradiation and 0 s Decay Times, $20 \times 20 \times 21$ cm^3 / $10 \times 10 \times 10$ cm^3

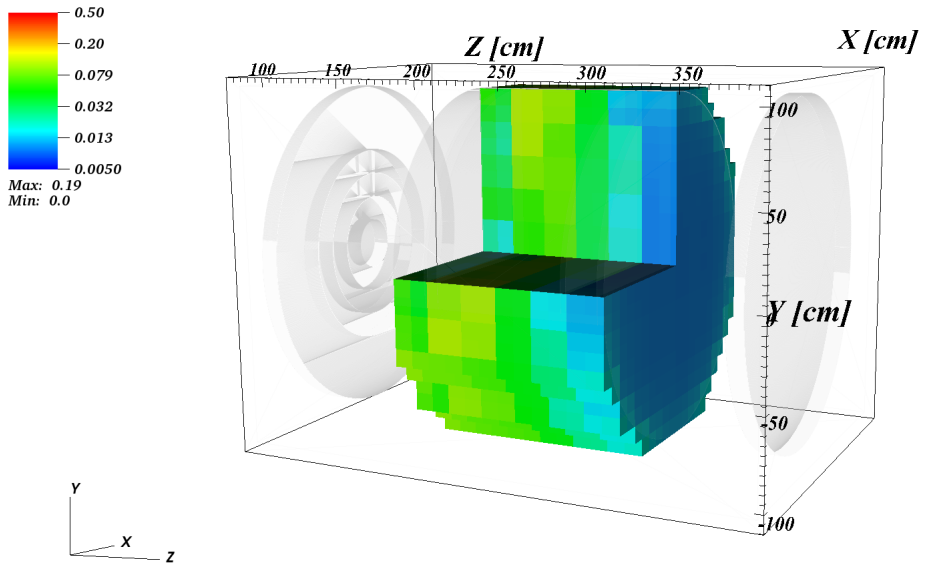

Figure 4.10: Minimum R of the Photon Emission Density for 10^5 s Irradiation and 0 s Decay Times, $20 \times 20 \times 21$ cm^3 / $10 \times 10 \times 10$ cm^3

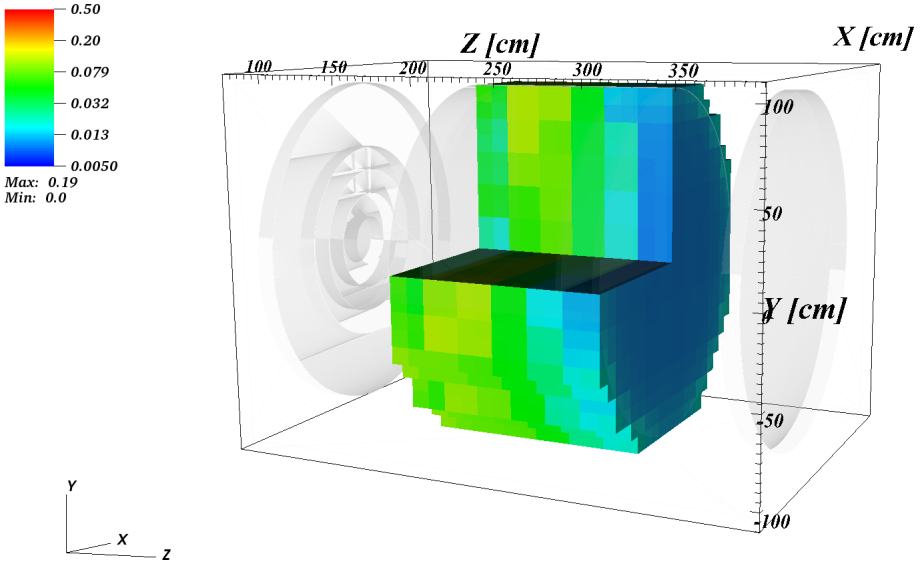

Figure 4.11: R of the Photon Emission Density Obtained Using Correlation Matrices for 10^5 s Irradiation and 0 s Decay Times, $20 \times 20 \times 21$ cm^3 / $10 \times 10 \times 10$ cm^3

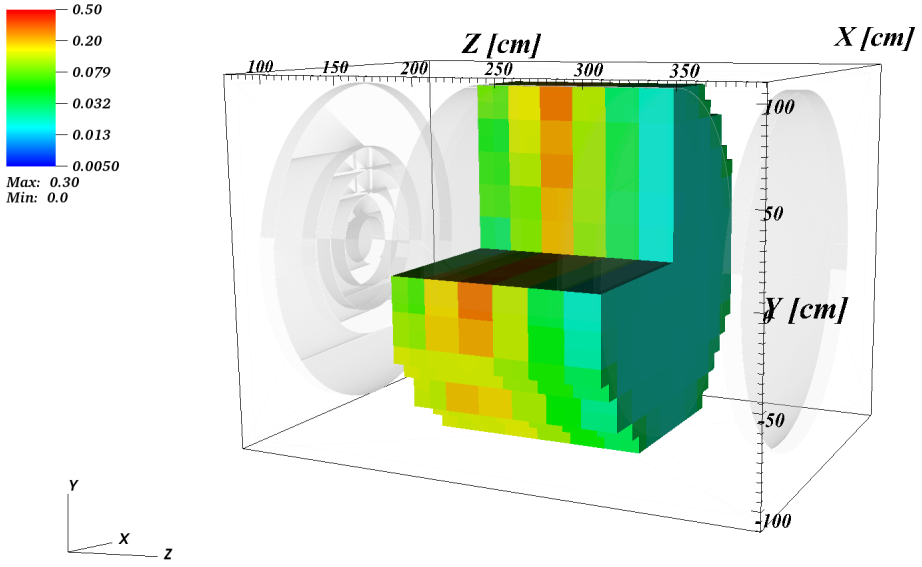

Figure 4.12: Maximum R of the Photon Emission Density for 10^5 s Irradiation and 0 s Decay Times, $20 \times 20 \times 21$ cm^3 / $10 \times 10 \times 10$ cm^3

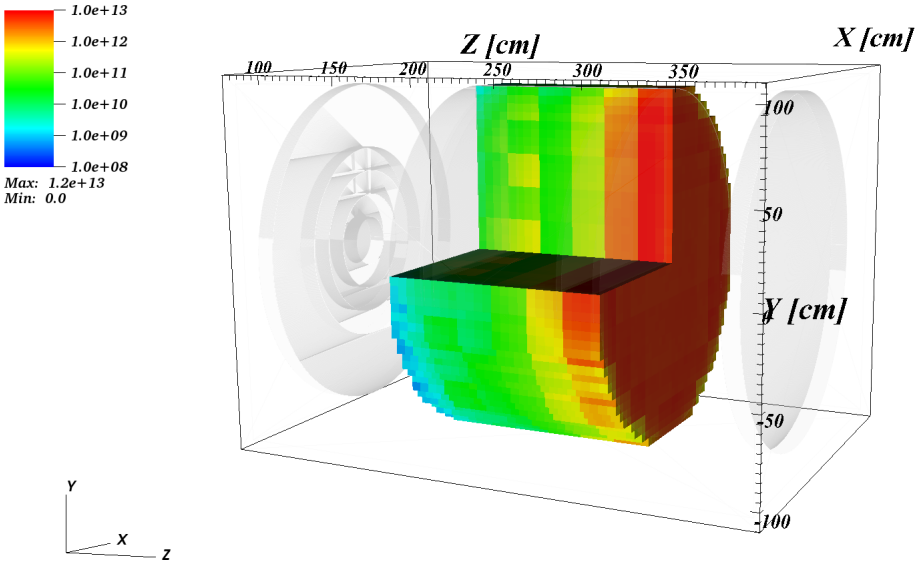

Figure 4.13: Photon Emission Density [p/cm^3 · s] Distribution for 10^5 s Irradiation and 0 s Decay Times, $20 \times 20 \times 21$ cm^3 / $5 \times 5 \times 5$ cm^3

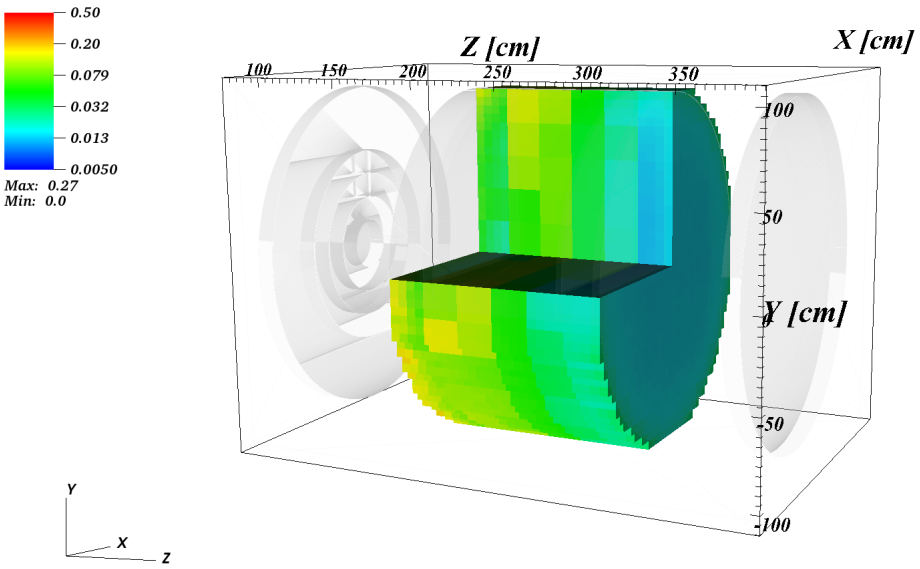

Figure 4.14: R of the Photon Emission Density Obtained Using Correlation Matrices for 10^5 s Irradiation and 0 s Decay Times, $20 \times 20 \times 21$ cm^3 / $5 \times 5 \times 5$ cm^3

4.6 Conclusions

In this chapter, a new version of the R2S workflow that aimed at reducing the number of activation analyses while maintaining high resolution of the photon source has been studied. It has been shown that scaling a photon source obtained using a neutron spectrum over a coarse spatial mesh by the total spectrum over the desired fine spatial mesh alters the photon emission density distribution. This is due to imposing the local spectrum in each coarse spatial mesh on every fine spatial mesh that it constitutes. A test problem has been studied where the effects were prominent in the photon flux but didn't affect the SDR. The reason for that could be related to the relative importance of photons at different energy groups to the SDR, in other words the changes in the photon flux were in groups that are less important to SDR.

Following that, a method to quantify the photon emission density distribution of the scaled photon source in the modified workflow has been introduced. It has been shown that the modified workflow produces source distributions with lower uncertainties compared to the original workflow. This is true only if the neutron spectrum used to obtain the source distribution was over a mesh coarse enough to resolve the flux gradients in the problem. The method has been demonstrated to be effective and simple to apply to quantify the uncertainty of the photon emission density using a demonstration problem.

5 UNCERTAINTY QUANTIFICATION OF THE SHUTDOWN DOSE RATE

5.1 Introduction

In the R2S workflow, the photon emission density distribution obtained from activation analysis, using the neutron flux distribution from the first transport step, is used as a source for the subsequent photon transport step. By obtaining the photon flux distribution in the problem domain, the SDR is then calculated using proper flux-to-dose-rate conversion factors. As the neutron flux distribution in the first transport step is obtained using Monte Carlo (MC) simulations, the produced photon source will have an associated uncertainty, as discussed in chapters 3 and 4. The uncertainty of the SDR reported by MC codes represents only the contribution from the photon transport step to the uncertainty of the SDR and doesn't account for the contribution due to the photon source uncertainty.

It has long been considered that if the neutron flux was obtained with low enough uncertainty, by simulating a large number of histories, that would mean a lower uncertainty of the photon source distribution. The estimate of the uncertainty of the SDR from the photon transport step was then considered as an adequate estimate of the total SDR uncertainty. One of the methods to estimate the total uncertainty from both transport steps which is computationally expensive and might be prohibitive for large models, is the brute force technique. By running many clones of the problem, the whole R2S workflow, with different random number seeds for both transport steps, the standard deviation of the SDR can be obtained. Aside from the obstacle arising from the complexity of the models, the number of clones to obtain adequate estimates of the uncertainty are, on average, large. Many questions arise as a result; how low should the uncertainty of the neutron flux be to guarantee a low enough uncertainty of the photon source to be ignored?, how many clones is enough to obtain an adequate estimate of the uncertainty of the SDR using the brute force method?.

Previous work, [12] [14] [30], provided methodologies to estimate the lower and upper bounds or to calculate the uncertainty of the SDR based on some approximations. While those methods seem adequate for some problems, they often require additional steps which are often cumbersome. In this chapter, a method is introduced to estimate the total uncertainty of the SDR as well as the lower and upper bounds, using the photon source uncertainty, via random sampling.

5.2 Statistical Error Propagation: from the Photon Source to SDR

The SDR at a location, $\vec{r}$, in the problem domain due to a photon source distribution can be expressed as in Eq. (5.1), where $c(\vec{r}, E^p)$ is the contribution from a photon source of unit strength at point $\vec{r}$ and energy E^p, $q(\vec{r}, E^p)$ is the photon source strength, and the superscript p denotes a photon. Discretization of Eq. (5.1) in space and energy is carried out by integrating over the photon energy range of interest and a region of space corresponding to the spatial mesh size. The SDR in mesh voxel/geometry cell could then be expressed as a sum over the contributions of all photon sources from all mesh voxels, v, and energy groups, E^p_h, in the problem domain, as given by Eq. (5.2). The subscript h denotes an energy group number. This is used here to follow the same convention introduced in chapter 3.

$$SDR = \int_v \int_{E^p} c(\vec{r}, E^p) q(\vec{r}, E^p) \, dE^p \, dv \tag{5.1}$$

$$SDR = \sum_v \sum_h c_{v,E^p_h} q_{v,E^p_h} \tag{5.2}$$

The total uncertainty of the SDR due to both the neutron and photon transport steps in the R2S workflow can be defined as in Eq. (5.3).

$$\sigma^2_{SDR,Total} = \sigma^2_{SDR,MC1} + \sigma^2_{SDR,MC2} \tag{5.3}$$

where, $\sigma^2_{SDR,MC1}$ is due to the uncertainty of the photon source distribution, the contribution from the MC neutron transport step (MC1), and $\sigma^2_{SDR,MC2}$ is the contribution of the MC photon transport step (MC2). Since both the neutron and photon transport steps are independent, not performed in the same simulation, the covariance between their contributions to the uncertainty of the SDR is ignored.

There are two possible ways to calculate the contribution to the uncertainty of the SDR due to the uncertainty from the neutron transport step; *explicit* and *implicit*. The *explicit* method could make use of an expression of the SDR as a function of the adjoint neutron source, q^+_{ν,E^n_g}, and the forward neutron flux, ϕ_{ν,E^n_g}, obtained in each mesh voxel. Using the definition of the SDR given by Eq. (5.4), where the subscript g refers to a neutron energy group number, the uncertainty of the SDR could be calculated by applying standard error propagation techniques. This method has two possible drawbacks. The first drawback is that it can only estimate the upper and lower bounds due to the difficulty of estimating the needed neutron flux covariance terms, between combinations of mesh voxels and energy groups. The second comes from relying on an adjoint photon flux to calculate the adjoint neutron source which is usually obtained via deterministic methods and has a built-in uncertainty due to discretization.

$$SDR = \sum_{\nu} \sum_{g} q^+_{\nu,E^n_g} \phi_{\nu,E^n_g} \tag{5.4}$$

The *implicit* method, the subject of this chapter, utilizes random sampling to propagate the uncertainty of the photon source to the SDR. As the SDR is calculated via random sampling in MC simulations, it is possible to tally the uncertainty associated with the contributions from each mesh element to the SDR given the uncertainty of the photon source distribution in the problem domain in those mesh elements. As will be shown, the method requires no modification to the sampling routine in MC codes, only a custom input based on the source distribution is provided for an additional photon transport step. The output of such step is then manipulated to calculate the contribution of the photon source uncertainty to the uncertainty of the SDR. It's worth noting that a code modification to the tally and/or

sampling routine could make it possible to obtain the total uncertainty of the SDR in a single run.

5.2.1 Theory

By applying the standard error propagation technique, via Taylor expansion, to Eq. (5.2), the uncertainty of the SDR can be derived as given by Eq. (5.5), where σ represents statistical uncertainty and ρ represents a correlation coefficient. The covariance between the photon source, q_{v,E_h^p}, and the contribution, c_{v,E_h^p}, for mesh voxel v and photon energy group h is ignored as the two quantities are independent since the uncertainty of the source comes from the neutron transport step.

$$\sigma^2_{SDR,Total} = \sum_{v,v'}\sum_{h,h'}\left(\frac{\partial SDR}{\partial c_{v,E_h^p}}\right)\sigma_{c_{v,E_h^p}}\left(\frac{\partial SDR}{\partial c_{v',E_{h'}^p}}\right)\sigma_{c_{v',E_{h'}^p}}\rho(c_{v,E_h^p}, c_{v',E_{h'}^p}) + \sum_{v,v'}\sum_{h,h'}\left(\frac{\partial SDR}{\partial q_{v,E_h^p}}\right)\sigma_{q_{v,E_h^p}}\left(\frac{\partial SDR}{\partial q_{v',E_{h'}^p}}\right)\sigma_{q_{v',E_{h'}^p}}\rho(q_{v,E_h^p}, q_{v',E_{h'}^p}) \quad (5.5)$$

The first term in Eq. (5.5) represents the contribution to the uncertainty of the SDR due to photon transport reported by MC codes, $\sigma^2_{SDR,MC2}$, while the second term represents the contribution due to the uncertainty of the photon source, $\sigma^2_{SDR,MC1}$. The second term, after some algebraic manipulations, can be expressed as in Eq. (5.6), where $R_{q_{v,E_h^p}}$ is the relative error of q_{v,E_h^p}.

$$\begin{aligned}\sigma^2_{SDR,MC1} &= \sum_{v}\sum_{h} c^2_{v,E_h^p}\sigma^2_{q_{v,E_h^p}} + 2\sum_{\substack{v,v'\\ v<v'}}\sum_{\substack{h,h'\\ h<h'}} c_{v,E_h^p}\sigma_{q_{v,E_h^p}} c_{v',E_{h'}^p}\sigma_{q_{v',E_{h'}^p}}\rho(q_{v,E_h^p}, q_{v',E_{h'}^p}) \\ &= \sum_{v}\sum_{h}(c_{v,E_h^p}q_{v,E_h^p})^2 R^2_{q_{v,E_h^p}} \\ &+ 2\sum_{\substack{v,v'\\ v<v'}}\sum_{\substack{h,h'\\ h<h'}}(c_{v,E_h^p}q_{v,E_h^p})R_{q_{v,E_h^p}}(c_{v',E_{h'}^p}q_{v',E_{h'}^p})R_{q_{v',E_{h'}^p}}\rho(q_{v,E_h^p}, q_{v',E_{h'}^p}) \quad (5.6)\end{aligned}$$

5.2.2 Implementation of the Implicit Method

Using mesh based sampling of the photon source, the normalized photon emission density distribution serves as a probability density function (PDF) which governs the frequency by which particles are sampled at different mesh voxels, v, and energy groups, h. Eq. (5.2) can be written as in Eq. (5.7), where $q_{total} = \sum_v \sum_h q_{v,E_h^p}$ is the total photon emission density, and f_{v,E_h^p} is the relative strength of the photon source, q_{v,E_h^p}, and is also the sampling frequency of a particle from q_{v,E_h^p}. If we considered random sampling from the PDF represented by Eq. (5.7), N samples drawn from the PDF, we can switch from summation over v and h to a summation over i, where i is the sample number. Eq. (5.7) represents how SDR is calculated in the photon transport step in R2S, by tallying the average contribution of all sources in the problem domain to the SDR at the different locations of interest.

$$SDR = q_{total} \sum_v \sum_h c_{v,E_h^p} f_{v,E_h^p} = q_{total} \left(\frac{1}{N} \sum_i c_i \right) \tag{5.7}$$

The same mesh based sampling technique can be utilized to propagate the uncertainty of the photon source to the SDR. This method has an advantage; the photon sources at different mesh voxels, v, and energy groups, h, can be considered as independent, hence avoiding the second term in Eq. (5.6). By analogy to switching from v & h notations to i in writing Eq. (5.7), Eq. (5.6) can be rewritten as given in Eq. (5.8), where $\tilde{R}_{q_{v,E_h^p}}$ is defined as $R_{q_{v,E_h^p}} \sqrt{f_{v,E_h^p}}$.

$$\begin{aligned} \sigma^2_{SDR,MC1} &= q^2_{total} \sum_v \sum_h (c_{v,E_h^p} f_{v,E_h^p})^2 R^2_{q_{v,E_h^p}} \\ &= q^2_{total} \sum_v \sum_h \left(c_{v,E_h^p} R_{q_{v,E_h^p}} \sqrt{f_{v,E_h^p}} \right)^2 f_{v,E_h^p} = q^2_{total} \sum_v \sum_h (c_{v,E_h^p} \tilde{R}_{q_{v,E_h^p}})^2 f_{v,E_h^p} \\ &= q^2_{total} \left(\frac{1}{N} \sum_i (c_i \tilde{R}_i)^2 \right) \end{aligned} \tag{5.8}$$

The contribution of the photon transport step, $\sigma^2_{SDR,MC2}$, to the total uncertainty

of the SDR can be calculated as given in Eq. (5.9), where $R^2_{SDR,MC2}$ is the relative error reported by the MC code.

$$\sigma^2_{SDR,MC2} = R^2_{SDR,MC2} SDR^2 \tag{5.9}$$

A dedicated MC simulation, similar to the photon transport step, to estimate the contribution to the total uncertainty of the SDR due to the photon source uncertainty, $\sigma^2_{SDR,MC1}$, can then be performed by proper adjustment of input. In MC codes, weights can be assigned to the problem domain and is often utilized when a biased PDF is used for sampling to maintain a fair game, the weight is equal to the reciprocal of the biased sampling frequency. In a similar way, if a PDF representing the photon emission density distribution in the problem domain, f_{ν,E^p_h}, is used for sampling, it is possible to modify the tally, $\hat{\mu}$, by assigning weights equal to the modified relative error of the photon source, $\tilde{R}_{q_{\nu,E^p_h}}$. The reported relative error by the MC code, $\sigma^2_{\hat{\mu}}$, Eq. (5.10), can then be manipulated to obtain the uncertainty given by Eq. (5.8). This is demonstrated in Eq. (5.11).

$$\sigma^2_{\hat{\mu}} = R^2_{\hat{\mu}} \hat{\mu}^2 = \frac{q^2_{total}}{N} \left[\frac{1}{N} \sum_i (c_i \tilde{R}_i)^2 - \left(\frac{1}{N} \sum_i (c_i \tilde{R}_i) \right)^2 \right] \tag{5.10}$$

where $\hat{\mu} = q_{total} \frac{1}{N} \sum_i (c_i \tilde{R}_i)$

$$\sigma^2_{SDR,MC1} = q^2_{total} \left(\frac{1}{N} \sum_i (c_i \tilde{R}_i)^2 \right) = \hat{\mu}^2 \left[1 + N R^2_{\hat{\mu}} \right] \tag{5.11}$$

The total uncertainty of the SDR due to both the neutron and photon transport steps can then be calculated as in Eq. (5.12) and the relative error as given by Eq. (5.13). While the second term, $R^2_{SDR,MC2}$, goes down with the number of histories, N, the first term should reach an asymptotic value due to the fact that it's independent of N. By considering the tally, $\hat{\mu}$, its value is expected to be lower by few orders of magnitude compared to the SDR value as a result of the way the tally has been set up. In Eq. (5.8), the tally is the mean of the square of the contributions from each

mesh element, mesh voxel v and energy group h, multiplied by a weight equal to the fractional photon emission of the photon source, $\sqrt{f_{v,E_h^p}}$, and $R_{q_{v,E_h^p}}$ of the mesh element from which the contribution originated. This will result in a tally skewed towards smaller values by few orders of magnitude compared to the value of the SDR. As a result, an acceptable value for $R_{\hat{\mu}}$ would be $\ll 0.1$.

$$\sigma^2_{SDR,Total} = \sigma^2_{SDR,MC1} + \sigma^2_{SDR,MC2} = \hat{\mu}^2 \left[1 + NR^2_{\hat{\mu}}\right] + R^2_{SDR,MC2} SDR^2 \tag{5.12}$$

$$R^2_{SDR,Total} = \left(\frac{\hat{\mu}}{SDR}\right)^2 \left[1 + NR^2_{\hat{\mu}}\right] + R^2_{SDR,MC2} \tag{5.13}$$

5.2.3 Total R Using Random Sampling

To demonstrate the applicability of the method described by Eq. (5.13), a 1-D problem was set up. The problem consists of a discrete PDF with a finite number of bins, from 1 to 1000. The average bin number was then tallied by means of random sampling. This problem was chosen because it is possible to predict the tally and assess the convergence of its relative uncertainty. At the top right corner of Fig. (5.1), a mapping is shown of 10 different PDFs, sampled individually. Starting with uniform at the bottom, to monotonically increasing in the middle, and finally random at the top. Relative errors, R_{bin}, were assigned to all the bins in all PDFs, as shown in the middle plot at the top row on the figure, changing from 0 at the bottom, to monotonically increasing, to monotonically decreasing, and finally random at the top. This is to simulate different situations of a uniform PDF with $R_{bin} = 0$, uniform PDFs with increasing R_{bin}, increasing PDFs with increasing R_{bin}, increasing PDFs with decreasing R_{bin}, and finally random PDFs with randomly assigned R_{bin}. Each plot of the remaining plots corresponds to R of bin number tally starting from the bottom PDF "PDF # 1" to the top PDF "PDF # 10".

In Fig. (5.1), R_2 refers to the relative error of samples drawn randomly from the corresponding PDFs, R_t refers to the total relative error of sampling calculated using Eq. (5.13). R_{ts} represents a special case where R for each sample was also randomly sampled from a Normal distribution, N(0, R_{bin}). It can be seen that in all cases R_2

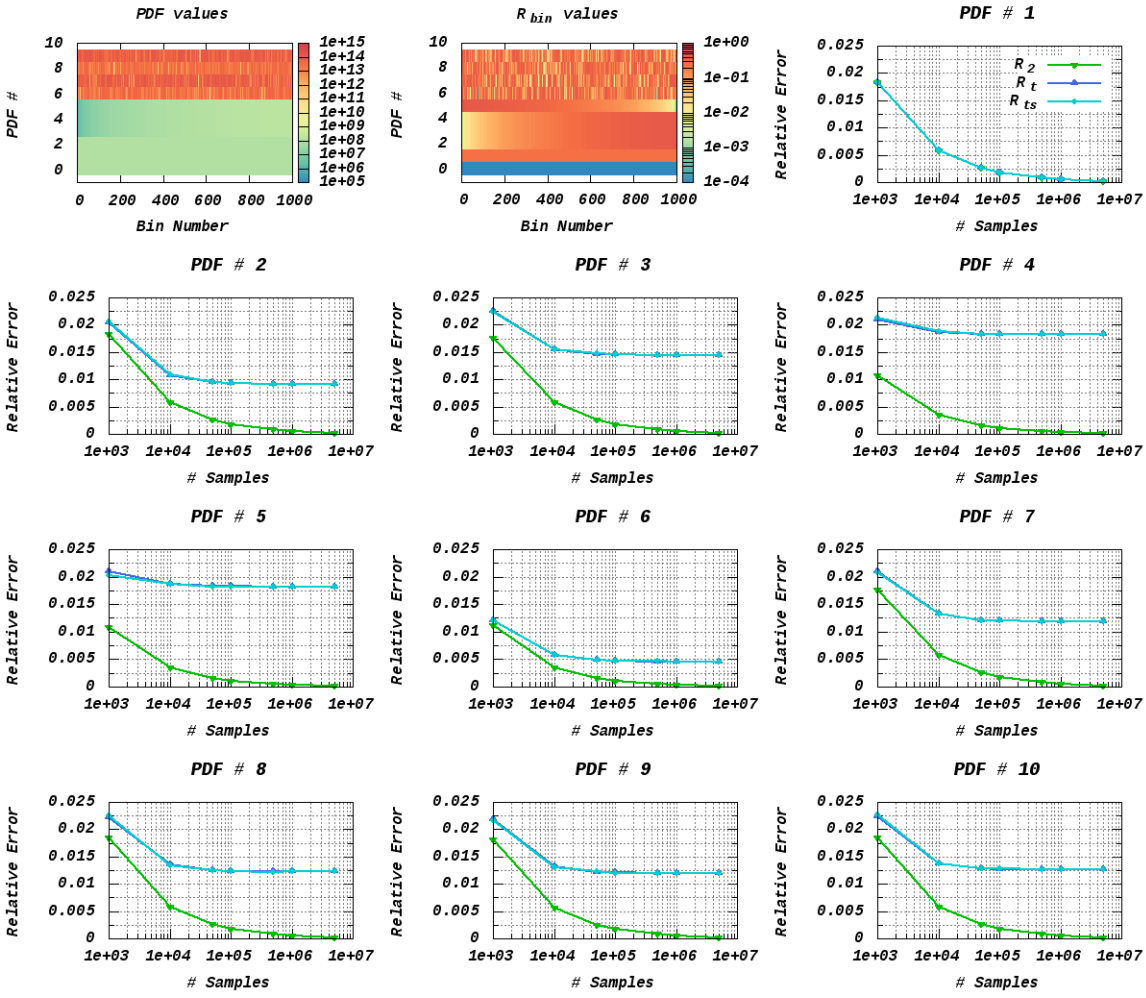

Figure 5.1: Total Relative Error Using Sampling on Different PDFs

diminishes as the number of samples increases, as expected. The total relative error, R_t & R_{ts}, on the other hand levels off at a certain value which is expected also since this is the contribution to the total uncertainty from the uncertainty associated with the PDFs, R_{bin}.

To show the convergence of the method, R_t of the tally was decomposed into two components, one from sampling, R_2, and another from the uncertainty of the PDF values in each bin, R_1, which is calculated using (5.11). This is to be analogous to the case of SDR uncertainty which comes from two separate contributions. Figure (5.2) shows a mapping of the bin number tally for a variation of 10 PDFs similar to those described in the previous two paragraphs with bin numbers increased to 10000. From the figure, it can be seen that R_2, from sampling, decreases with the number of samples drawn, as expected. R_1, which is the component of R_t that comes from R_{bin}, can be seen to level off at certain value, which is the expected behavior since the contribution to the total uncertainty from that of the PDF should remain constant independent of the samples drawn. This demonstrates that with sufficient samples, the contribution of the uncertainty of the sampling PDF to the total uncertainty of the tally can be estimated to a good accuracy.

5.3 Demonstration Problem

For demonstration, the same model used in section 3.6 is used here. First, analyses were performed on the convergence of the statistical uncertainty of the SDR from the photon emission density, $R_{SDR,MC1}$. Following that, the total uncertainty of the SDR using different source distributions were calculated and both $R_{SDR,MC1}$ & $R_{SDR,MC2}$ were examined. Finally, the method of SDR uncertainty quantification by random sampling is demonstrated.

5.3.1 Convergence Of $R_{SDR,MC1}$

As mentioned in previous sections, the contribution of the photon source uncertainty to $R_{SDR,Total}$ should be independent of the number of histories processed

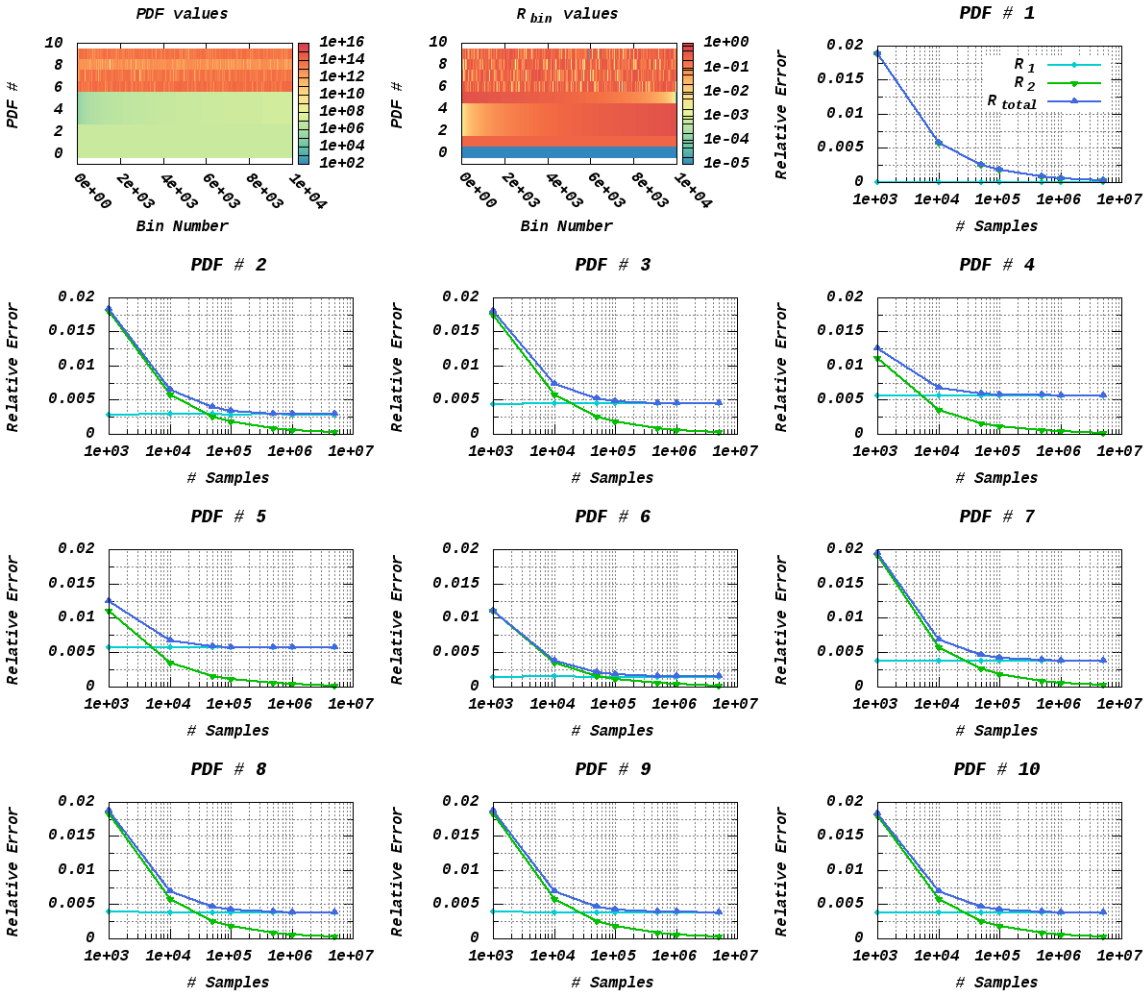

Figure 5.2: Decomposition of Total Relative Error for Sampling on Different PDFs

in the MC dedicated simulation for $R_{SDR,MC1}$ quantification. That means that if enough samples are drawn then the contribution of their uncertainty to $R_{SDR,Total}$ should be stable when using random sampling for uncertainty quantification. This was found to be true before for the toy problem of different PDFs in the previous section. Now this is demonstrated on the FNSF cylindrical problem where $R_{SDR,MC2}$ has been obtained for an irradiation time of 10^5 s and for different decay times with the SDR obtained over a $10 \times 10 \times 10$ cm^3 spatial mesh. Figure (5.3) shows a plot of $R_{SDR,MC1}$ at four points at the mid-plane corresponding to FW, front of BZ, back of BZ, and SR. It can be seen from the figure that $R_{SDR,MC1}$ converges to its asymptotic value after 10^7 histories in MC simulation. It is worth mentioning that the mesh consists of 4800 spatial and 24 energy intervals and with 10^7 histories simulated that means ~ 100 samples were drawn per mesh element. This is key to convergence, enough samples has to be drawn from each mesh element. This supports the findings of the previous section and proves that random sampling can be used to calculate the contribution of the photon source uncertainty to the SDR, $R_{SDR,MC1}$ from Eq. (5.13).

5.3.2 Mesh Sensitivity Study

The described method of utilizing random sampling to propagate the uncertainty of the photon source to the SDR can then be used to study the sensitivity of the SDR and $R_{SDR,Total}$ to mesh size and different workflows, R2S vs modified R2S. Three different photon sources were used to calculate the SDR over a $10 \times 10 \times 10$ cm^3 spatial mesh. The first photon source was obtained using a neutron spectrum over $5 \times 5 \times 5$ cm^3 spatial mesh and the second using a neutron spectrum over $10 \times 10 \times 10$ cm^3 spatial mesh. Both source distributions were obtained for an irradiation time of 10^5 s and at different decay times using the R2S workflow. The third photon source distribution was obtained using the modified R2S workflow, photon source scaling. The photon source distribution was first obtained using a $20 \times 20 \times 21$ cm^3 for an irradiation time of 10^5 s and at different decay times and then scaled by a total neutron flux over a $10 \times 10 \times 10$ cm^3.

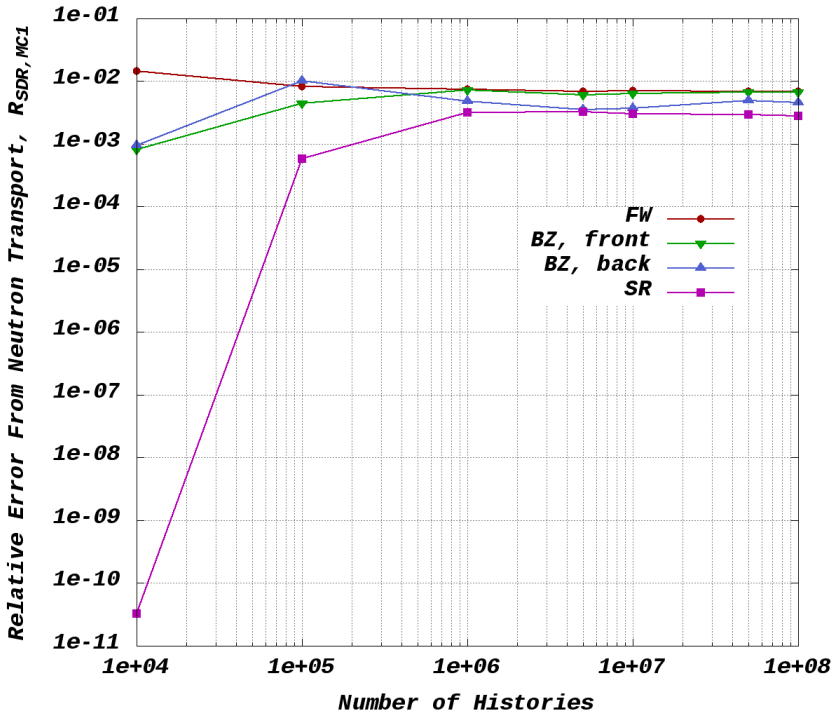

Figure 5.3: Convergence of $R_{SDR,MC1}$ of the SDR at FW, BZ, and SR

The three sources were then used to calculate the SDR and $R_{SDR,Total}$ over the FNSF cylindrical model. For comparison, a different calculation of the SDR and $R_{SDR,Total}$ was also performed using brute force of a photon source obtained using R2S workflow over $10 \times 10 \times 10$ cm^3 mesh. The result of the different clones, 200 with different random number seeds for both transport steps, were then used to calculate the mean and R of the SDR distribution. Figure (5.4) shows plots of the SDR values at different decay times at four points at x = 20 cm, y = -20 cm, and z = 176.5, 208,5, 261,63, 293.83 cm, corresponding to SR, back of BZ, front of BZ, and FW, respectively. From the figure, it can be seen that scaling the photon source results in an overestimation of the SDR especially at higher decay times.

Figure (5.5) shows plots of $R_{SDR,MC2}$ and $R_{SDR,Total}$ of the SDR values shown in Fig. (5.4). By examining both figures, it can be seen that although the $5 \times 5 \times 5$ cm^3 photon source produced slightly lower SDR values at different decay times

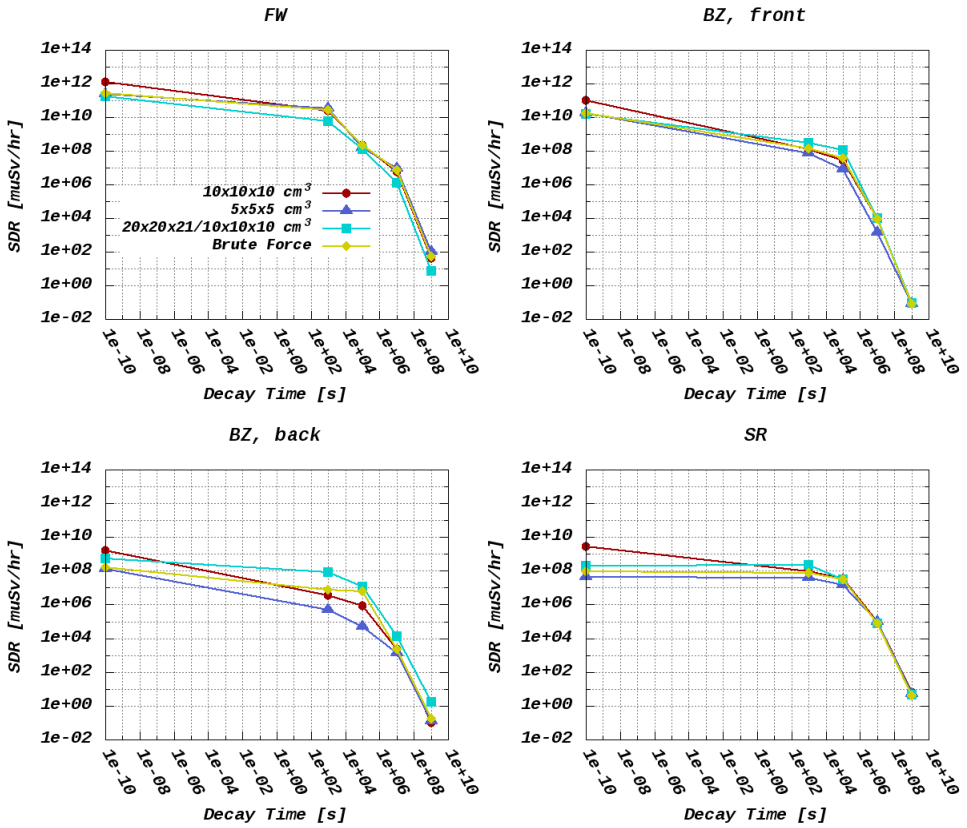

Figure 5.4: SDR [μ Sv/hr] from Photon Sources over Different Mesh Sizes and for 10^5 s Irradiation Time

compared to the $10\times10\times10$ cm^3 photon source, the uncertainty, $R_{SDR,MC1}$, increased at shutdown especially at the back of the BZ. This suggests that the uncertainty of the photon source has to be higher to result in such an increase in $R_{SDR,Total}$. The difference between $R_{SDR,Total}$ and $R_{SDR,MC2}$ is the contribution of the photon source uncertainty, $R_{SDR,MC1}$. While there's no specific trend of that value for the different sources at the different decay times, it was found that at low decay times, at shutdown, on average the photon source over the finer mesh has higher uncertainty associated, Fig. (3.19) vs (3.16), and in turn contributed a higher uncertainty to the $R_{SDR,Total}$.

Attention was paid to the case of $10 \times 10 \times 10$ cm^3 photon source at 10^5 s

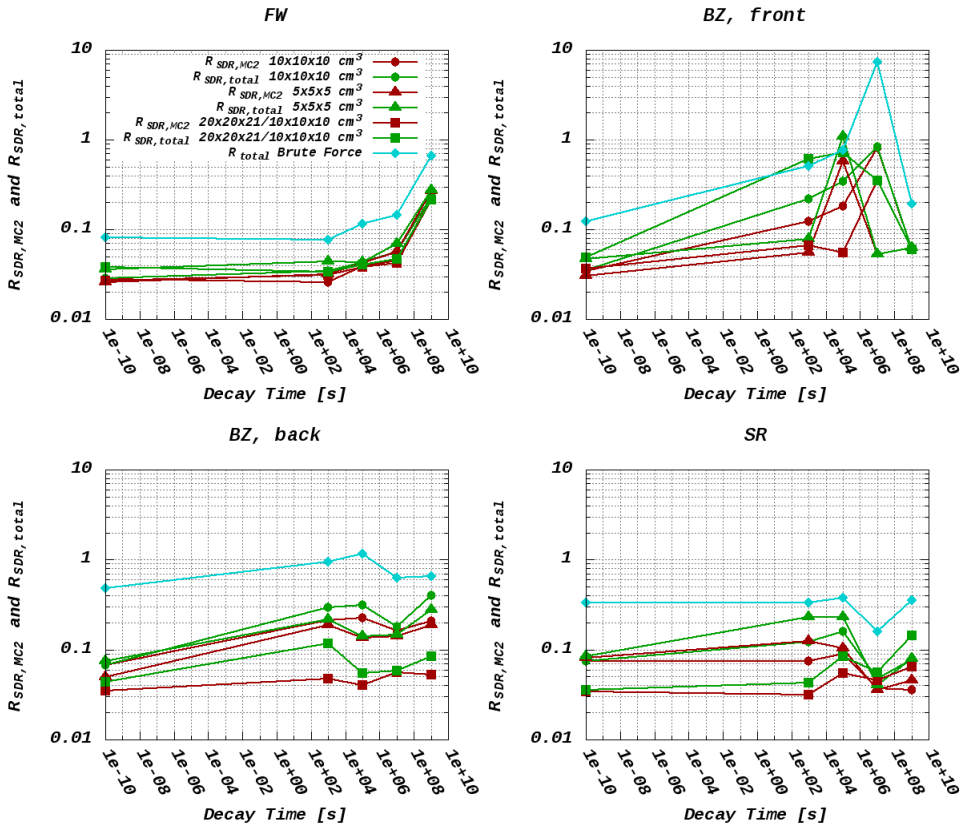

Figure 5.5: $R_{SDR,MC2}$ and $R_{SDR,Total}$ from Photon Sources over Different Mesh Sizes for 10^5 s Irradiation Time

decay time at BZ and SR. It can be seen that although the contribution of the photon transport step to $R_{SDR,Total}$ is low, the contribution from the photon source uncertainty increased compared to the same cases for 0 s decay time. Two causes have been found to be responsible for such an increase. The first is the decrease in the photon emission density compared to the 0 s case, Fig. (5.6). Although the values in the T matrix have decreased, the multi-group neutron flux values and its standard deviations caused the photon emission density to decrease by a higher magnitude compared to 0 s case relative to the decrease in uncertainty, standard deviation, of the source. Figure (5.7) shows a plot of $R_{SDR,MC1}$, $R_{SDR,MC2}$, $R_{SDR,Total}$ and photon source R. The second cause of the increase in $R_{SDR,MC1}$

comes from sampling. The photon emission density in the problem was found to decrease faster in all regions compared to the stabilizing and kink shells. This is due to the decay of other isotopes with shorter half lives compared to tungsten, W-187, that is found in the stabilizing and kink shells which becomes the major contributor to the photon emission density at decay times after shutdown. This means a local increase in the fractional photon emission density at the shells and as a result a higher contribution from that region which has a high uncertainty associated.

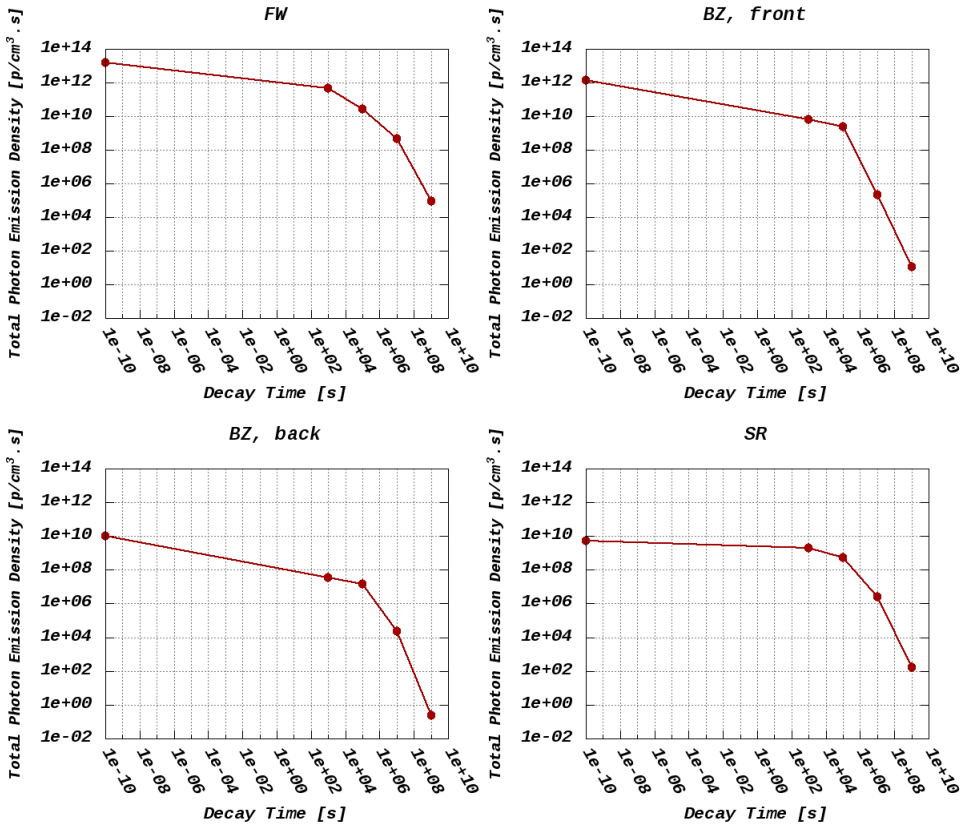

Figure 5.6: Photon Emission Density [p/cm^3 · s] over $10 \times 10 \times 10$ cm^3 Mesh for 10^5 s Irradiation Time

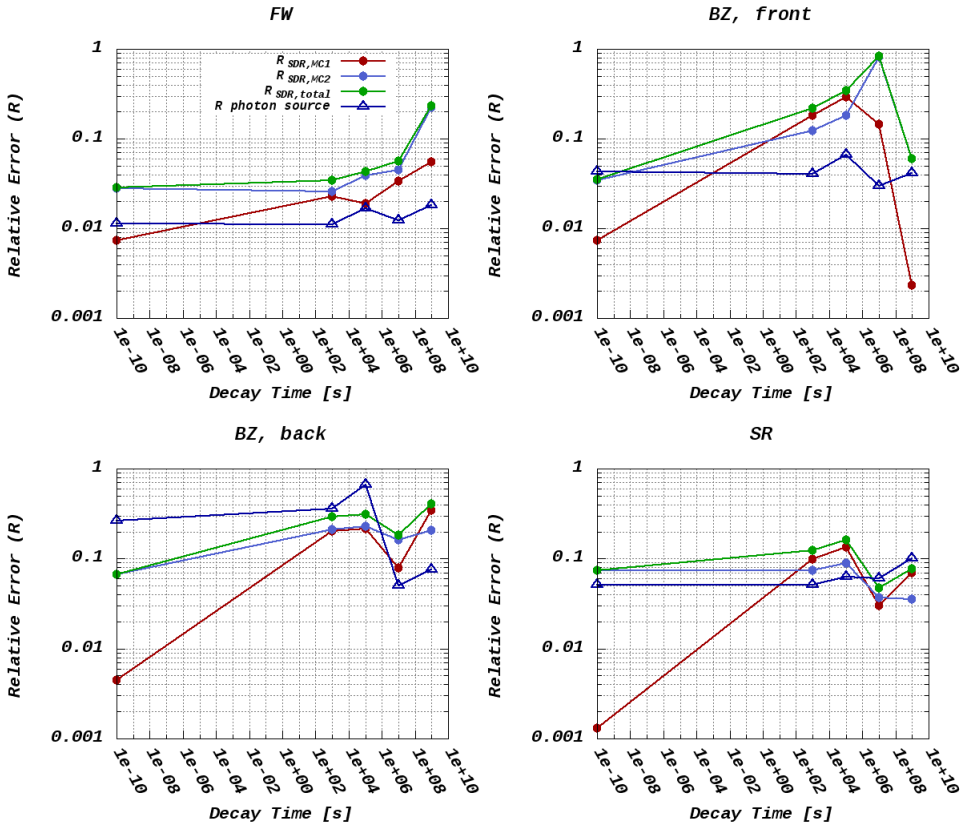

Figure 5.7: $R_{SDR,MC1}$, $R_{SDR,MC2}$, $R_{SDR,Total}$, and Photon Source R From a Photon Source over $10 \times 10 \times 10$ cm^3 Mesh for 10^5 s Irradiation Time

5.3.3 Uncertainty Quantification of the Shutdown Dose Rate

To show the estimated uncertainty of the SDR, $R_{SDR,Total}$, an irradiation time of 10^5 s and a decay time of 0 s have been chosen. The same photon emission density obtained using a neutron spectrum over a $10 \times 10 \times 10$ cm^3 spatial mesh was used, to continue the analyses performed in chapter 3 for the same photon source. Figure (5.8) shows a mapping of the SDR over a $10 \times 10 \times 10$ cm^3 spatial mesh and Fig. (5.9) shows a mapping of the relative error, $R_{SDR,MC2}$. This quantity is the contribution of the photon transport step to $R_{SDR,Total}$. It was mentioned before that such quantity is often considered as being representative of the total uncertainty of the SDR. This has been found not to be the case especially in regions where there is a high photon source with an associated high uncertainty, often in regions far from the neutron source with high photon emission density.

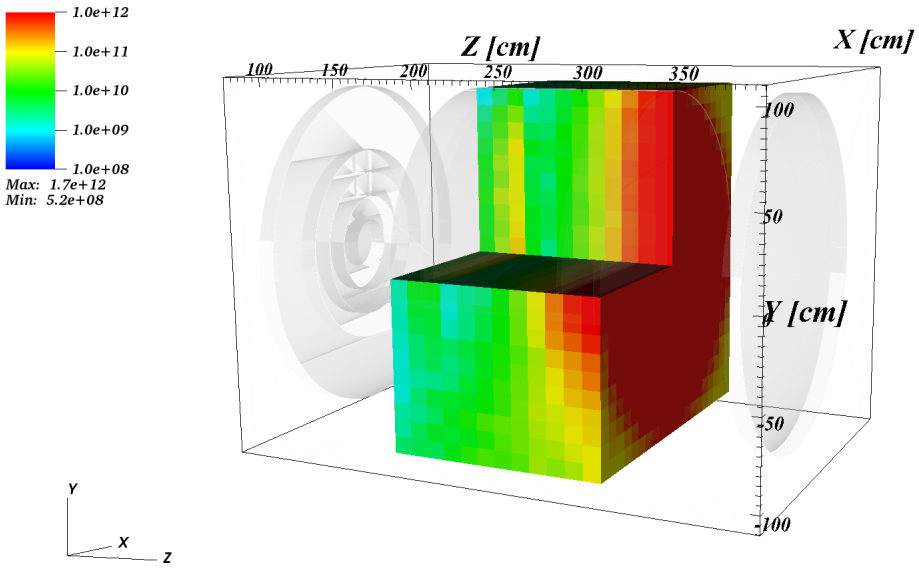

Figure 5.8: SDR [μ Sv/hr], $10 \times 10 \times 10$ cm^3, from a Photon Source, $10 \times 10 \times 10$ cm^3, for 10^5 s Irradiation and 0 s Decay Times

Figure (5.10) shows a mapping of the minimum total R of the SDR, $R^{min}_{SDR,Total}$, which is the value obtained by considering the minimum R of the photon emission density. In Fig. (5.11), the ratio of $R^{min}_{SDR,Total}$ to $R_{SDR,MC2}$ is presented. The mapping

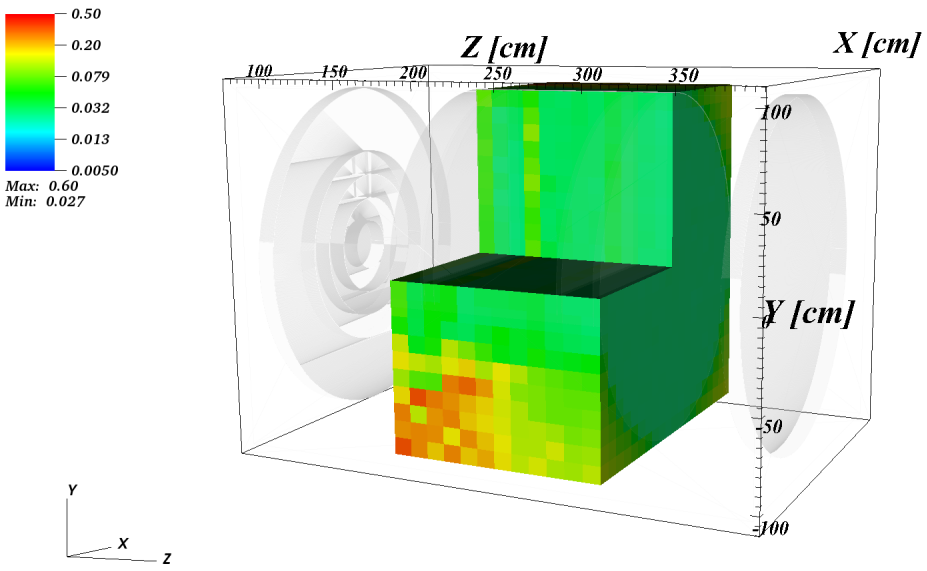

Figure 5.9: $R_{SDR,MC2}$, $10 \times 10 \times 10$ cm^3, from a Photon Source, $10 \times 10 \times 10$ cm^3, for 10^5 s Irradiation and 0 s Decay Times

shows mesh voxels with ratios $> 10\%$ and it can be seen that some mesh voxels exceed a ratio of 50%. This means that taking the R reported by MC codes at the end of the photon transport step, $R_{SDR,MC2}$, as being $R_{SDR,Total}$ will underestimate the SDR uncertainty especially in regions with high photon emission density with a high associated uncertainty. This can be deduced from the figure since the mesh voxels with ratios $> 10\%$ are found near the end of the BZ and the kink shell where the photon emission density is high from tungsten and it has a high associated uncertainty from the neutron fluxes. Figure (5.12) shows the maximum total R of the SDR, $R^{max}_{SDR,Total}$ and the ratio to R from the photon transport step, $R_{SDR,MC2}$, is shown in Fig. (5.13). It's immediately noticeable that the regions where the ratio exceeds 10% are wider than the case in Fig. (5.11). This is due to the increased photon uncertainty compared to the minimum, Fig. (3.17) vs Fig. (3.15).

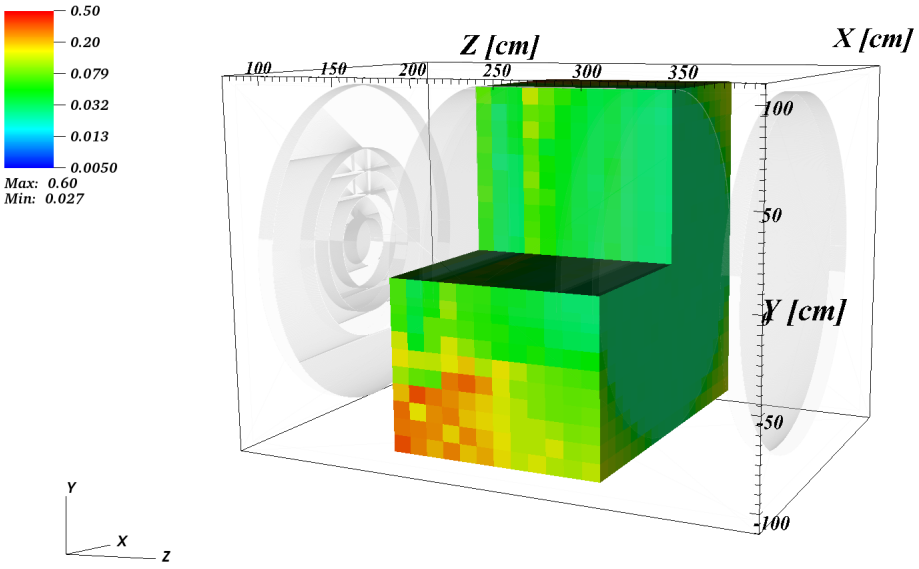

Figure 5.10: $R^{min}_{SDR,Total}$, $10 \times 10 \times 10$ cm^3, from a Photon Source, $10 \times 10 \times 10$ cm^3 for 10^5 s Irradiation and 0 s Decay Times

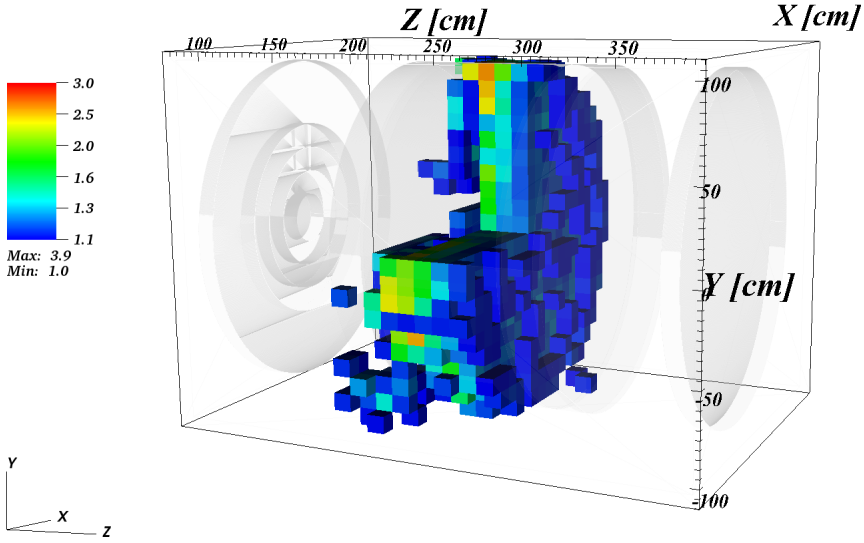

Figure 5.11: Ratio of $R^{min}_{SDR,Total}$ to $R_{SDR,MC2}$, $10 \times 10 \times 10$ cm^3, from a Photon Source, $10 \times 10 \times 10$ cm^3, for 10^5 s Irradiation and 0 s Decay Times

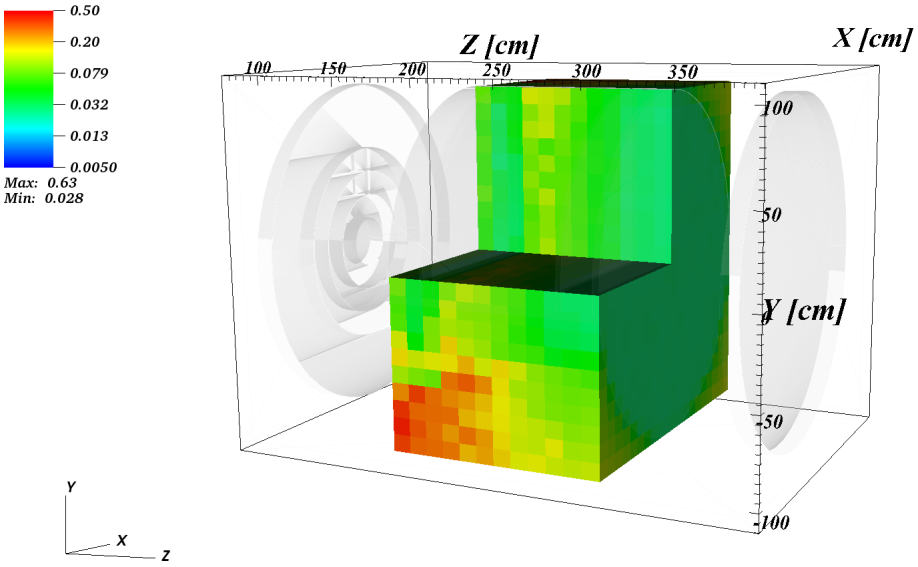

Figure 5.12: $R^{max}_{SDR,Total}$, $10 \times 10 \times 10$ cm^3, from a Photon Source, $10 \times 10 \times 10$ cm^3, for 10^5 s Irradiation and 0 s Decay Times

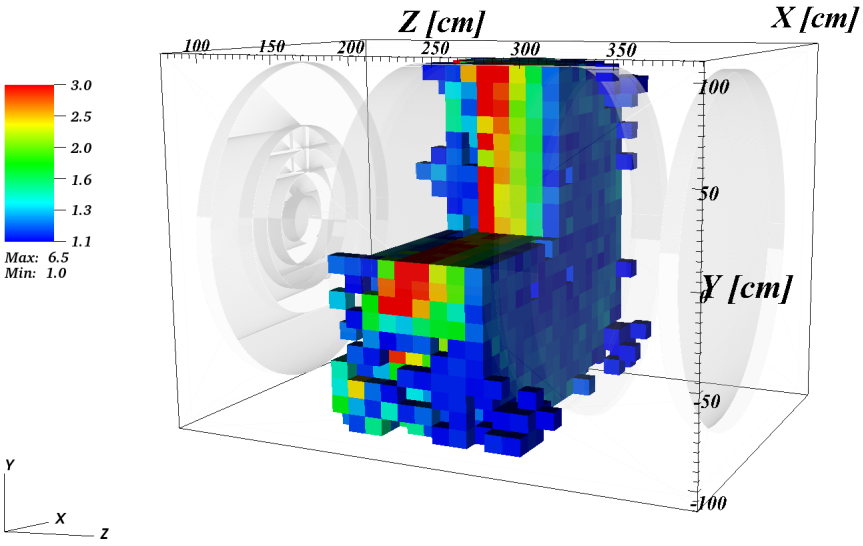

Figure 5.13: Ratio of $R^{max}_{SDR,Total}$ to $R_{SDR,MC2}$, $10 \times 10 \times 10$ cm^3, from a Photon Source, $10 \times 10 \times 10$ cm^3, for 10^5 s Irradiation and 0 s Decay Times

5.4 Conclusions

In this chapter, a method was developed to estimate the contribution of the photon emission density distribution to the total uncertainty of the SDR. The method has been demonstrated on simple toy problems and then applied to the cylindrical FNSF problem. It has been shown that in some regions of the problem domain, taking the uncertainty of the SDR reported by MC codes in the photon transport step, $R_{SDR,MC2}$, as being representative of the total uncertainty, $R_{SDR,Total}$, underestimates the uncertainty of the SDR. This was found to be more important in regions with high photon emission density and a high associated uncertainty which are often found far from the source with material composition that dominates the photon yield compared to surrounding regions.

6 UNCERTAINTY QUANTIFICATION IN A PRODUCTION LEVEL PROBLEM

In chapter 3, the uncertainty of the photon source was calculated by applying standard error propagation techniques to an expression of the photon emission density as a function of the multi-group neutron flux distribution. In chapter 5, a method to calculate the contribution of the photon source uncertainty to the $R_{SDR,Total}$ was introduced. Both methods were applied to a reduced model of the FNSF, a cylindrical geometry with planar boundary source and radial build that corresponds to the OB region of the FNSF. In this chapter, the developed methods are applied to a full scale facility design to show the efficacy of the developed workflow in quantifying the total uncertainty of the SDR in FES. In section 6.1 an introduction to the FNSF facility will be given followed by a description of the facility in section 6.2. In section 6.3 the results of the neutron transport step will be discussed followed by a discussion of the photon source distribution and the calculation of its uncertainty in section 6.4. Sections 6.5 and 6.6 will be dedicated to introducing the SDR results and a discussion of the calculated uncertainty due to neutron and photon transport steps.

6.1 Introduction

The Fusion Energy Systems Studies - Fusion Nuclear Science Facility (FESS-FNSF) [4] is an important step on the US fusion path from test facilities like ITER [3] to a demonstration facility like US DEMO [27]. The FNSF is an experimental facility with the purpose of establishing a database on the behavior of different materials and components in conditions similar to those expected in prospective power plants. The FNSF subjected to study in this chapter is a tokamak-based facility with 518 MW fusion power and consists of 16 sectors - including a 2 cm maintenance clearance in between - with ports and testing modules cutting through it. A top view of the facility with all ports identified is shown in Fig. (6.1) and a planar view of the

CAD model of one sector is shown in Fig. (6.2) with all regions identified. The composition of different OB regions is listed in Table 6.1. The facility was the subject of previous studies [33] [34] that assessed tritium self-sufficiency, shielding of the magnet, and radiation damage.

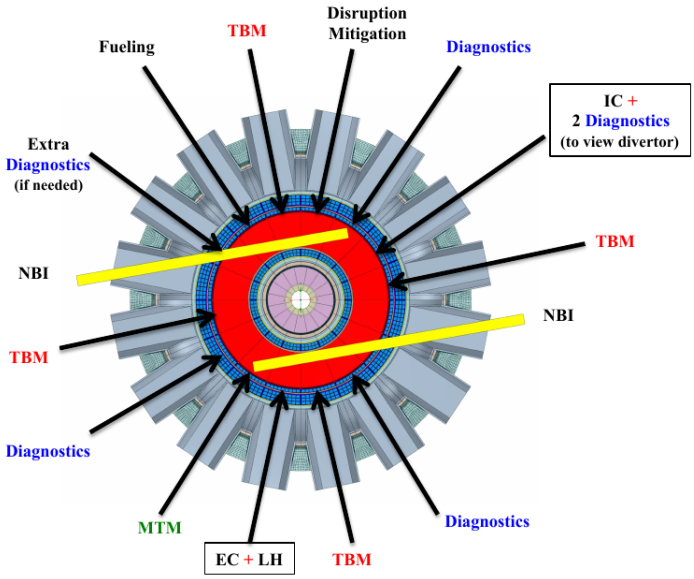

Figure 6.1: Top View of FESS-FNSF Design

A modular facility like the FNSF with integrated engineering systems will necessitate interventional maintenance work to repair/replace different components during the lifetime of the facility. Components near the plasma core will get activated due to exposure to the high energy (~ 14.1 MeV) neutrons produced in the plasma due to deuterium - tritium (D-T) fusion reactions. Such neutrons penetrate deep into system components and cause transmutations of existing nuclides, the products of which are radioactive that decay by emitting photons long after shutdown of the facility. An accurate calculation of the SDR from decay photons is necessary to establish the maintenance schedule and will aide in the design of shielding for activated components outside the core.

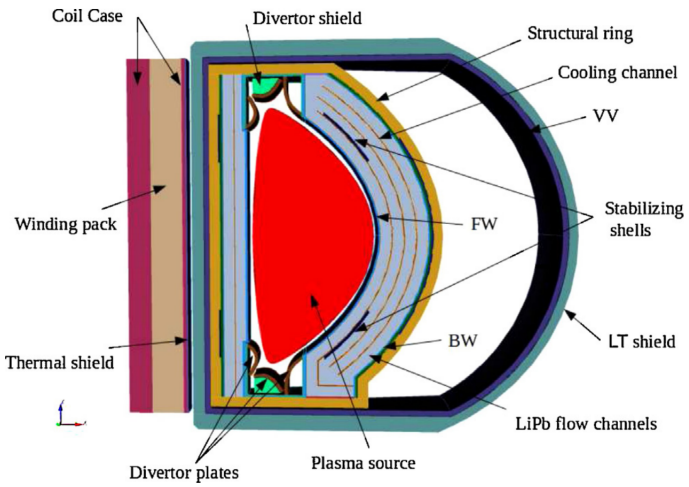

Figure 6.2: CAD Model of a Single FESS-FNSF Sector

Table 6.1: Material Composition of Different OB Regions in FNSF

Region	Material Composition [Volume %]
2 mm W armor	91.3% W, 8.7% void
3.8 cm FW	34% FS (F82H), 66% He
94 cm Breeding Zone	73.7% LiPb (90% Li-6), 14.9% He/void, 7.5% FS, 3.9% SiC
2 cm Back Wall	80% FS, 20% He
2 cm Stabilizing Shells	100% W alloy
6 cm He Manifolds	30% FS, 70% He
20 cm Structural Ring	28% FS, 20% He, 52% B-FS Filler
10 cm VV	60% 3Cr-FS, 40% He
17 cm LT Shield	39% 3Cr-FS, 29% B-FS, 32% H2O
Coil Case	100% SS-316LN
Winding Pack	30% JK2LB Steel, 25% Cu, 25% Ternary Nb3Sn, 10% Hybrid Electric Insulator, 10% Liquid He 30% JK2LB Steel, 25% Cu, 25% Ternary Nb3Sn, 10% Hybrid Electric Insulator, 10% Liquid He

6.2 Problem Description

The design philosophy of a modular facility like the FNSF considers extraction of individual sectors for maintenance away from the core. The proposed scheme [35] involves radial extraction of sectors through maintenance port doors that are extensions to the vacuum vessel (VV) by design. The sector design allows of such

operation since the entire sector is enclosed in a structural ring (SR) that provides support for all subsystems like the divertors, breeding blankets, etc. The approach assumes wait times of a sector in place after shutdown. The LiPb coolant will then be drained and replaced by He to remove residual heat and the sector will be extracted and transported to a hot cell in a transport cask.

The FNSF will go through many operational phases of the plasma (H-He, D-D, D-T, etc.) and the third phase lasts ~ 2.75 years. The facility was the subject of a recent study [36] that assessed the SDR at different maintenance stages. In this chapter, the uncertainty of the SDR at one of this stages is calculated. The uncertainty of the SDR is calculated for a sector inside the core immediately after shutdown following a single pulse of 2.75 years irradiation time. The CAD-based R2S workflow (PyNE-R2S) [37] from the PyNE [38] software library was used with the fusion evaluated nuclear data library (FENDL2.1) [39] and the flux-to-dose-rate conversion factors ICRP-74 [22]. Transport simulations were performed using DAG-MCNP5, a version of MCNP5 [5] that has been enhanced by the DAGMC [7] toolkit which utilizes acceleration techniques to achieve efficient ray tracing directly on CAD solid models. Activation analysis was performed using the activation code ALARA [19].

6.3 Neutron Transport Results

The 16 sectors in FNSF differ only by the type of diagnostics/ports cutting through each one. As diagnostics/ports will have clearance gaps, their main impact would be an increase in the neutron streaming to the back side of the sectors and the shielding plugs at the end of the ports. A previous study [36] found that by analogy to previous tritium breeding analyses [33] [34], the effect of a reduction of the active volume of a sector due to diagnostics/ports on activation is higher than the effect of the increased neutron flux at the back end due to streaming. As a result, this work studies the SDR on a base sector, one without any ports/diagnostics, as it is expected to provide a higher photon emission density.

The model used for neutron transport is a wedge spanning 22.5° as shown in Fig.

(6.3). As mentioned above, the analysis in this chapter considers base sectors and because of symmetry of the 16 sectors in the toroidal direction, reflective BCs were applied on both sides of the model for one sector to simulate neutron transport in the 360° model of the facility. The plasma source was modeled as three concentric tori with varying emission densities; 63%, 32%, 5% from the inner to the outer tori, respectively. The plasma region has a neutron source strength of 1.8372×10^{20} n/s and because of symmetry the source strength considered for the wedge model was 1.1483×10^{19} n/s. For the transport calculation, 10^8 histories in MCNP where simulated.

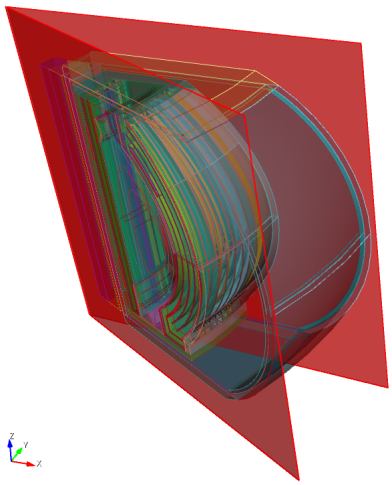

Figure 6.3: CAD Model for Neutron & Photon Transport

Figure (6.4) shows a mapping of the total neutron flux distribution, at plane y = -20 cm, calculated using a Cartesian mesh with $14 \times 14 \times 14$ cm^3 voxels. On the figure, it can be seen that there is a reduction of the flux magnitude of about two orders of magnitude on the outboard and three orders of magnitude on the inboard, between the FW and back of the SR at the mid plane. R of the neutron flux distribution is well below 3% as shown in the mapping of R in Fig. (6.5), at plane y = -20 cm.

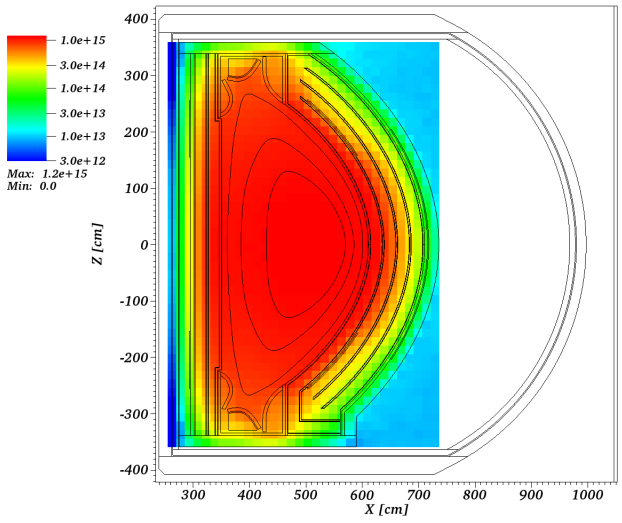

Figure 6.4: Total Neutron Flux Distribution [$n/cm^2 \cdot s$] over a $14 \times 14 \times 14$ cm^3 Mesh

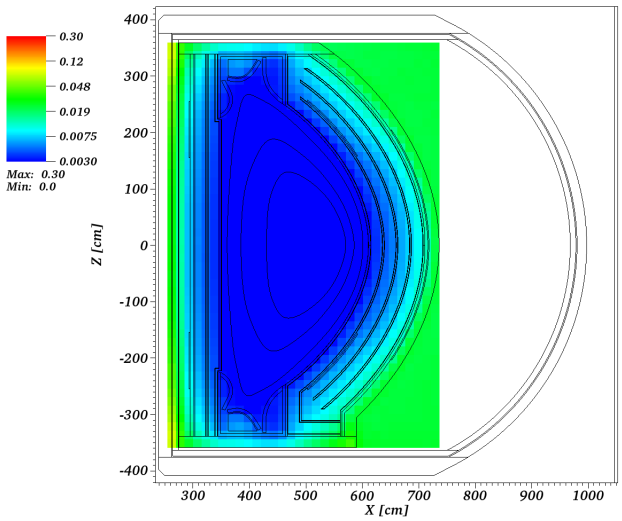

Figure 6.5: R of the Total Neutron Flux Distribution over a $14 \times 14 \times 14$ cm^3 Mesh

6.4 Photon Source Uncertainty Quantification

The obtained neutron flux distribution was then used to calculate the photon emission density distribution. This was achieved by using ALARA code and the R2S workflow. The photon source was obtained at shutdown after an irradiation time of 2.75 years. Figure (6.6) shows a mapping, at plane y = -20 cm, of the photon emission density distribution. The photon emission density can be seen to be relatively higher than surrounding regions at the FW, stabilizing shells, divertor plates, and the kink shell near the end of the sector. This increase is caused by isotopes dominating the photon emission such as; Pb-207m (42.57%), W-187 (29.25%), and W-183m (13.56%) [36].

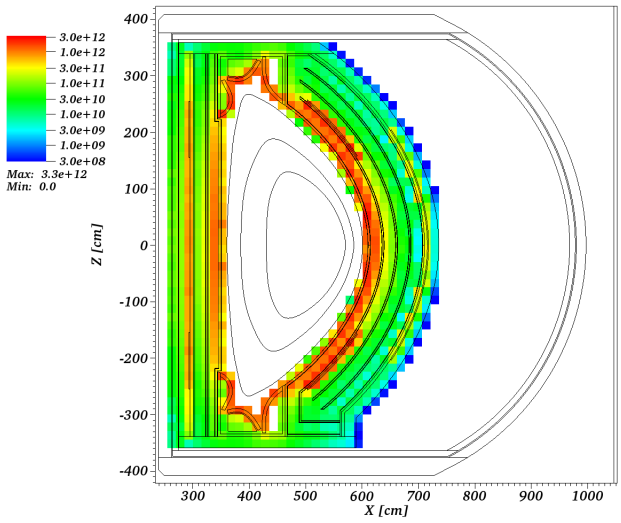

Figure 6.6: Photon Emission Density Distribution [$p/cm^3 \cdot s$] at Shutdown for 2.75 years Irradiation Time

The minimum and maximum R of the photon emission density were then calculated using the method for uncertainty quantification of the photon source introduced in chapter 3. Figures (6.7) & (6.8) show a mapping, at y = -20 cm plane, of the minimum and maximum R of the photon emission density, respectively. It can immediately be noticed that both R_{min} and R_{max} are relatively lower at the FW compared to the other regions of the sector. This is due to two factors. First,

being close to the plasma, the neutron flux distribution has low uncertainty at the plasma facing regions. Second, a high photon emission density from tungsten in the W armor. Also, a higher R_{min} and R_{max} at the kink shell can be noticed. This could be mainly attributed to a higher neutron flux uncertainty as this region is deep inside the sector and away from the plasma with no direct streaming paths.

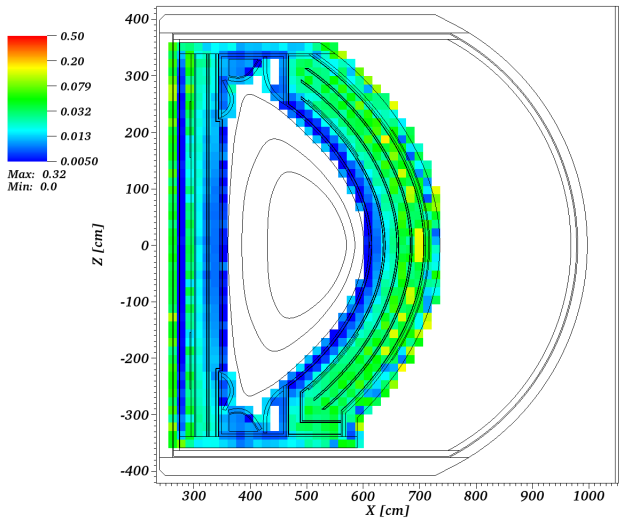

Figure 6.7: R_{min} of the Photon Emission Density Distribution at Shutdown for 2.75 years Irradiation Time

6.5 SDR Results

The photon source distribution obtained was then used as a source definition for the subsequent photon transport step. The SDR was calculated using ICRP-74 flux-to-dose-rate conversion factors. Figure (6.9) shows a mapping, at y = -20 cm plane, of the SDR over the entire sector over a $14 \times 14 \times 14$ cm^3 spatial mesh. As expected, the SDR levels are highest at the core and at the FW. It then goes down by about two orders of magnitude as we move radially from the FW towards the SR. The SDR level is very low behind the VV and LT shield. This was part of the design

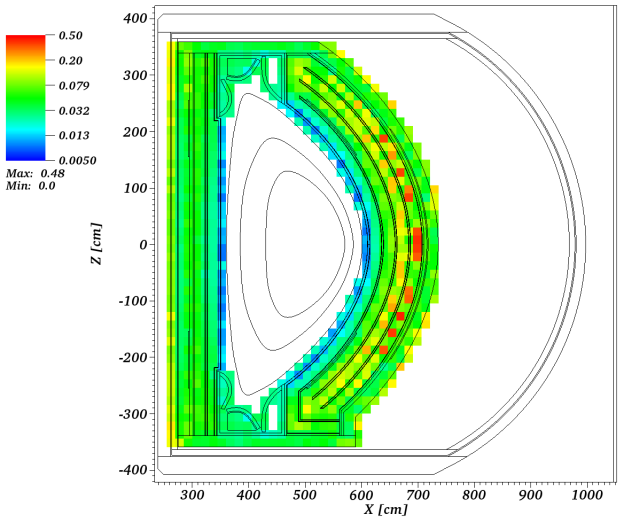

Figure 6.8: R_{max} of the Photon Emission Density Distribution at Shutdown for 2.75 years Irradiation Time

philosophy of FNSF, each layer provides protection to the subsequent layers, so collectively the whole sector provides protection for the magnets behind the VV.

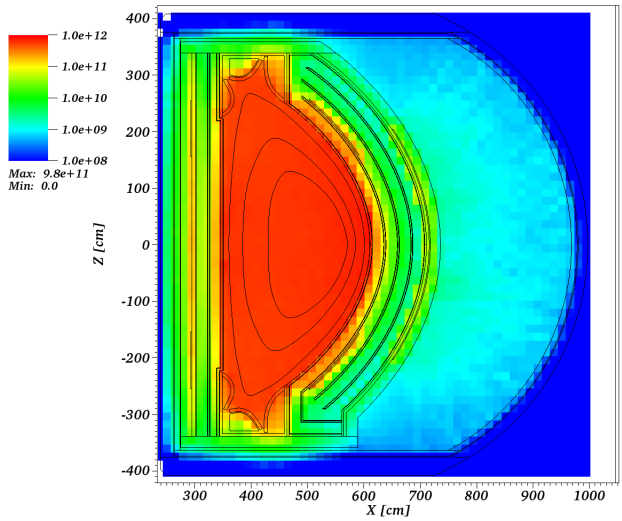

Figure 6.9: SDR [μ Sv/hr] over a $14 \times 14 \times 14$ cm^3 Mesh

The relative error of the SDR from the photon transport step, $R_{SDR,MC2}$ was

reported by the MC transport code, DAG-MCNP5. A mapping, at y = -20 cm plane, of $R_{SDR,MC2}$ is shown in Fig. (6.10). It can be seen that $R_{SDR,MC2}$ is well below 4% inside the sector near the FW and goes up to ~ 10% behind the SR. The lowest $R_{SDR,MC2}$ occurs in the plasma region where there's vacuum and due to facing the highest photon emission density at FW, and the highest is behind the SR. $R_{SDR,MC2}$ is $>$ 25% behind the VV and LT shield where fewer photons are able to traverse the sector where the LiPb region cause attenuation of the flux. This is expected since the shield and VV contain ferritic steel and lead resulting in effective shielding against photons. The high uncertainty of the SDR behind the VV is of no concern in this study since the main focus is on the SDR inside the VV.

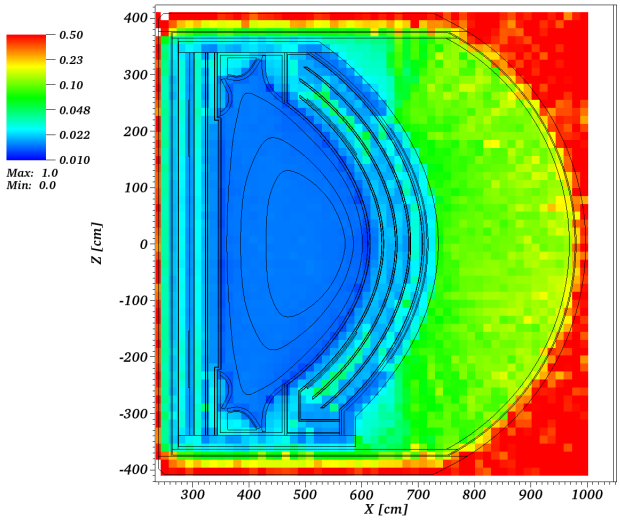

Figure 6.10: Relative Error of the SDR from Photon Transport ($R_{SDR,MC2}$) over a $14 \times 14 \times 14$ cm^3 Mesh

6.6 SDR Uncertainty Quantification

In literature [12], the uncertainty of the SDR from the photon transport step was considered as being representative of the the total uncertainty given that the neutron spectrum used to obtain the photon source had low enough uncertainty. In chapter

5, this has been shown to be missing a component of the total uncertainty. The total uncertainty of the obtained SDR of the sector was estimated by combining both the uncertainty from the photon transport step, $R_{SDR,MC2}$, with the calculated uncertainty from the neutron transport step, $R_{SDR,MC1}$. Since in chapter 4 a method was introduced to quantify the minimum and maximum uncertainty of the photon source, both were combined individually with $R_{SDR,MC2}$ and the bounds of the total SDR uncertainty, $R^{min}_{SDR,Total}$ & $R^{max}_{SDR,Total}$, were calculated. Figure (6.11) shows a mapping, at y = -20 cm plane, of the minimum total uncertainty, $R^{min}_{SDR,Total}$, which was obtained using $R_{SDR,MC2}$ and $R^{min}_{SDR,MC1}$. To show the difference between $R^{min}_{SDR,Total}$ and $R_{SDR,MC2}$, the ratio between the two, $\frac{R^{min}_{SDR,Total}}{R_{SDR,MC2}}$, is shown in Fig. (6.12). The figure shows that in many of the mesh voxels on the OB region $R^{min}_{SDR,MC1}$ amounts to at least ~ 10% of $R_{SDR,MC2}$.

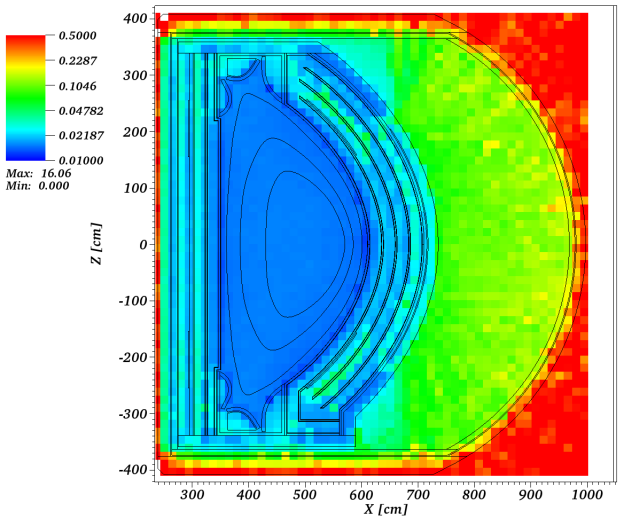

Figure 6.11: $R^{min}_{SDR,Total}$ of the SDR over a $14 \times 14 \times 14$ cm^3 Mesh

In the same way described in the previous paragraph, Fig. (6.13) shows a mapping, at y = -20 cm plane, of the maximum total uncertainty, $R^{max}_{SDR,Total}$, which was obtained using $R_{SDR,MC2}$ and $R^{max}_{SDR,MC1}$. The noticeable increase in $R^{max}_{SDR,Total}$ over $R^{min}_{SDR,Total}$ occurs near the stabilizing shells and in the LiPb cooling channels where the photon source is high. This is to say that the photon emission density

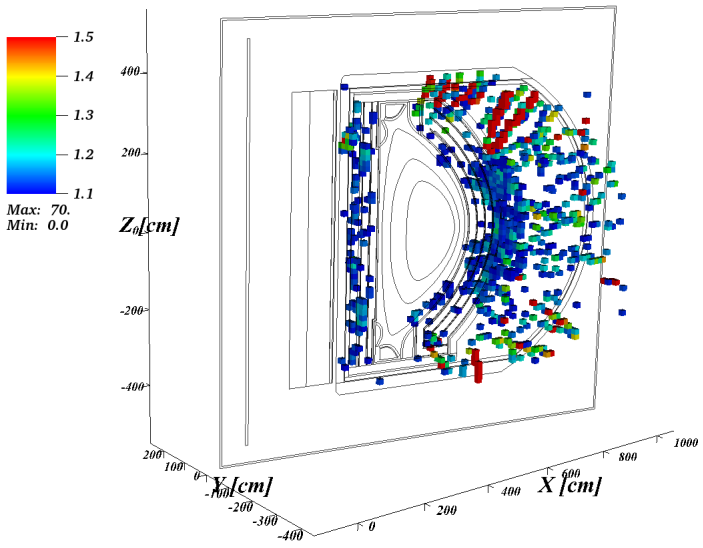

Figure 6.12: Ratio of $R^{min}_{SDR,Total}$ to $R_{SDR,MC2}$ of the SDR over a $14 \times 14 \times 14$ cm^3 Mesh

contributes the most to the uncertainty of the SDR due to the high emission density in those regions that has an associated high uncertainty. This can be shown by consulting Fig. (6.8) where the uncertainty is high in the LiPb cooling channels and at the kink shell near the SR. To show the difference between $R^{max}_{SDR,Total}$ and $R_{SDR,MC2}$, the ratio between the two, $\frac{R^{max}_{SDR,Total}}{R_{SDR,MC2}}$, is shown in Fig. (6.14). The figure shows that in most of the mesh voxels on the OB region $R^{max}_{SDR,MC1}$ amounts to at least $\sim 10\%$ of $R_{SDR,MC2}$. Although that is comparable to the ratio in Fig. (6.12), it can be seen that more voxels are now missing that ratio in case $R_{SDR,MC2}$ was taken to be the total uncertainty of the SDR. Although the total uncertainty is well below the accepted limits, being $< 10\%$, this could be significant in other complex irradiation scenarios or for different material compositions.

Figures (6.15) & (6.16) show a plot of the SDR, $R^{min}_{SDR,Total}$, $R^{max}_{SDR,Total}$, $R_{SDR,MC2}$, $R^{min}_{SDR,MC1}$, and $R^{max}_{SDR,MC1}$ for mesh voxels at $z = 8$ cm along the mid-plane half way between sector side walls. It can be seen that the SDR is high in the LiPb cooling channels compared to the surrounding regions and decreased by many orders of magnitude in regions behind the VV. $R^{min}_{SDR,Total}$ and $R^{max}_{SDR,Total}$ are close

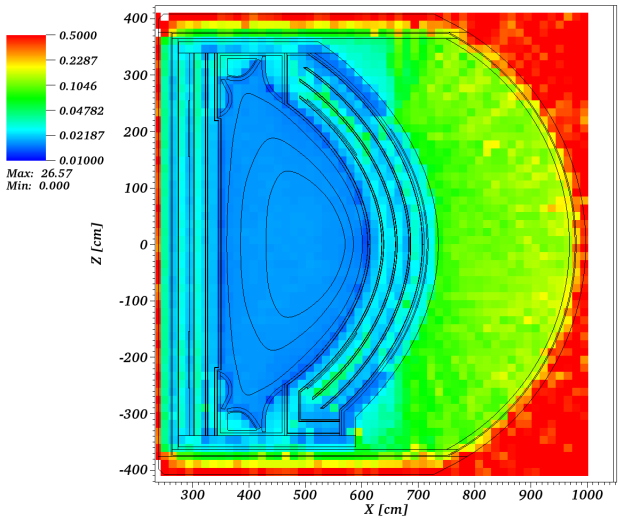

Figure 6.13: $R^{max}_{SDR,Total}$ of the SDR over a $14 \times 14 \times 14$ cm^3 Mesh

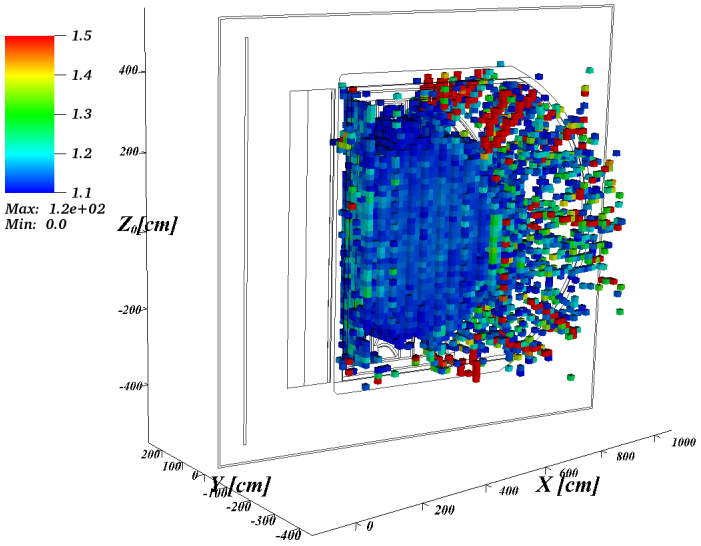

Figure 6.14: Ratio of $R^{max}_{SDR,Total}$ to $R_{SDR,MC2}$ of the SDR over a $14 \times 14 \times 14$ cm^3 Mesh

to $R_{SDR,MC2}$ in nearly all regions along the line of mesh voxels except in the LiPb and plasma regions where there's a noticeable difference due to a high contribution from the uncertainty of the high photon source.

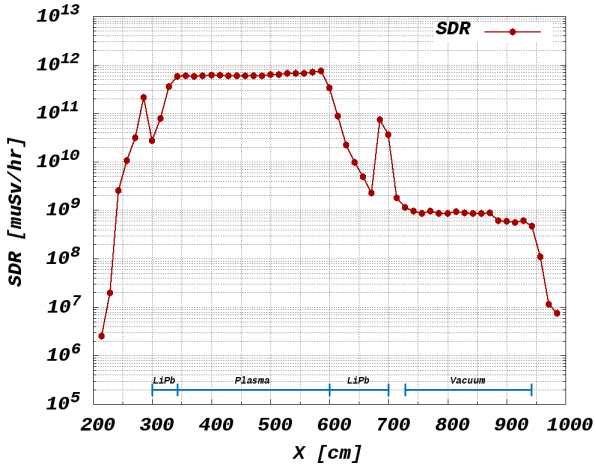

Figure 6.15: SDR [μ Sv/hr] for Mesh Voxels at $z = 8$ cm along Mid-plane over a $14 \times 14 \times 14$ cm^3 Mesh

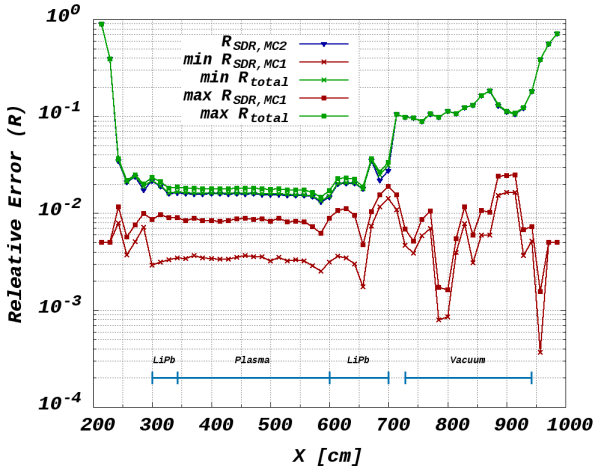

Figure 6.16: $R^{min}_{SDR,Total}$, $R^{max}_{SDR,Total}$, $R_{SDR,MC2}$, $R^{min}_{SDR,MC1}$, and $R^{max}_{SDR,MC1}$ of the SDR for Mesh Voxels at $z = 8$ cm along Mid-plane over a $14 \times 14 \times 14$ cm^3 Mesh

6.7 Conclusions

In this chapter, the method for uncertainty quantification of the photon source and SDR, introduced in chapters 3 & 5, were applied to the FNSF facility. First, neutron transport simulation was performed and the obtained neutron flux distribution was used to produce the photon emission density distribution in the facility. The bounds of R of the photon source were calculated and the photon emission density distribution was used as a source for the photon transport step. The bounds of the total R of the SDR were then calculated. It has been demonstrated that using the value of R reported by MC codes in the photon transport step as being representative of the total R of the SDR results in an underestimation of at least 10 % in some mesh voxels, in the cases studied.

7 CONCLUSIONS AND FUTURE WORK

7.1 Conclusions

In this work, a method to estimate the uncertainty of the photon emission density due to the statistical uncertainty of the neutron flux distribution in the R2S workflow has been developed. Following that, a method to propagate the uncertainty of the photon source to the SDR was also developed. For the uncertainty quantification of the photon source, the developed method has been demonstrated to be efficient in estimating the upper and lower bounds of the uncertainty. An approximation to the covariance between the neutron fluxes in different energy groups has been studied and can be utilized to estimate the uncertainty of the photon emission density. The method has also been applied to a variation of the R2S workflow that utilizes scaling of a photon source obtained over a coarse spatial mesh by the total neutron flux over a fine mesh. The method has also been demonstrated to be useful for mesh sensitivity analysis, which would lead to an optimization of the meshing scheme to minimize the photon source uncertainty. For the uncertainty quantification of the SDR, the new method utilizes random sampling to estimate the contribution of the photon source uncertainty to the total uncertainty of the SDR. Both methods has been demonstrated on simple problems as well as a production-level facility design.

In chapter 3, the standard error propagation formula was applied to an expression of the photon emission density yielding an expression for the uncertainty of the photon emission density that results from the statistical uncertainty of the neutron flux distribution in MC simulations of FES. Analyses have been conducted to study the correlation between the neutron fluxes at different energy groups and it yielded some approximations of the correlation coefficients. The approximations where studied to facilitate the quantification of the uncertainty of the photon emission density. While the derived formula for the photon emission uncertainty can be efficiently used to estimate the upper and lower bounds, analyses were performed to show that the correlation matrices for different elements/mixtures

can be obtained separately and used to estimate the uncertainty over a mesh and that was found to be an acceptable approximation to the correlation coefficients. The approximation of the correlation coefficients builds on the dependence of the correlation coefficients on the nuclear cross section of the material constituents. A best estimate of the correlation coefficients was found to be one where all the neutron energy groups are populated which is often obtained by calculating the correlation coefficients over a simple problem with reflective BCs. The developed method has been demonstrated on a simple cylindrical problem using the neutron spectrum over two different mesh configurations.

In chapter 4, the method developed in Ch. 3 was applied to a new version of the R2S workflow, that aimed at reducing the number of activation calculations while maintaining high resolution of the photon source. It has been shown that scaling a photon source obtained using a neutron spectrum over a coarse spatial mesh by the total neutron flux over the desired fine spatial mesh alters the photon emission density distribution. This is due to imposing the local spectrum in each coarse spatial mesh on every fine spatial mesh that it constitutes. A test problem has been studied where the effects were prominent in the photon flux but didn't affect the SDR. The reason for that could be related to the relative importance of photons at different energy groups to the SDR, in other words the changes in the photon flux were in groups that are less important to SDR. The method has also been utilized for mesh sensitivity analysis. It has been shown that the modified workflow produces source distributions with lower uncertainties compared to the original workflow. This is true only if the neutron spectrum used to obtain the source distribution was over a coarse mesh that is small enough to resolve the flux gradients in the problem. The method has been demonstrated to be effective and simple to apply to quantify the uncertainty of the photon emission density using a demonstration problem.

In chapter 5, a method was developed to estimate the contribution of the uncertainty of the photon emission density distribution to the total uncertainty of the SDR. Random sampling is used to propagate the uncertainty of the photon emission density to the SDR. The approach has been demonstrated on simple non-

transport toy problems consisting of different PDFs with different uncertainties. The behavior of the estimated uncertainty of sampling the position was studied and convergence was confirmed. The method was then applied to a simple cylindrical transport problem. It has been shown that in some regions of the problem domain, taking the uncertainty of the SDR reported by MC codes in the photon transport step, $R_{SDR,MC2}$, as being representative of the total uncertainty, $R_{SDR,Total}$, underestimates the total uncertainty of the SDR. This was found to be more important in regions with high photon emission density and a high associated uncertainty which are often found in regions far from the source with material composition that dominates the photon yield compared to surrounding regions.

In chapter 6, the method for uncertainty quantification of the photon source and SDR, introduced in chapters 3 & 5, were applied to a production-level problem. The model was for the FNSF facility and the irradiation time considered was 2.75 years. First, neutron transport simulation was performed and the obtained neutron flux distribution was used to produce the photon emission density distribution in one sector from the facility. The upper and lower bounds of R of the photon source were calculated and the photon emission density distribution was used as a source for the photon transport step. The upper and lower bounds of $R_{SDR,Total}$ were calculated. It has been demonstrated that using $R_{SDR,MC2}$, reported by MC codes in the photon transport step, as being representative of $R_{SDR,Total}$ resulted in an underestimation of at least 10 % in some mesh voxels, in the case studied.

7.2 Future Work

This work has demonstrated the efficacy of newly developed methods for the quantification of the uncertainty of both the photon emission density and the SDR in the R2S workflow applied to FES. The developed methods provide tools that open the doors for more potential research topics, as will be introduced below.

7.2.1 Mesh Sensitivity and Optimization

As a result of the methods developed in this work it is now possible to study the effect of changing the meshing scheme on the uncertainty of the photon emission density. This could lead to mesh optimization that lowers the photon source uncertainty to acceptable limits. One research topic would be to perform a sweep analysis of the uncertainty of the photon source over a variation of material compositions, such as those typically found in FES applications, and for different irradiation and decay times. This would lead to an optimized meshing scheme that is suitable for each irradiation and decay time to minimize the uncertainty of the photon source.

Another possible research topic would be a comparative study of different meshing schemes and workflows that would potentially lead to an optimization of computing resources for FES simulations. By performing mesh sensitivity analysis it is possible to estimate the optimum meshing scheme that is suitable for different simulation scenarios and problem configurations/settings, potentially avoiding spending too much computing resources on a fine mesh when a coarse mesh could achieve similar results with a reasonable payoff, considering the photon source uncertainty.

7.2.2 Correlation Matrix

The tools provided in this work to study the correlation between the neutron flux in different energy groups give insight to some potential properties of the correlation matrix. A possible research topic would be a thorough analysis of the correlation matrix by applying more advanced statistical tools that could potentially shed more light on the nature of the correlation matrix and its properties. By performing analysis on the correlation matrix for different problem settings (material compositions, BCs, and source type & spectrum) it could lead to analytic expression for the correlation. By expanding the preliminary analysis performed in this work it could become possible to obtain an analytic expression of the correlation between the neutron fluxes in different energy groups as a function of problem settings. Such an expression, although not easy to be developed, would lead to an exact calculation

of uncertainties of the photon sources and the SDR in FES systems.

7.2.3 Error Propagation via Random Sampling

In this work a method was developed to obtain the component of the total uncertainty of the SDR that comes from the photon source uncertainty. Although demonstrated to be efficient enough for the applications that were the subject of this work, there is still room for improvement. One possible improvement would be to modify the tallying and source sampling scheme in MCNP such that both the SDR and its total uncertainty, a component of which is calculated via random sampling on a separate dedicated simulation, could be obtained in a single simulation.

A.1 Correlation Coefficient Decomposition

The correlation coefficient between neutron fluxes at two energy groups is a function of the underlying distribution of histories scores. As a result, more insight on the effect of changes in the problem settings can be gained by decomposing the correlation coefficient. Changes in the problem settings; boundary conditions, nuclear cross-sections, source spectrum, etc. will have a direct impact on the neutron population at different regions of the space-energy phase-space. Assuming we have a reference problem with arbitrary settings and the neutron flux distributions at two different energy groups obtained using MC codes. With the neutron flux, $\hat{x}$, at an energy group defined as the mean of histories scores, x_i, at that energy group, the correlation between the neutron fluxes at two different energy groups is then;

$$\mathrm{Corr}(\hat{x},\hat{y}) = \frac{\mathrm{Cov}(\hat{x},\hat{y})}{\sigma_{\hat{x}}\sigma_{\hat{y}}} = \frac{E[\hat{x}\hat{y}] - E[\hat{x}]E[\hat{y}]}{\sigma_{\hat{x}}\sigma_{\hat{y}}}, \qquad \hat{x} = \frac{1}{N-1}\sum_{i=1}^{N} x_i \tag{A.1}$$

where $\hat{x}$ & $\hat{y}$ are the neutron fluxes at two different energy groups and $\sigma_{\hat{x}}$ & $\sigma_{\hat{y}}$ are their respective standard deviations. $\mathrm{Corr}(\hat{x},\hat{y})$ and $\mathrm{Cov}(\hat{x},\hat{y})$ are the Pearson correlation coefficient and the covariance between $\hat{x}$ & $\hat{y}$, respectively. N is the number of histories in the problem.

Assuming now a change has been introduced in the problem settings, such as a change in the BCs or changes in the materials. Such changes will result in a change in histories scores at different energy groups. The correlation coefficient in A.1 will now be;

$$\mathrm{Corr}(\hat{x}+\delta\hat{x},\hat{y}+\delta\hat{y}) = \frac{\mathrm{Cov}(\hat{x}+\delta\hat{x},\hat{y}+\delta\hat{y})}{\sigma_{\hat{x}+\delta\hat{x}}\sigma_{\hat{y}+\delta\hat{y}}} = \frac{E[(\hat{x}+\delta\hat{x})(\hat{y}+\delta\hat{y})] - E[\hat{x}+\delta\hat{x}]E[\hat{y}+\delta\hat{y}]}{\sigma_{\hat{x}+\delta\hat{x}}\sigma_{\hat{y}+\delta\hat{y}}} \tag{A.2}$$

where $\delta\hat{x}$ & $\delta\hat{y}$ are the means of changes in the histories scores due to changes in

the problem settings. The numerator on the right hand side can be expressed as;

$$\begin{aligned} E[(\hat{x}+\delta\hat{x})(\hat{y}+\delta\hat{y})] - E[\hat{x}+\delta\hat{x}]E[\hat{y}+\delta\hat{y}] &= (E[\hat{x}\hat{y}] - E[\hat{x}]E[\hat{y}]) + (E[\hat{x}\delta\hat{y}] \\ &\quad - E[\hat{x}]E[\delta\hat{y}]) + (E[\delta\hat{x}\hat{y}] - E[\delta\hat{x}]E[\hat{y}]) + (E[\delta\hat{x}\delta\hat{y}] - E[\delta\hat{x}]E[\delta\hat{y}]) \\ &= Cov(\hat{x},\hat{y}) + Cov(\hat{x},\delta\hat{y}) + Cov(\delta\hat{x},\hat{y}) + Cov(\delta\hat{x},\delta\hat{y}) \end{aligned} \quad (A.3)$$

Multiplying and dividing each term on the right hand side by its respective product of standard deviations of the fluxes, we end up with;

$$\begin{aligned} Corr(\hat{x}+\delta\hat{x},\hat{y}+\delta\hat{y}) &= Corr(\hat{x},\hat{y})\frac{\sigma_{\hat{x}}\sigma_{\hat{y}}}{\sigma_{\hat{x}+\delta\hat{x}}\sigma_{\hat{y}+\delta\hat{y}}} + Corr(\hat{x},\delta\hat{y})\frac{\sigma_{\hat{x}}\sigma_{\delta\hat{y}}}{\sigma_{\hat{x}+\delta\hat{x}}\sigma_{\hat{y}+\delta\hat{y}}} \\ &\quad + Corr(\delta\hat{x},\hat{y})\frac{\sigma_{\delta\hat{x}}\sigma_{\hat{y}}}{\sigma_{\hat{x}+\delta\hat{x}}\sigma_{\hat{y}+\delta\hat{y}}} + Corr(\delta\hat{x},\delta\hat{y})\frac{\sigma_{\delta\hat{x}}\sigma_{\delta\hat{y}}}{\sigma_{\hat{x}+\delta\hat{x}}\sigma_{\hat{y}+\delta\hat{y}}} \end{aligned} \quad (A.4)$$

The above relation decomposes the correlation coefficient for the two energy groups into its constituent correlation coefficients. The first term contains $Corr(\hat{x},\hat{y})$ which is the correlation coefficient of the fluxes at the two groups before the change in the problem settings, reference correlation. The second and third terms contain correlation coefficients between the reference fluxes and the changes introduced due to the change in the problem settings. The last term, $Corr(\delta\hat{x},\delta\hat{y})$, contains the correlation coefficient between the changes in the two groups. By examining each term, we can deduce that the terms are just re-normalization of the respective correlation coefficients by the new standard deviations of the fluxes at the two energy groups after the changes in the problem settings were made. It can also be deduced that the first and last terms are more important than the other two as the correlation between the score in one flux in the reference problem and the change in the other group in the changed problem should be low.

In case the flux normalization in the reference and new problem setting are

different, A.4 becomes;

$$\begin{aligned}\mathrm{Corr}(\hat{x}+\delta\hat{x},\hat{y}+\delta\hat{y}) = \mathrm{Corr}(\hat{x},\hat{y})\frac{\sigma_{\hat{x}}\sigma_{\hat{y}}}{\sigma_{\hat{x}+\delta\hat{x}}\sigma_{\hat{y}+\delta\hat{y}}}\frac{M_{new}^2}{M_{ref}^2}+\mathrm{Corr}(\hat{x},\delta\hat{y})\frac{\sigma_{\hat{x}}\sigma_{\delta\hat{y}}}{\sigma_{\hat{x}+\delta\hat{x}}\sigma_{\hat{y}+\delta\hat{y}}}\frac{M_{new}}{M_{ref}}\\ + \mathrm{Corr}(\delta\hat{x},\hat{y})\frac{\sigma_{\delta\hat{x}}\sigma_{\hat{y}}}{\sigma_{\hat{x}+\delta\hat{x}}\sigma_{\hat{y}+\delta\hat{y}}}\frac{M_{new}}{M_{ref}} + \mathrm{Corr}(\delta\hat{x},\delta\hat{y})\frac{\sigma_{\delta\hat{x}}\sigma_{\delta\hat{y}}}{\sigma_{\hat{x}+\delta\hat{x}}\sigma_{\hat{y}+\delta\hat{y}}} \quad \text{(A.5)}\end{aligned}$$

where M_{ref} & M_{new} are the reference and new neutron flux normalizations, respectively.

A.2 Constructed Mesh-Based Fluxes

The neutron flux in MCNP is calculated as the mean of the scores of many histories and should be treated carefully when dividing or multiplying. According to the mean value theorem [8], as the number of histories gets large enough the distribution of the means of histories from repeated independent runs assumes a Normal distribution around the true mean. That concept can be used to judge whether the estimator of the mean for the constructed fluxes is biased or not and derive the corrected formula in case of a biased estimator.

Assume we have three sets of N independent scores; $\{x_1, x_2, ..., x_N\}$, $\{y_1, y_2, ..., y_N\}$, $\{z_1, z_2, ..., z_N\}$ and we need to estimate the quantity

$$\hat{r} = \frac{\hat{x}\hat{y}}{\hat{z}}, \qquad where \qquad \hat{x} = \frac{1}{N}\sum_{i}^{N} x_i \qquad and \qquad \langle\hat{x}\rangle = m_x > 0 \qquad \text{(A.6)}$$

where m_x is the true mean for random variable x and similarly for y and z. Now let $f(\hat{x},\hat{y},\hat{z})$ be a multivariate Normal distribution where $N >> 1$ such that the mean value theorem is applicable. f is itself Normal in the direction of each random variable in accordance with the mean value theorem which is true if each variable mean has a low standard deviation following $N >> 1$. The quantity defined in Eq.

(A.6) can be calculated as:

$$\langle \hat{r} \rangle = \iiint_{-\infty}^{\infty} d\hat{x} d\hat{y} d\hat{z} \hat{r} f(\hat{x}, \hat{y}, \hat{z}) = \iiint_{-\infty}^{\infty} d\hat{x} d\hat{y} d\hat{z} \frac{\hat{x}\hat{y}}{\hat{z}} f(\hat{x}, \hat{y}, \hat{z}) \tag{A.7}$$

$\hat{x}$ can be written as $\hat{x} = m_x[\frac{\hat{x}-m_x}{m_x} + 1]$ and similarly for $\hat{y}$ and $\hat{z}$. Eq. (A.7) becomes

$$\langle \hat{r} \rangle = \frac{m_x m_y}{m_z} \iiint_{-\infty}^{\infty} d\hat{x} d\hat{y} d\hat{z} \frac{[\frac{\hat{x}-m_x}{m_x} + 1][\frac{\hat{y}-m_y}{m_y} + 1]}{[\frac{\hat{z}-m_z}{m_z} + 1]} f(\hat{x}, \hat{y}, \hat{z}) \tag{A.8}$$

Because N $>>$ 1, so $|\frac{\hat{z}-m_z}{m_z}| << 1$. Expressing the denominator using the binomial theorem with a real variable and truncating at the second order term we end up with

$$\langle \hat{r} \rangle = \frac{m_x m_y}{m_z} \iiint_{-\infty}^{\infty} d\hat{x} d\hat{y} d\hat{z} \left[\frac{\hat{x} - m_x}{m_x} + 1\right] \left[\frac{\hat{y} - m_y}{m_y} + 1\right] \cdot \left[1 - \left(\frac{\hat{z} - m_z}{m_z}\right) + \left(\frac{\hat{z} - m_z}{m_z}\right)^2\right] f(\hat{x}, \hat{y}, \hat{z}) \tag{A.9}$$

which evaluates to

$$\langle \hat{r} \rangle = \frac{m_x m_y}{m_z} \left[1 + \frac{V_{\hat{x},\hat{y}}}{m_x m_y} - \frac{V_{\hat{y},\hat{z}}}{m_y m_z} - \frac{V_{\hat{x},\hat{z}}}{m_x m_z} + \frac{V_{\hat{z}}^2}{{m_z}^2}\right] \tag{A.10}$$

where $V_{\hat{x},\hat{z}}$ is the covariance between $\hat{x}$ and $\hat{z}$ and $V_{\hat{z}}^2$ is the variance of variable $\hat{z}$. It is clear that the estimator of the product given in Eq. (A.6) is biased and a correction should be applied. The unbiased estimator can be written as

$$\hat{r}_{unbiased} = \frac{\hat{x}\hat{y}}{\hat{z}} \left[1 - \frac{Cov_{\hat{x},\hat{y}}}{\hat{x}\hat{y}} + \frac{Cov_{\hat{y},\hat{z}}}{\hat{y}\hat{z}} + \frac{Cov_{\hat{x},\hat{z}}}{\hat{x}\hat{z}} - \frac{Var_{\hat{z}}}{\hat{z}^2}\right] \tag{A.11}$$

A similar procedure could be followed for the variance of $\hat{r}$ and the unbiased

variance is given by

$$Var_{\hat{r}_{unbiased}} = \left(\frac{\hat{x}\hat{y}}{\hat{z}}\right)^2 \left[\frac{Var_{\hat{x}}}{\hat{x}^2} + \frac{Var_{\hat{y}}}{\hat{y}^2} + \frac{Var_{\hat{z}}}{\hat{z}^2} + 2\frac{Cov_{\hat{x},\hat{y}}}{\hat{x}\hat{y}} - 2\frac{Cov_{\hat{y},\hat{z}}}{\hat{y}\hat{z}} - 2\frac{Cov_{\hat{x},\hat{z}}}{\hat{x}\hat{z}}\right] \quad (A.12)$$

which also shows the covariance terms are necessary for a correct derivation of variance of $\hat{r}$ based on the variances of $\hat{x}, \hat{y}$, and $\hat{z}$.

A.3 The Statistical Error of the Ratio of Two Random Variables

In a similar way to the derivation in appendix A.2, the unbiased estimator and the corrected statistical uncertainty of the ratio of two random variables could be derived. Assume we have two sets of N independent scores; $\{x_1, x_2, ..., x_N\}$, $\{z_1, z_2, ..., z_N\}$ and we need to estimate the quantity

$$\hat{r} = \frac{\hat{x}}{\hat{z}}, \qquad where \qquad \hat{x} = \frac{1}{N}\sum_{i}^{N} x_i \qquad and \qquad \langle\hat{x}\rangle = m_x > 0 \quad (A.13)$$

where m_x is the true mean for random variable x and similarly for z. Now let $f(\hat{x}, \hat{z})$ be a bi-variate Normal distribution where $N >> 1$ such that the mean value theorem is applicable. f is itself Normal in the direction of each random variable in accordance with the mean value theorem which is true if each variable mean has a low standard deviation following $N >> 1$. The quantity defined in Eq. (A.13) can be calculated as:

$$\langle\hat{r}\rangle = \iint_{-\infty}^{\infty} d\hat{x}d\hat{z}\hat{r}f(\hat{x},\hat{z}) = \iint_{-\infty}^{\infty} d\hat{x}d\hat{z}\frac{\hat{x}}{\hat{z}}f(\hat{x},\hat{z}) \quad (A.14)$$

$\hat{x}$ can be written as $\hat{x} = m_x[\frac{\hat{x}-m_x}{m_x} + 1]$ and similarly for $\hat{z}$. Eq. (A.14) becomes

$$\langle \hat{r} \rangle = \frac{m_x}{m_z} \iint_{-\infty}^{\infty} d\hat{x}d\hat{z} \frac{[\frac{\hat{x}-m_x}{m_x} + 1]}{[\frac{\hat{z}-m_z}{m_z} + 1]} f(\hat{x}, \hat{z}) \tag{A.15}$$

Because N >> 1, so $|\frac{\hat{z}-m_z}{m_z}| << 1$. Expressing the denominator using the binomial theorem with a real variable and truncating at the second order term we end up with

$$\langle \hat{r} \rangle = \frac{m_x}{m_z} \iint_{-\infty}^{\infty} d\hat{x}d\hat{z} \left[\frac{\hat{x} - m_x}{m_x} + 1\right] \left[1 - \left(\frac{\hat{z} - m_z}{m_z}\right) + \left(\frac{\hat{z} - m_z}{m_z}\right)^2\right] f(\hat{x}, \hat{z}) \tag{A.16}$$

which evaluates to

$$\langle \hat{r} \rangle = \frac{m_x}{m_z} \left[1 - \frac{V_{\hat{x},\hat{z}}}{m_x m_z} + \frac{V_{\hat{z}}^2}{{m_z}^2}\right] \tag{A.17}$$

where $V_{\hat{x},\hat{z}}$ is the covariance between $\hat{x}$ and $\hat{z}$ and $V_{\hat{z}}^2$ is the variance of variable $\hat{z}$. It is clear that the estimator of the quotient given in Eq. (A.13) is biased and a correction should be applied. The unbiased estimator can be written as

$$\hat{r}_{unbiased} = \frac{\hat{x}}{\hat{z}} \left[1 + \frac{Cov_{\hat{x},\hat{z}}}{\hat{x}\hat{z}} - \frac{Var_{\hat{z}}}{\hat{z}^2}\right] \tag{A.18}$$

A similar procedure could be followed for the variance of $\hat{r}$ and the unbiased variance is given by

$$Var_{\hat{r}_{unbiased}} = \left(\frac{\hat{x}}{\hat{z}}\right)^2 \left[\frac{Var_{\hat{x}}}{\hat{x}^2} + \frac{Var_{\hat{z}}}{\hat{z}^2} - 2\frac{Cov_{\hat{x},\hat{z}}}{\hat{x}\hat{z}}\right] \tag{A.19}$$

which also shows the covariance terms are necessary for a correct derivation of variance of $\hat{r}$ based on the variances of $\hat{x}$ and $\hat{z}$.

A.4 Derivation of the Condition Under Which Correction Terms Could Be Ignored in the Constructed Flux Formula

Using the results of the derivation from appendix A.2 (Eqs. (A.11) & (A.12)), an expression for the corrected formula of constructed flux and its relative error is given by Eqs. (A.20a) & (A.20b), respectively.

$$\phi(r_f, E_f^n) = \frac{\phi(r_f, E_c^n)\phi(r_c, E_f^n)}{\phi(r_c, E_c^n)} \left[1 - R^2(r_c, E_c^n) - \frac{Cov[\phi(r_f, E_c^n), \phi(r_c, E_f^n)]}{\phi(r_f, E_c^n)\phi(r_c, E_f^n)} + \frac{Cov[\phi(r_f, E_c^n), \phi(r_c, E_c^n)]}{\phi(r_f, E_c^n)\phi(r_c, E_c^n)} + \frac{Cov[\phi(r_c, E_f^n), \phi(r_c, E_c^n)]}{\phi(r_c, E_f^n)\phi(r_c, E_c^n)} + O(3)\right] \quad \text{(A.20a)}$$

$$R^2(r_f, E_f^n) = \left[R^2(r_f, E_c^n) + R^2(r_c, E_f^n) + R^2(r_c, E_c^n) + 2\frac{Cov[\phi(r_f, E_c^n), \phi(r_c, E_f^n)]}{\phi(r_f, E_c^n)\phi(r_c, E_f^n)} - 2\frac{Cov[\phi(r_f, E_c^n), \phi(r_c, E_c^n)]}{\phi(r_f, E_c^n)\phi(r_c, E_c^n)} - 2\frac{Cov[\phi(r_c, E_f^n), \phi(r_c, E_c^n)]}{\phi(r_c, E_f^n)\phi(r_c, E_c^n)} + O(3)\right] \quad \text{(A.20b)}$$

where $R(r_c, E_c^n)$ is a relative error for $\phi(r_c, E_c^n)$ and is defined as in Eq. (A.21) and $\sigma_{\phi(r_c, E_c^n)}$ is the standard deviation of $\phi(r_c, E_c^n)$.

$$R(r_c, E_c^n) = \frac{\sigma_{\phi(r_c, E_c^n)}}{\phi(r_c, E_c^n)} \quad \text{(A.21)}$$

From Eq. (A.20a) we have,

$$1 - R^2(r_c, E_c^n) - \frac{Cov[\phi(r_f, E_c^n), \phi(r_c, E_f^n)]}{\phi(r_f, E_c^n)\phi(r_c, E_f^n)} + \frac{Cov[\phi(r_f, E_c^n), \phi(r_c, E_c^n)]}{\phi(r_f, E_c^n)\phi(r_c, E_c^n)} + \frac{Cov[\phi(r_c, E_f^n), \phi(r_c, E_c^n)]}{\phi(r_c, E_f^n)\phi(r_c, E_c^n)} + O(3) > 0 \quad \text{(A.22)}$$

and the correction terms - all terms other than 1 - can be ignored only if the following

condition is satisfied,

$$R^2(r_c, E_c^n) + \frac{Cov[\phi(r_f, E_c^n), \phi(r_c, E_f^n)]}{\phi(r_f, E_c^n)\phi(r_c, E_f^n)} - \frac{Cov[\phi(r_f, E_c^n), \phi(r_c, E_c^n)]}{\phi(r_f, E_c^n)\phi(r_c, E_c^n)} - \frac{Cov[\phi(r_c, E_f^n), \phi(r_c, E_c^n)]}{\phi(r_c, E_f^n)\phi(r_c, E_c^n)} - O(3) = \epsilon \quad \text{(A.23)}$$

where $\epsilon << 1$.

From Eq. (A.20b) we have,

$$R^2(r_f, E_c^n) + R^2(r_c, E_f^n) + R^2(r_c, E_c^n) + 2\frac{Cov[\phi(r_f, E_c^n), \phi(r_c, E_f^n)]}{\phi(r_f, E_c^n)\phi(r_c, E_f^n)} - 2\frac{Cov[\phi(r_f, E_c^n), \phi(r_c, E_c^n)]}{\phi(r_f, E_c^n)\phi(r_c, E_c^n)} - 2\frac{Cov[\phi(r_c, E_f^n), \phi(r_c, E_c^n)]}{\phi(r_c, E_f^n)\phi(r_c, E_c^n)} + O(3) > 0 \quad \text{(A.24)}$$

and the correction terms - covariance terms and O(3) term - can be ignored only if the following condition is satisfied,

$$R^2(r_f, E_c^n) + R^2(r_c, E_f^n) + R^2(r_c, E_c^n) >> -2\left[\frac{Cov[\phi(r_f, E_c^n), \phi(r_c, E_f^n)]}{\phi(r_f, E_c^n)\phi(r_c, E_f^n)} - \frac{Cov[\phi(r_f, E_c^n), \phi(r_c, E_c^n)]}{\phi(r_f, E_c^n)\phi(r_c, E_c^n)} - \frac{Cov[\phi(r_c, E_f^n), \phi(r_c, E_c^n)]}{\phi(r_c, E_f^n)\phi(r_c, E_c^n)} + O(3)\right] \quad \text{(A.25)}$$

By substituting Eq. (A.23) into Eq. (A.25) we end up with,

$$R^2(r_f, E_c^n) + R^2(r_c, E_f^n) + R^2(r_c, E_c^n) >> -2\left[\epsilon - R^2(r_c, E_c^n) + O(3)\right] = -2\epsilon + 2R^2(r_c, E_c^n) - O(3) \quad \text{(A.26)}$$

which could be further simplified to

$$R^2(r_f, E_c^n) + R^2(r_c, E_f^n) + 2\epsilon + O(3) >> R^2(r_c, E_c^n) \quad \text{(A.27)}$$

If we considered the acceptable uncertainty by MCNP standards, we have $R(r_f, E_c^n) < 10\%$ and $R(r_c, E_f^n) < 10\%$. The term O(3) encapsulates information

about high order moments of the flux such as the skewness, etc. and was found to be $<< 0$ and by ignoring ϵ as $\epsilon << 1$, we end up with the final condition given by

$$10\sqrt{2}\% >> R(r_c, E_c^n) \tag{A.28}$$

BIBLIOGRAPHY

[1] L. El-Guebaly. "History and Evolution of Fusion Power Plant Studies: Past, Present, and Future Prospects". *International Journal of Energy, Environment, and Economics.*, 18(1–2):115–167, 2011.

[2] L. El-Guebaly and S. Malang. "Toward the Ultimate Goal of Tritium Self-Sufficiency: Technical Issues and Requirements Imposed on ARIES Advanced Power Plants". *Fusion Engineering and Design*, 84:2072–2083, 2009.

[3] IAEA. "Technical Basis for the ITER Final Design Report, Cost Review and Safety Analysis (FDR), ITER EDA Documentation Series". 16, 1998.

[4] C. E. Kessel, *et al*. "The Fusion Nuclear Science Facility, the Critical Step in the Pathway to Fusion Energy". *Fusion Science and Technology*, 68:225–236, 2015.

[5] X-5 Monte Carlo Team. "MCNP™ a General Monte Carlo N-Particle Transport Code Version 5, Tech. Rep. LA-CP-03-0245, Los Alamos National Laboratory". 2005.

[6] A. Ferrari and P. Sala, *et al*. "FLUKA: a Multi − Particle Transport Code, CERN-2005-10, INFN/$TC_0$5/11, SLAC − R − 773". 2005.

[7] T. Tautges and P. P.H. Wilson, *et al*. "Acceleration Techniques for Direct Use of CAD-Based Geometries in Monte Carlo Radiation Transport". International Conf on Mathematics, Computational Methods & Reactor Physics (M&C)". *Saratoga Springs, NY: American Nuclear Society*, 2009.

[8] E.E. Lewis and W.F. Miller Jr. "Computational Methods of Neutron Transport". *American Nuclear Society, Inc*, 1993.

[9] E. Biondo and A. Ibrahim. "Accelerating Fusion Reactor Neutronics Modeling by Automatic Coupling of Hybrid Monte Carlo / Deterministic Transport on CAD Geometry". *ANS MC2015 - Joint International Conference on Mathematics*

and Computation (M&C), Supercomputing in Nuclear Applications (SNA) and the Monte Carlo (MC) Method, Nashville, Tennessee USA, 2015.

[10] A. Haghighat and John C. Wagner. "Monte Carlo Variance Reduction with Deterministic Importance Functions". *Progress in Nuclear Energy*, 42:25–53, 2003.

[11] Y. Chen and U. Fischer. "Rigorous MCNP based shutdown dose rate calculations: computational scheme, verification calculations and applications to ITER". *Fusion Engineering and Design*, 63 - 64:107–114, 2002.

[12] Douglas E. Peplow and A. Ibrahim, *et al*. "Propagation of Uncertainty from a Source Computed with Monte Carlo". *Transactions of the American Nuclear Society, Atlanta, Georgia June 16-20*, 108, 2013.

[13] T. Frosio and T. Bonaccorsi, *et al*. "Nuclear Data Uncertainties Propagation Methods in Boltzmann/Bateman Coupled Problems: Application to Reactivity in MTR". *Annals of Nuclear Energy*, 90:303–317, 2016.

[14] A. Ibrahim and Douglas E. Peplow, *et al*. "Novel hybrid Monte Carlo / deterministic technique for shutdown dose rate analyses of fusion energy systems". *Fusion Engineering and Design*, 89:1933–1938, 2014.

[15] A. Ibrahim and Douglas E. Peplow, *et al*. "The Multi-Step CADIS Method for ShutDown Dose Rate Calculations and Uncertainty Propagation". *Nucear Technology*, 192:286–298, 2015.

[16] E. Biondo and Paul P. H. Wilson. "Transmutation Approximations for the Application of Hybrid Monte Carlo / Deterministic Neutron Transport to Shutdown Dose Rate Analysis". *Nuclear Science and Engineering*, 187:27–48, 2017.

[17] M. Majerle and D. Leichtle, *et al*. "Verification and validation of the R2Smesh approach for the calculation of high resolution shutdown dose rate distributions". *Fusion Engineering and Design*, 87:443–447, 2012.

[18] G. Bell and S. Glasstone. "Nuclear Reactor Theory". *Van Nostrand and Reinhold, New York*, 1970.

[19] P. P.H. Wilson and H. Tsige-Tamirat, *et al*. "Validation of the ALARA Activation Code". *Fusion Science and Technology*, 34:78–88, 1998.

[20] Robin A. Forrest. "FISPACT-2007: User manual. Technical Report". *UKAEA FUS 534, Culham Science Centre, Oxfordshire, OX14 3DB*, 2007.

[21] Bateman. "Solution of A System of Differential Equations". *Proceedings of the Cambridge Philosophical Society, Mathematical and physical sciences, http://www.biodiversitylibrary.org/item/97262*, 15:423–427, 1908–1910.

[22] ICRP Publication 74. "Conversion Coefficients for use in Radiological Protection against External Radiation". *Ann. ICRP, No. 3/4, Elsevier, Amsterdam*, 26, 1996.

[23] D. Valenza and H. Lida, *et al*. "Proposal of shutdown dose estimation method by Monte Carlo code". *Fusion Engineering and Design*, 55:411–418, 2001.

[24] R. Villari and U. Fischer, *et al*. "Shutdown dose rate assessment with the Advanced D1S method: Development, applications and validation". *Fusion Engineering and Design*, 89, 2014.

[25] U. Fischer and D. Leichtle, *et al*. "Review and Validation of Shutdown Dose Rate Estimation Techniques for Application to ITER". *Fusion Science and Technology*, 64:563–570, 2017.

[26] A. Davis and R. Pampin. "Benchmarking the MCR2S system for high-resolution activation dose analysis in ITER". *Fusion Engineering and Design*, 85:87–92, 2010.

[27] FESAC. "Priorities, Gaps and Opportunities: Towards a Long-Range Strategic Plan for Magnetic Fusion Energy". *http://www.ofes.fusion.doe.gov/fesac.shtml*, 2007.

[28] D. Rochman and A. J. Koning, *et al*. "Exact Nuclear Data Uncertainty Propagation for Fusion Design". *Journal of the Korean Physical Society*, 59:1386–1389, 2011.

[29] D. Rochman and W. Zwermann, *et al*. "Efficient Use of Monte Carlo: Uncertainty Propagation". *NUCLEAR SCIENCE AND ENGINEERING*, 177:337–349, 2017.

[30] Gi YoungHan and Do Hyun Kim, *et al*. "On-the-fly Estimation Strategy for Uncertainty Propagation in Two-Step Monte Carlo Calculation for Residual Radiation Analysis". *Nuclear Engineering and Technology*, 48:765–772, 2016.

[31] I. Lux and L. Koblinger. "Monte Carlo Particle Transport Methods: Neutron and Photon Calculations". *CRC press*, 1991.

[32] M. J. Loughlin. "Conclusions of Shutdown Dose Rate Benchmark Study, IDM Number: 6593RF v1.0". *6th ITER Neutronics Meeting, Hefei, China, June 19–24*.

[33] Moataz S. Harb and L. El-Guebaly, *et al*. "3-D Neutronics Assessment of Tritium Breeding Capacity and Shielding of Tokamak-Based Fusion Nuclear Science Facility". *Fusion Science and Technology*, 72:510–515, 2017.

[34] A. Davis and Moataz S. Harb, *et al*. "Neutronics Aspects of the FESS-FNSF". *Fusion Engineering and Design*, 2018.

[35] L. Waganer and C. Kessel, *et al*. The examination of the fnsf maintenance approach. *Fusion Engineering and Design*, 135:394–425, 2018.

[36] Moataz S. Harb and Bohm, *et al* T. "Calculation of Shutdown Dose Rate in Fusion Nuclear Science Facility During A Proposed Maintenance Scheme". *Manuscript submitted to Fusion Science and technology*.

[37] E. Biondo and A. Davis, *et al*. "Rigorous Two-Step Activation for Fusion Systems with PyNE". *Proceeding of the 18th Topical Meeting of the Radiation Protection & Shielding Division of ANS, Knoxville, TN*, 2014.

[38] C. Bates and E. Biondo, *et al*. "PyNE progress report". *Transactions of the American Nuclear Society*, 111, 2014.

[39] D. L. Aldama , *et al*. "FENDL2.1, Update of an Evaluated Nuclear Data Library for Fusion applications". *IAEA report INDC (NDS) 467, Vienna, Austria*, 2004.